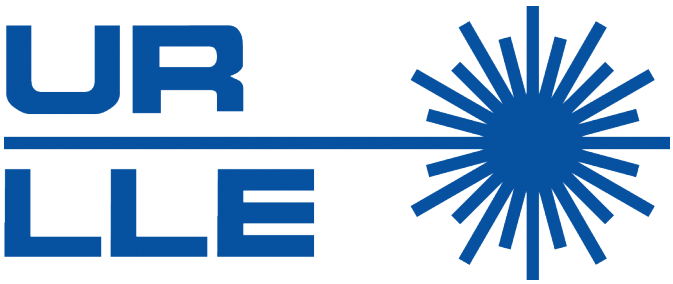

2022 SUMMER RESEARCH PROGRAM FOR HIGH SCHOOL JUNIORS

AT THE

UNIVERSITY OF ROCHESTER'S

LABORATORY FOR LASER ENERGETICS

STUDENT RESEARCH REPORTS

PROGRAM DIRECTOR

Dr. R. Stephen Craxton

January 2024 **Lab Report 500**

Laboratory for Laser Energetics
University of Rochester

2022 SUMMER RESEARCH PROGRAM FOR HIGH SCHOOL JUNIORS

AT THE

UNIVERSITY OF ROCHESTER'S

LABORATORY FOR LASER ENERGETICS

STUDENT RESEARCH REPORTS

PROGRAM DIRECTOR

Dr. R. Stephen Craxton

LABORATORY FOR LASER ENERGETICS

University of Rochester

250 East River Road

Rochester NY 14623-1299

During the summer of 2022, 16 students from Rochester-area high schools participated in the Laboratory for Laser Energetics' Summer High School Research Program (Fig.1). This was the 33rd year of the program, which started in 1989. The 2020 program was unfortunately canceled because of the COVID-19 pandemic. In 2021, LLE held a fully virtual program for students who had applied and been interviewed for the 2020 program, and in 2022 LLE was able to return to a normal, in-person program.

Figure 1.

Participants in LLE's 2022 Summer High School Research Program. Front Row: Cameron Ryan, Alisha Upal, Dr. Stephen Craxton, Grace Wu, Rick Zhou; Middle Row: Jackson McCarten, John Geiss, Elizabeth Norris, Jenny Zhao, Samuel Gray, David Villani, Jayden Roberts, Olivia Fietkiewicz; Back Row: Arjun Patel, Sara Davies, Vinay Pendri, and Micah Kim.

The goal of LLE's program is to excite a group of high school students about careers in the areas of science and technology by exposing them to research in a state-of-the-art environment. Too often, students are exposed to "research" only through classroom laboratories, which have prescribed procedures and predictable results. In LLE's summer program, the students experience many of the trials, tribulations, and rewards of scientific research. By participating in research in a real environment, the students often become more excited about careers in science and technology. In addition, LLE gains from the contributions of the many highly talented students who are attracted to the program.

The students spent most of their time working on their individual research projects with members of LLE's scientific staff. The projects were related to current research activities at LLE and covered a broad range of areas of interest including experimental diagnostic development, computer modeling of implosion physics, physical and computational chemistry, laser physics,

optical engineering, terahertz radiation, future laser system design, and scientific data management. The students, their high schools, their LLE supervisors, and their project titles are listed in Table I. Their written reports are collected in this volume. By working through several iterations of their project reports, incorporating feedback from their supervisors and the Program Director, the students experience most of the steps involved in preparing a scientific paper for publication.

The students attended weekly seminars on technical topics associated with LLE's research. Topics this year included laser physics, fusion, nonlinear optics, fission energy, pulsed power, fiber optics, and LLE's cryogenic target program. The students also received safety training, learned how to give scientific presentations, were given guidance on writing scientific reports, and were introduced to LLE's computational resources.

The program culminated on 24 August with the "High School Student Summer Research Symposium," at which the students presented the results of their research to an audience including parents, teachers, and LLE staff. Each student spoke for approximately eight minutes and answered questions. At the symposium LLE presented its 24th annual William D. Ryan Inspirational Teacher Award. The recipient this year was Mrs. Dawn Knapp, a mathematics teacher at Victor High School. This award honors a teacher, nominated by alumni of the LLE program, who has inspired outstanding students in the areas of science, mathematics, and technology. Mrs. Knapp was nominated by Semma Alfatlawi, a participant in the 2021 Summer Program.

A total of 415 high school students have participated in the program from its inception through 2022. The students in 2022 were selected from just under 40 applicants. Each applicant submitted an essay describing his or her interests in science and technology, a copy of his or her transcript, and a letter of recommendation from a science or math teacher.

LLE plans to continue this program in future years. The program is strictly for students from Rochester-area high schools who have just completed their junior year. Application information is mailed to schools and placed on the LLE web site in January with an application deadline near the middle of March. For more information about the program, please contact Dr. R. Stephen Craxton at LLE.

Acknowledgment

This material is based upon work supported by the Department of Energy National Nuclear Security Administration under Award Number DE-NA0003856, the University of Rochester, and the New York State Energy Research and Development Authority.

Table I: High School Students and Projects—Summer 2022.

Name	High School	Supervisor	Project Title
Sara Davies	Pittsford Sutherland	R. S. Craxton	Direct-Drive Uniformity Calculations for a Future High-Gain Laser Facility
Olivia Fietkiewicz	Mercy	S. Bucht	Measuring the Mode Field Diameter of Single-Mode Fibers Using the Knife-Edge Technique
John Giess	McQuaid	V. N. Goncharov and K. M. Woo	Mitigating Rayleigh–Taylor Instabilities in the Deceleration Phase of Inertial Confinement Fusion
Samuel Gray	Brighton	W. T. Shmayda and E. Dombrowski	Characterizing a Cryosorption Pump for Collecting Tokamak Exhausts
Micah Kim	Home School	D. W. Jacobs-Perkins	Design, Fabrication, and Testing of a 3-D–Printed Optomechanical Assembly for MIFEDS Coil Characterization
Jackson McCarten	Webster Schroeder	B. N. Hoffman and K. R. P. Kafka	Viability Testing of Polymer Coating for Optical Cleaning Applications
Elizabeth Norris	Brighton	M. D. Wittman	Determining the Absorption Efficiency of a Flow-Through Pd-Bed as a Function of Initial ^4He:D_2 Ratio and Flow Rate
Arjun Patel	Brighton	D. Chakraborty and R. Sobolewski	Terahertz Time-Domain Characterization of Biological Tissues Modeled Using COMSOL Multiphysics
Vinay Pendri	Pittsford Mendon	K. L. Marshall	Computational Modeling of Liquid Crystals and Related Materials Using Time-Dependent Density Functional Theory
Jayden Roberts	Brockport	S. T. Ivancic	Investigation of Microwave-Induced Chemical Etching in CR39
Cameron Ryan	McQuaid	R. W. Kidder	Containerized Application Management for Cloud-Based Scientific Analysis
Alisha Upal	Pittsford Sutherland	R. S. Craxton	Development of a National Ignition Facility Laser Configuration with X-Ray Backlighting for Direct Drive of a Foam Ball Target
David Villani	Harley School	M. J. Guardalben	Energy Prediction on the OMEGA EP Laser System Using Neural Networks
Grace Wu	Pittsford Mendon	I. A. Begishev	Measurement of the Refractive Indices of KDP and ADP at Low Temperatures
Jenny Zhao	Pittsford Mendon	K. L. Marshall and N. D. Urban	Chiroptical Properties and Mesophase Stability of Saturated Chiral Dopants for High-Peak-Power Liquid Crystal Device Applications
Rick Zhou	Brighton	W. T. Shmayda and M. Sharpe	Measuring the Performance of Molecular Sieve Driers

Direct Drive Uniformity Calculations for a Future High Gain Laser Facility

Sara C. Davies

Pittsford Sutherland High School

Pittsford, NY

Advisor: Dr. R. Stephen Craxton

Laboratory for Laser Energetics

University of Rochester

Rochester, NY

December 2023

Abstract

This work investigates the optimization of uniformity for direct drive experiments on a possible future laser facility larger than the National Ignition Facility (NIF). The NIF has 48 groups of 4 beams, or quads. The proposed facility has 96 quads. A key feature of the facility is that it can perform both direct and indirect drive. Indirect drive will use octahedral hohlraums, which promise greater uniformity than the cylindrical hohlraums used on the NIF. The 2-D hydrodynamic code *SAGE* was applied to evaluate beam repointing for direct drive. The optimum repointing obtained maintains all beam repointings below 14.1° and gives a root mean square nonuniformity of 0.41%. These results show that the optimized design promises highly uniform direct drive implosions on a facility also capable of highly uniform indirect drive.

I Introduction

Nuclear fusion promises a long-lasting source of clean energy. One approach to fusion uses laser beams to heat a spherical capsule that contains fuel made of deuterium (D) and tritium (T), two isotopes of hydrogen. As the exterior of the capsule is heated to high temperatures it turns into an expanding plasma, thus exerting an inward pressure on the fuel. The compressed fuel can reach densities and temperatures far higher than those found anywhere else on the Earth. The high temperature of the fuel allows the positively charged D and T nuclei to overcome the electrostatic repulsion forces, allowing fusion to occur, while the high density ensures that enough fusion reactions occur before the fuel expands and cools. DT fusion forms a helium nucleus, or alpha particle, and releases a large amount of energy, mostly in the form of energetic neutrons. The helium nucleus can further heat the compressed fuel if the density and radius of the fuel are sufficient, reducing the energy required from the laser beams.

There are two approaches to laser-driven fusion, direct and indirect drive (Fig. 1). In

direct drive, laser beams directly irradiate the capsule. For indirect drive, the capsule is placed in a case, known as a hohlraum, made of a high-Z material, typically gold. The laser beams enter the hohlraum through laser entrance holes and deposit energy on the hohlraum walls. The walls then emit x rays, which irradiate the capsule. Indirect drive is less energy efficient than direct drive as only a fraction of the laser power, 10-20%, is absorbed by the capsule. Indirect drive is, however, less sensitive to small imperfections in the laser beams.

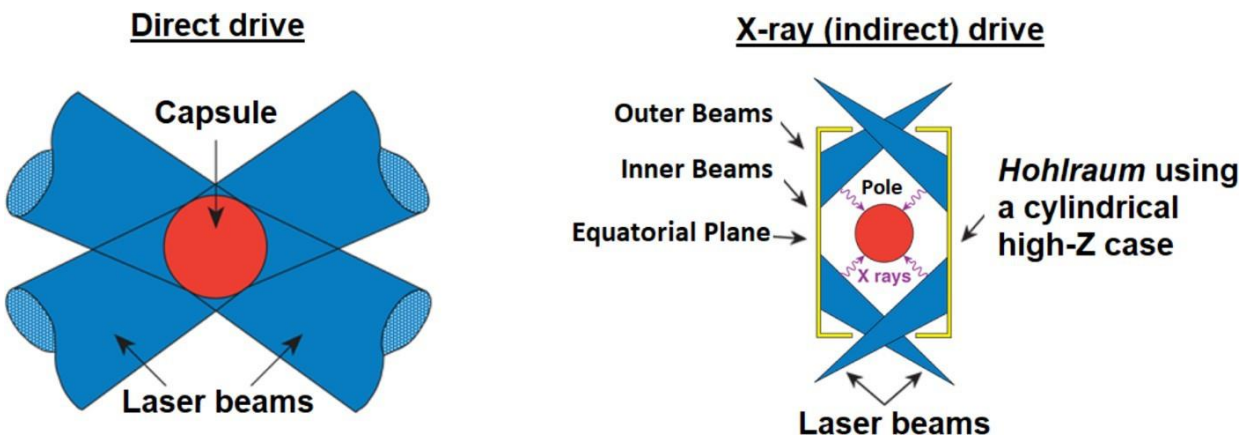

Figure 1: *The two main approaches to laser-driven fusion, direct and indirect drive. The model of indirect drive depicts a cross-section of a cylindrical hohlraum. From Ref. 1*

Regardless of the approach used, it is essential to obtain high levels of irradiation uniformity on the capsule [2]. The National Ignition Facility (NIF), dedicated to indirect drive, currently uses cylindrical hohlraums, which make it difficult to implode the spherical fuel capsules uniformly. With heroic efforts, Livermore have been able to obtain implosions with very good uniformity. During the implosion, material that ablates from the hohlraum wall makes it difficult for the inner beams to reach the equator of the hohlraum, reducing the drive on the equator.

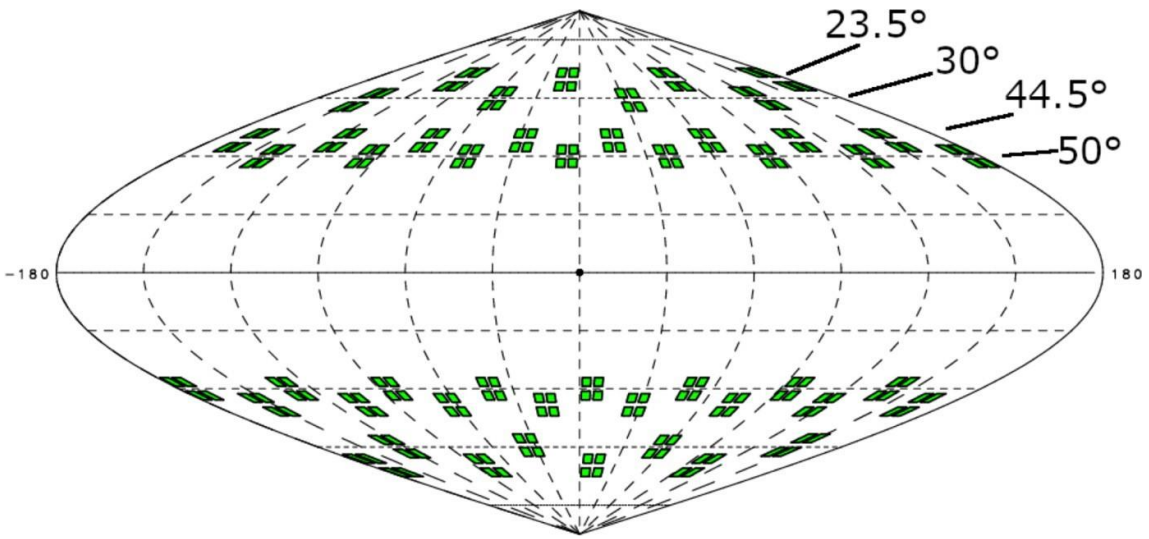

Figure 2: *The locations of laser beam ports on the NIF target chamber, indicated in green, are grouped into 48 quads of four beams each. From Ref. 1*

Due to the NIF's target chamber design, symmetrical direct drive is impractical. The NIF beam ports are specifically designed to perform indirect drive experiments with cylindrical hohlraums. The beam ports are arranged in four rings in each hemisphere with a total of 48 quads, which are groups of four beams (Fig. 2). If the beams are pointed at the center of the capsule for direct drive experiments, the equatorial regions of the capsule are underdriven compared to the poles. To perform direct drive experiments on the NIF the beams need to be repointed towards the equator. Some of the beams need to be repointed by as much as 35° [3, 4]. When the beams are repointed by such a large angle, the energy from the beams refracts around the edge of the capsule, reducing absorption. Also, the distribution of energy around the surface of the capsule changes as the capsule implodes, limiting the convergence that can be achieved. Therefore, the NIF is unsuitable for uniform high-convergence direct drive implosions.

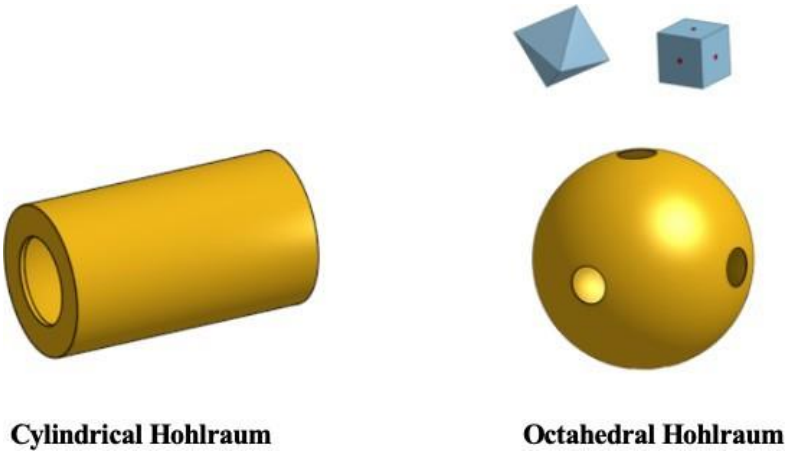

Figure 3: *Comparison between cylindrical and octahedral hohlraums. The holes in the hohlraums represent laser entrance holes. The octahedral hohlraum has six laser entrance holes, corresponding to the six vertices of a regular octahedron or faces of a cube. From Ref. 1*

Octahedral hohlraums have been proposed as more uniform alternatives to cylindrical hohlraums, using 48 quads [5, 6, 7]. As shown in Fig. 3, the octahedral hohlraum has six laser entrance holes that correspond to the six vertices of an octahedron. The geometry of the octahedral hohlraum provides greater uniformity than cylindrical hohlraums. However, the NIF cannot use octahedral hohlraums as the NIF does not match the cubic symmetry needed for them.

Here, a higher energy, 96-quad laser facility is proposed to drive an octahedral hohlraum (Fig. 3) to achieve higher gain than the 48-quad NIF. The proposed facility would have twice as many beams as the NIF. Unlike the NIF, the proposed facility would be capable of driving highly symmetric, high-convergence implosions using both direct and indirect drive. The proposed facility extends previous work that investigated achieving both direct and indirect drive on a 48-quad system [1] to a 96-quad system.

II Layout of the 96-Quad System

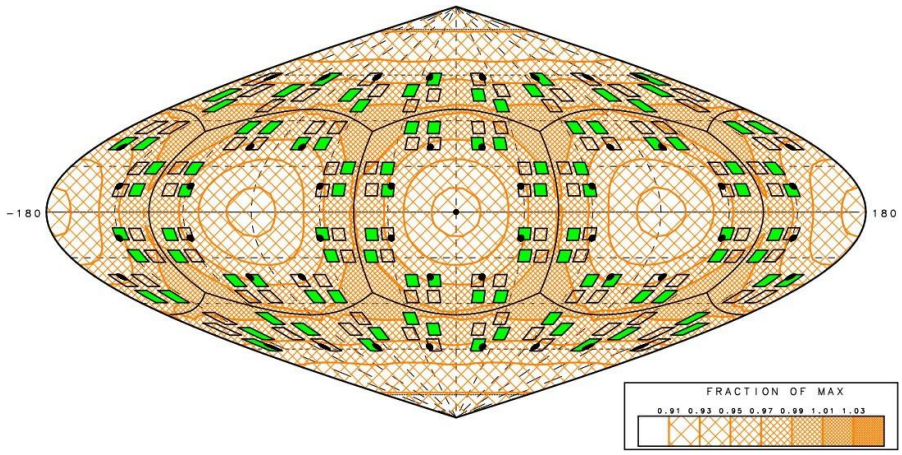

Figure 4: *Sinusoidal projection of the proposed 96-quad system. Green squares are beam ports. Black dots are the "ideal" aim points on a direct drive capsule. Open black squares represent the beam dumps on the opposite side of the target chamber. The curved black lines correspond to the edges of the cube. The contours give the relative irradiation intensity on the capsule when the beams are pointed at the closest ideal aim points. The lowest contour level drawn is 93% of maximum and the root mean square (RMS) intensity variation on the capsule surface is 2.26%.*

Figure 4 shows a projection of the proposed system, with the green squares indicating the 96 quads and the open squares the beam dumps on the opposite side of the target chamber. (Note that in Fig. 2, each green square represents a single beam.)

Like the NIF, the 96-quad system has non-opposed beams so that if a beam misses the target it cannot pass through the opposing port and damage the optics in the IR portion of the laser system. Instead, beam dumps are provided on the chamber wall. The beam dumps are also required to absorb the unconverted infrared and second-harmonic light from the frequency conversion process. The geometry of the 96-quad system allows for good diagnostic access, with large areas available at the six faces and eight corners of the cube. However, there are downsides to the 96-quad system's layout. The non-opposed beams make beam repointings for direct drive more difficult. Non-opposed beams also require double the solid angle for the beam dumps, complicating the design of the beam ports.

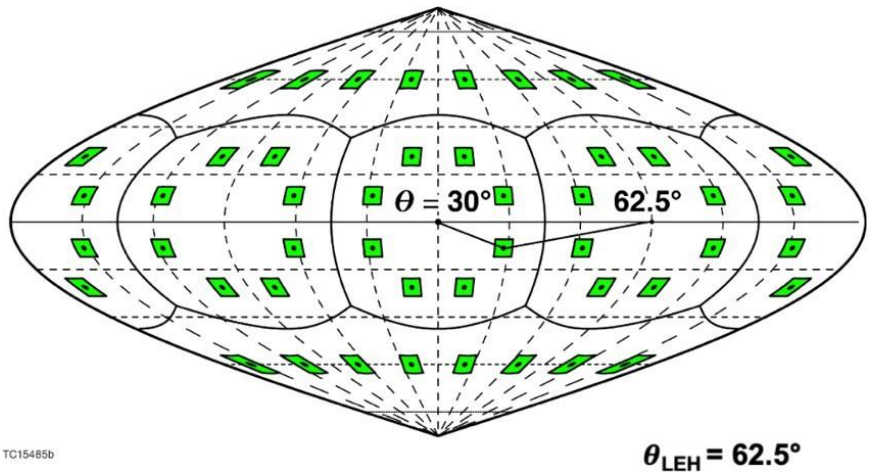

Figure 5: *Proposed 48-quad system from Refs. 8 and 9 with beams 30° from the centers of the cube faces. The black dots represent the "ideal" aim points. Figure from Refs. 10 and 11.*

Figure 4 also shows the "ideal" aim points (black dots), used as a starting point for the optimization of the 96-quad system. The ideal aim points are those proposed for a 48-quad Russian system [8, 9], illustrated in Figure 5. The 30° angle proposed in Refs. 8 and 9 provides excellent uniformity, as was independently confirmed in Refs. 10 and 11. For indirect drive using an octahedral hohlraum, all beams would enter the laser entrance hole on the adjacent face of the cube at 62.5° (although they could enter through the closest laser entrance hole at 30°).

For the *SAGE* simulation of Fig. 4, all beams are pointed at the ideal aim points. The contour levels show the time-integrated deposited energy. The simulation gives a root mean squared (RMS) intensity variation on the capsule surface of 2.26%. This RMS is high for efficient direct drive, considering that <1% is considered to be essential. Figure 4 shows that aiming at the ideal aim points results in too much deposition on the corners of the cube and too little at the centers of the faces of the cube. Simulations of a 48-quad system using these ideal aim points also resulted in a large RMS [10]. Thus it is necessary to repoint the beams to reduce the RMS nonuniformity below 1%.

III Optimization of Beam Pointing

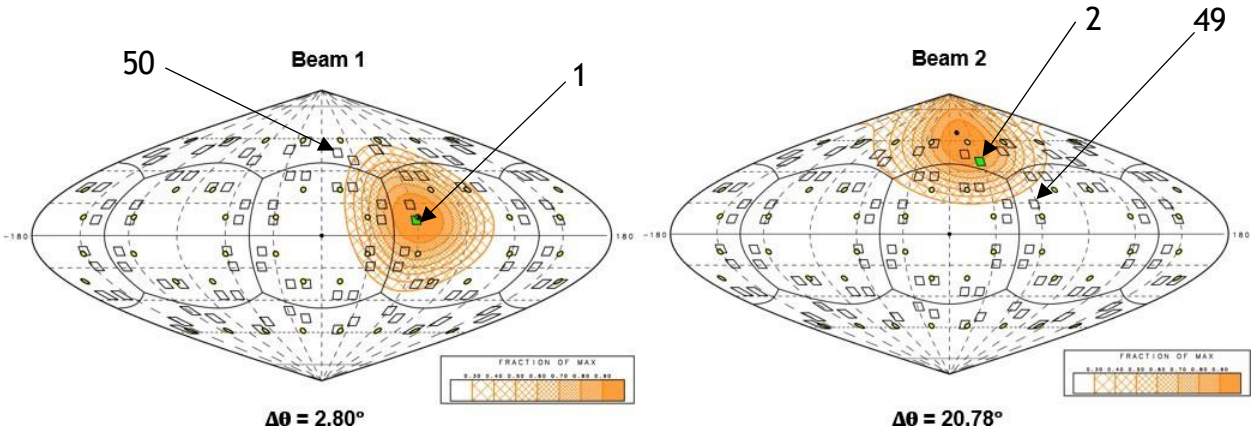

Figure 6: *Contour plots of the deposited laser energy on the capsule (as a fraction of the maximum) produced by beams 1 & 2 for the initial optimization. Left shows beam 1 and right shows beam 2, for the initial optimization. Beams/quads 1, 2, 49, and 50 are labeled by arrows. The yellow dots with black borders represent the ideal aim points. The black dots represent where beams 1 & 2 are actually pointed. Beam 1 is shifted 2.80° while beam 2 is shifted 20.78°.*

The first attempt at optimizing the beam repointings was based on individually optimizing four sets of beams, each set comprising 24 beams that have equivalent locations due to symmetry. Beams 1, 2, 49, and 50 in Fig. 6 represent the four sets. There are three equivalent locations on the cubic face that contains beam 1, obtained by 90° rotations, giving four equivalent beams per face or 24 equivalent beams total. Following Refs. 1 and 10, the beam locations are defined by the angle θ, representing the distance from the center of the face as shown in Fig. 5, and the azimuthal angle φ around the center of the face, measured counterclockwise relative to one of the axes. (For example, φ is 22.5° in Fig. 5.) In the proposed configuration, beam 1 is given by (θ=60°, φ=11°), beam 2 by (53°, 65.5°), beam 49 by (60°, 22.25°), and beam 50 by (53°, 77.75°). Each set is optimized by modeling just one of these four beams and rotating the deposited energy to the 23 equivalent locations.

Figure 6 depicts the cumulative deposited energy on the capsule for SAGE simulations of beams 1 and 2. The small yellow circles with black borders represent the ideal aim points and the

small black dots show the actual aim points of beams 1 and 2 with the optimized repointings. Since beam 1 is located very close to an ideal aim point, the ideal and actual aim points are virtually the same. However, for beam 2, the actual aim point is moved beyond the ideal aim point (as in Ref. 10) so that the deposited energy pattern is centered on the ideal aim point. Similarly to the beam port locations, the aim-point locations are defined by two parameters (θ_{aim}, φ_{aim}). The optimization is performed by varying these parameters.

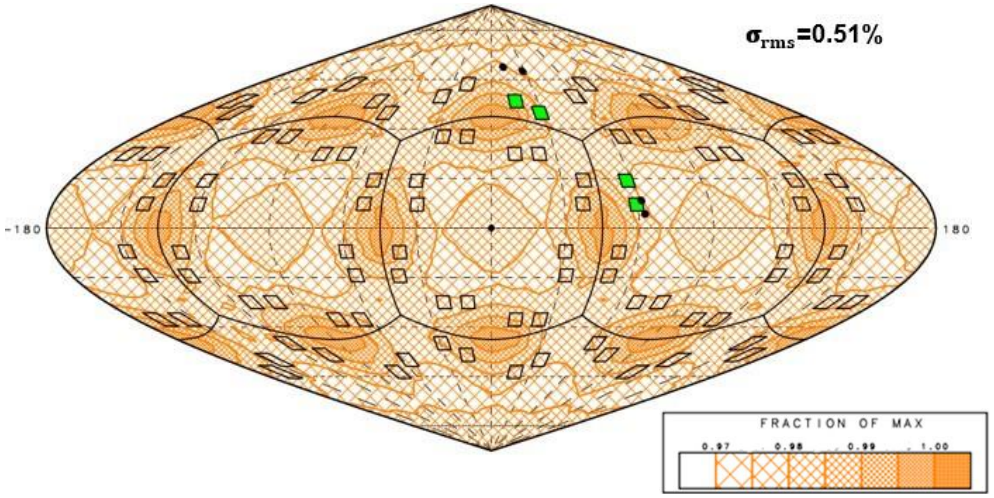

Figure 7: *Energy deposition pattern obtained by combining the patterns of four beams (1, 2, 49, 50) aimed past the ideal aim points as in Fig. 6 and symmetrizing them. The RMS nonuniformity is 0.51%.*

Figure 7 shows the result of combining the four beams (1, 2, 49, 50), each optimized individually as shown in Fig. 6, with the energy deposition pattern rotated to the 23 equivalent locations. The process of rotating the energy deposition patterns is known as symmetrizing. The pattern for each of the four beams was symmetrized individually to obtain the optimum pointing for each beam. The optimum pointings for each individual beam were then combined and the result symmetrized to produce the result shown in Fig. 7. By symmetrizing the energy deposition, it is possible to calculate the full energy deposition pattern modeling just four beams. The RMS nonuniformity significantly decreases from 2.26% to 0.51%.

Although the deposition pattern produced in Fig. 7 is far more uniform than the deposition pattern produced by aiming at the ideal aim points (Fig. 4), beam 2 requires repointing by 20.78° (measured around a great circle). This large repointing is not ideal because oblique incidence leads to lower absorption and can enhance energy loss from cross-beam energy transfer [12]. Conversely, beam 1 only had to be repointed by 2.80°. To minimize the repointing of beam 2, a solution was sought with intermediate repointings for each beam.

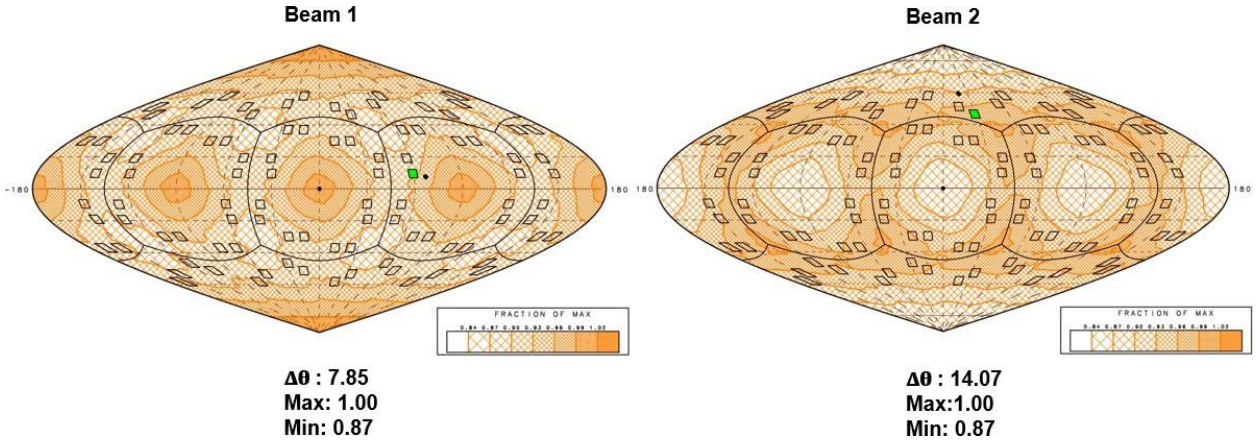

Figure 8: *Symmetrized energy deposition patterns for beam 1 (left) and beam 2 (right), for the final optimization. The two deposition patterns are complementary, with the same maximum (1.0) and minimum (0.87) values at different locations. This enables the maximum repointing angle Δθ of beam 2 to be reduced to 14.07°.*

To reduce the repointing angle of beam 2, beam 1 was pointed further from the ideal aim point toward the center of the face while beam 2 was pointed closer to the ideal aim point, producing the complementary deposition patterns shown in Fig. 8. These patterns ensure that when the two beams are combined, the strong center and weak corners of beam 1 line up with the weak center and strong corners of beam 2. As shown in Fig. 8, the maximum and minimum contours of beams 1 and 2 have the same values in complementary locations, allowing the deposition patterns, when combined, to have a low RMS while also lowering the repointing of beam 2 from 20.78° to 14.07°.

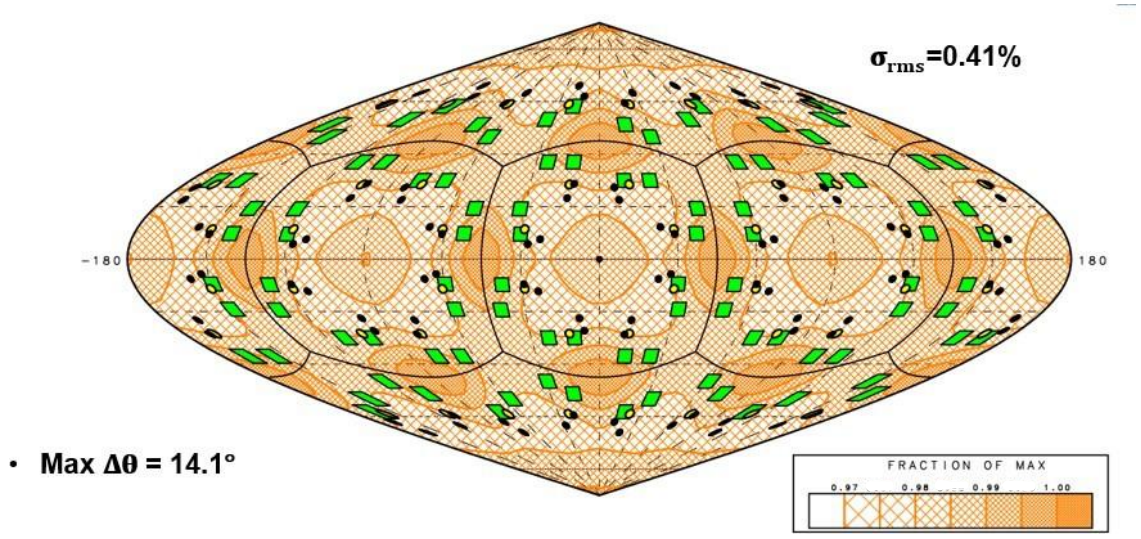

Figure 9: *Time-integrated energy deposition pattern for the final optimization of the 96-quad system with all 96 beams modeled. The yellow dots with black borders represent the ideal aim points and the black dots the optimized aim points.*

When the new complementary optimization of beams 1 and 2 is combined with the optimization of the other two beams, 49 and 50, the deposition pattern in Fig. 9 is achieved. For this figure, the optimized pointings of the four beams were applied to all 96 beams and the resulting deposition was also symmetrized, to ensure the most accurate model with numerical noise minimized. The scale is the same as for Fig. 7, with the lowest contour 0.97% of the maximum. The lowest value plotted is 0.98%, so although the deposition pattern has stronger edges and weaker corners, the overall variability is very low. Along with the maximum shift $\Delta\theta$ decreasing from 20.78° to 14.07°, the RMS has also decreased from the 0.51% in Fig. 7 to 0.41%.

V Conclusions

This work investigated the optimization of uniformity for direct drive experiments on a possible future laser facility that uses 96 quads. A key feature of the facility is that it can be used for both direct and indirect drive. Indirect drive will use spherical hohlraums with six laser entrance holes, which promise greater uniformity than the cylindrical hohlraums used on the

NIF. The 2-D hydrodynamics code *SAGE* was used to calculate beam repointings that provide maximum laser irradiation uniformity for direct drive. The optimum pointing design minimizes the repointing angles of the beams and results in a nonuniformity of 0.41% (RMS), with no beam repointed by more than 14.1° (compared with ~35° for direct drive designs on the NIF). These results show that the optimized design promises highly uniform direct drive implosions on a facility also capable of highly uniform indirect drive.

Acknowledgments

I would like to thank Dr. Craxton for all the hours he has dedicated to helping me do this research and for putting together this program. I would also like to thank my fellow students for their support. Additionally, the IT department was a great help through all the network issues I had. Lastly, I would like to thank Ms. Truebger for all her help in making sure this program ran smoothly.

References

[1] W. Wang. “Development of a Beam Configuration for the SG4 Laser to Support both Direct and Indirect Drive”. In: LLE Summer High School Research Program (2019). URL: https://www.lle.rochester.edu/media/publications/high_school_reports/documents/hs_reports/2019/Wang_William.pdf.

[2] J. D. Lindl. “Development of the indirect-drive approach to inertial confinement fusion and the target physics basis for ignition and gain”. In: Physics of Plasmas 2.11 (1995), pp. 3933-4024. DOI: 10.1063/1.871025. eprint: https://doi.org/10.1063/1.871025. URL: https://doi.org/10.1063/1.871025.

[3] P. B. Radha et al. “Direct drive: Simulations and results from the National Ignition Facility”. In: Physics of Plasmas 23.5 (2016), p. 056305. DOI: 10.1063/1.4946023. eprint: https://doi.org/10.1063/1.4946023.

[4] T. J. B. Collins et al. “A polar-drive-ignition design for the National Ignition Facility”. In: Physics of Plasmas 19.5 (2012), p. 056308. DOI: 10.1063/1.3693969. eprint: https://doi.org/10.1063/1.3693969. URL: https://doi.org/10.1063/1.3693969.

[5] K. Lan et al. “Octahedral spherical hohlraum and its laser arrangement for inertial fusion”. In: Physics of Plasmas 21.5 (2014), p. 052704. DOI: 10.1063/1.4878835. eprint: https://doi.org/10.1063/1.4878835. URL: https://doi.org/10.1063/1.4878835.

[6] K. Lan and W. Zheng. “Novel spherical hohlraum with cylindrical laser entrance holes and shields”. In: Physics of Plasmas 21.9 (2014), p. 090704. DOI: 10.1063/1.4895503. eprint: https://doi.org/10.1063/1.4895503. URL: https://doi.org/10.1063/1.4895503.

[7] K. Lan et al. “High Flux Symmetry of the Spherical Hohlraum with Octahedral 6 LEHs at the Hohlraum-to-Capsule Radius Ratio of 5.14”. In: Physics of Plasmas 21 (2014). DOI:

10.1063/1.4863435.

[8] S. A. Bel'kov et al. "Thermonuclear Targets for Direct-Drive Ignition by a Megajoule Laser Pulse". In: Journal of Experimental and Theoretical Physics 121.4 (2015). ISSN: 1063-7761.

[9] N. N. Demchenko. "Uniformity Simulation of Multiple-Beam Irradiation of a Spherical Laser Target with the Inclusion of Radiation Absorption and Refraction". In: Quantum Electronics 49.2 (2019). URL: https://doi/org/10.1070/QEL16784.

[10] M. Marangola. "Optimization of Direct Drive Designs for a Proposed Dual Direct/ Indirect Drive Laser". In: LLE Summer High School Research Program (2021). URL: https://www.lle.rochester.edu/media/publications/high_school_reports/documents/hs_reports/2021/Marangola_Meghan.pdf.

[11] R. S. Craxton. "A Dual Laser-Beam Configuration Compatible with Both Symmetric Direct Drive and Spherical Hohlraums". Presented at: 63rd Annual Meeting of the American Physical Society Division of Plasma Physics, Pittsburgh, PA, Nov. 2021.

[12] R.K. Kirkwood et al. "Observation of Energy Transfer Between Frequency-Mismatched Laser Beams in a Large-Scale Plasma". In: Physical Review Letters 76.12 (1996), p. 2065. URL: https://doi.org/10.1103/PhysRevLett.76.

Measuring the Mode Field Diameter of Single Mode Fibers Using the Knife-Edge Technique

Olivia Fietkiewicz

Our Lady of Mercy School for Young Women

Advisor: Sara Bucht

Laboratory for Laser Energetics

University of Rochester

November 2023

I. Abstract

Single mode fiber is used extensively in both telecommunications and the scientific community. At the Laboratory for Laser Energetics (LLE), single mode fiber is used in the fiber amplifiers which seed the OMEGA and OMEGA EP amplifiers, among other applications. An important property of single mode fiber is the mode field diameter (MFD), which is traditionally determined as the $1/e^2$ width of the intensity inside the fiber. Knowing MFD is an important parameter for preventing loss when coupling or splicing fibers and predicting how light will behave when it exits a fiber. The knife-edge technique, unique for its simplicity, is a method of measuring MFD that uses a razor edge to incrementally cut off the amount of light that reaches a power meter. The MFD measured by a knife-edge setup was within vendor specifications for two types of single mode fiber, validating its accuracy. The MFD of the SM980 fiber, a fiber commonly used at LLE, was measured to be 6.0 ± 0.1 μm at 1053 nm. This setup is a key step for improving LLE's technical knowledge of fibers, including polarization maintaining and other specialty fibers.

II. Introduction/Background

Knowing the mode field diameter (MFD) of a single mode fiber is useful because it allows for effective and efficient use of the fiber. Optical fibers are fibers made with a glass core that can guide light over long distances and in many directions without the light losing a significant portion of its strength. Single mode fiber is a specific type of optical fiber that is characterized by the fact that its core is so small that it can only support a single mode of light, whereas a multimode fiber has a larger core that allows for multiple modes of light to travel through the fiber. The light that travels through a single mode fiber maintains a Gaussian profile even as it exits the fiber and propagates into the air [1].

Fiber has many applications in the world and within the Laboratory for Laser Energetics (LLE). For instance, optical fiber has applications within cable TV and the internet, along with in medicine and dentistry, among other industries. In medicine, single mode fiber is used in procedures such as endoscopies to give medical professionals access to places in the human body that are otherwise difficult to see or access, such as the stomach or other parts of the gastrointestinal tract. Single mode fiber is also useful for data transmission because it can transport information better than the copper wires that are traditionally used. Single mode fibers can carry data over much longer distances and with reduced attenuation, or loss, compared to copper wires. Within LLE, fiber is used for various experiments as well as in the OMEGA and OMEGA EP lasers. Single mode fiber is used in the fiber amplifiers in the initial amplification stage of the two lasers.

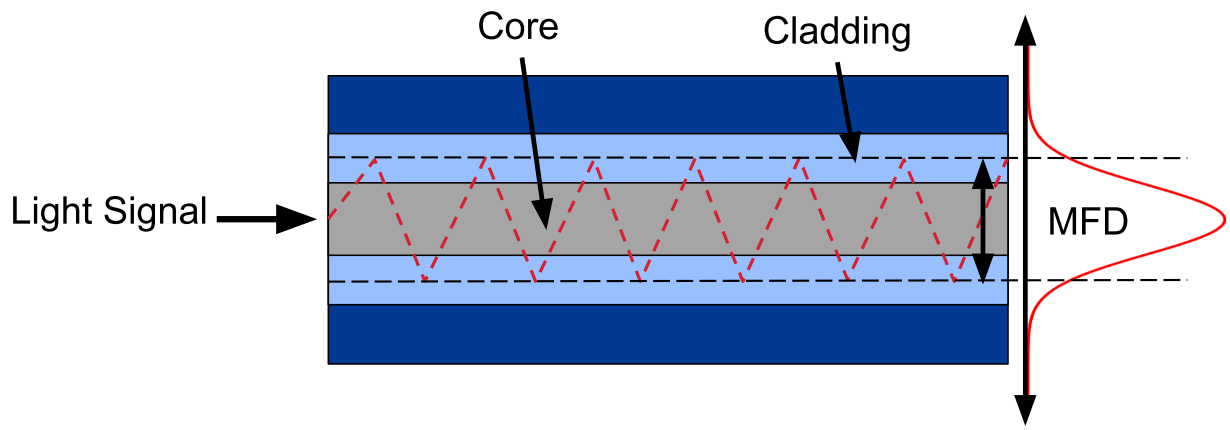

Figure 1: *Diagram of the inside of a single mode fiber. As light travels through the fiber, it doesn't stay within the core; instead, it extends into the cladding as well. The mode field diameter (MFD) is the diameter of the intensity curve of the light signal within the fiber at the* $1/e^2$ *level.*

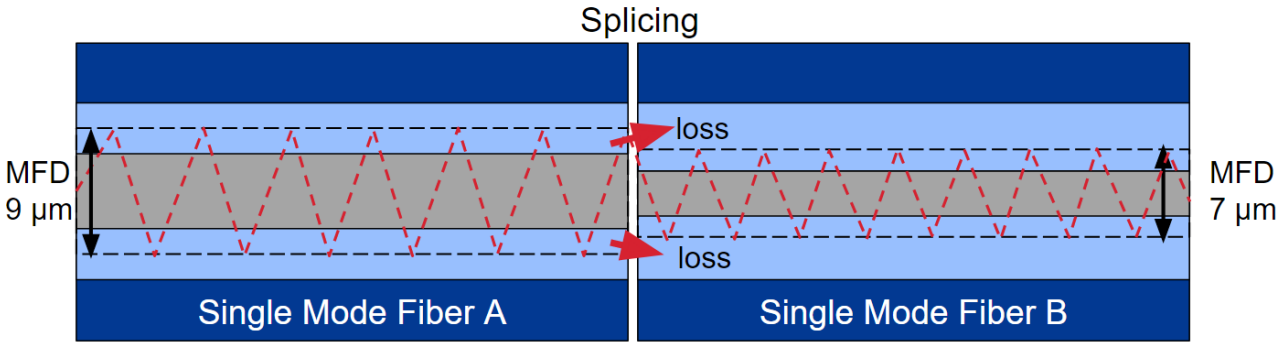

Figure 2: *Diagram of spliced fibers with different MFDs. When two fibers with different MFDs are spliced or coupled, the smaller MFD cannot carry the same amount of light, so loss occurs.*

MFD is an important property of single mode fibers, and it is usually defined as the width of the intensity curve at the $1/e^2$ level, as shown in Figure 1. As light travels through a single mode fiber, it propagates within the core and goes a little bit into the cladding, the material surrounding the core. MFD is the measure of the width of the area over which the light propagates [2]. It can be useful to know the MFD of different fibers at different wavelengths for experiments or setups that involve splicing or coupling different fibers or manipulating the light once it exits the fiber. If two fibers with different MFDs are coupled or spliced, loss will occur, as shown in Figure 2 [3]. Additionally, MFD is used to calculate other properties of the light once it exits the fiber and is manipulated in certain ways, such as with a collimator.

There are many different techniques for measuring the MFD of single mode fibers, but the knife-edge technique was chosen for this work. The knife-edge technique involves using a knife- or razor-edge to incrementally cut off the amount of light exiting a fiber that reaches a power meter. The amount of light that reaches the power meter is measured at each interval that the knife-edge is moved [4]. Compared to other methods of measuring MFD, the knife-edge

technique is inexpensive since razor/knife-edges are cheaper than quality cameras or other equipment [5]. The knife-edge technique is also relatively easy to set up.

III. Experimental Setup/Data-taking Process

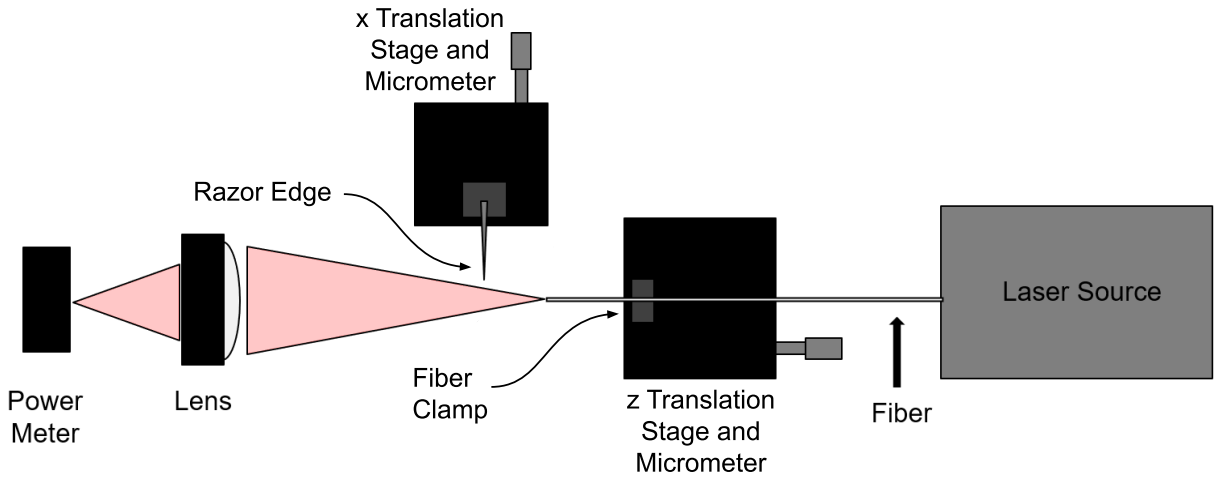

Figure 3: *Diagram of the experimental setup. The test fiber is coupled to the laser source and is held on the z translation stage with a fiber clamp. The razor edge is positioned perpendicular to the test fiber on the x translation stage so that it can be moved to cut off the light emitted from the fiber. That light is focused by a lens into the power meter.*

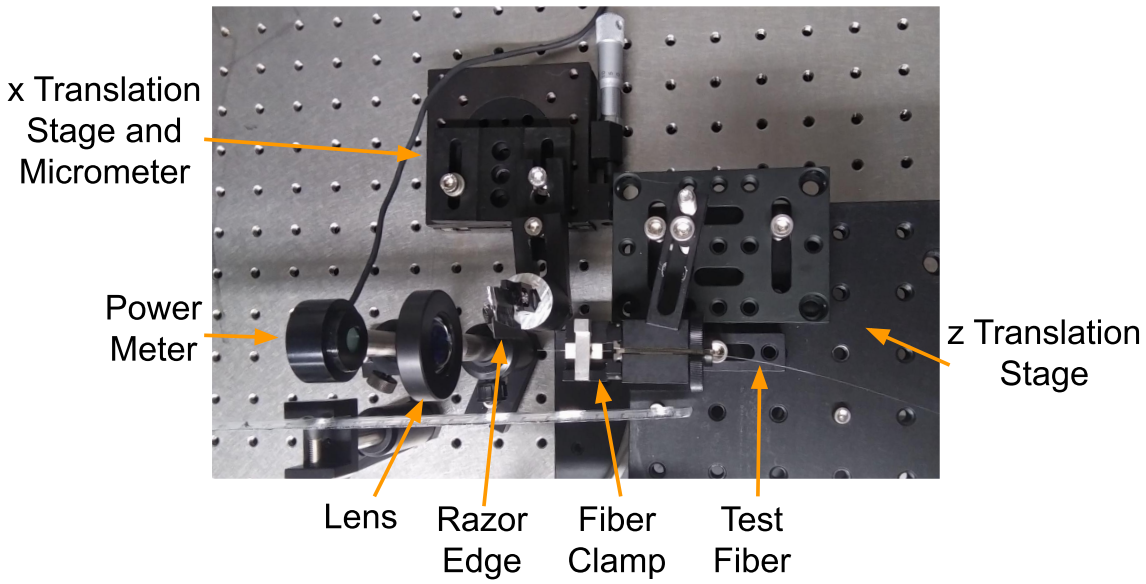

Figure 4: *Photograph of the experimental setup.*

The experimental setup consisted of the fiber under test, a fiber coupled laser source, two translation stages with micrometers, a razor edge, a fiber clamp, a lens, and a power meter (Ophir PD300R-IR), as shown in Figures 3-5. The fiber under test was mounted in the fiber clamp and

aligned such that the lens (f = 25.4 mm) focused all of the light exiting the fiber onto the power meter. The alignment and position of the lens and power meter were checked with an IR card. The razor was mounted in a filter clamp which was secured to the x translation stage that moved perpendicular to the fiber. The z position of the razor edge must satisfy the inequality

$$z > 30w_0^2/\lambda \quad (1)$$

where z is the distance from the fiber tip to the razor edge, w_0 is the mode field radius, and λ is the wavelength [4]. This ensures that the razor edge is sufficiently far from the fiber so that the beam will have a Gaussian shape where data is being taken. The x position of the razor edge was such that, depending on the position of the x translation stage, it could either block all of the light exiting the fiber from reaching the power meter or allow all of it to reach the power meter. The fiber under test was a sample at least 45 cm long of either SM980 or XP1060 spliced to a single mode pigtail. The pigtailed end was butt coupled to one of three fiber coupled laser sources. Three laser sources were used, Innovative Photonic Solutions 1064 nm laser source, a New Focus TLB-6700 tunable laser source, and a 976 nm pump diode. The other end of the fiber under test was stripped and cleaved so that it had a flat edge. The fiber was placed in the fiber clamp so that there was as little fiber sticking out from the fiber clamp as possible, approximately 1-2 cm, and the fiber clamp was secured to the z translation stage.

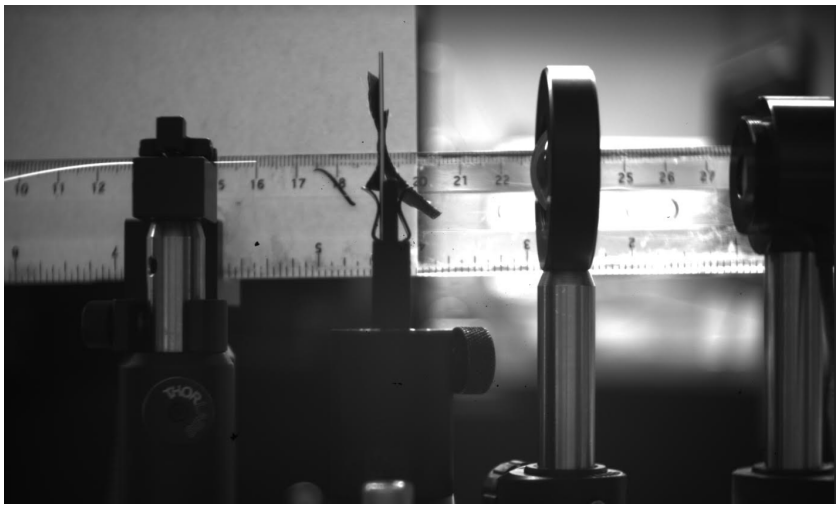

Figure 5: *Camera view of the setup. The camera was used to help measure the z distance. From left to right are the fiber clamp, razor, lens, and power meter. The ruler is behind the setup.*

The distance from the tip of the fiber to the razor edge (*z*) is necessary for calculating MFD, and it must be measured before taking data. A camera (Manta G-145) with a 16 mm TV lens was positioned perpendicular to the test fiber so that the fiber was in focus. An index card and ruler were placed directly behind the fiber. The ruler was used to mark the fiber position and the index card provided a background so that the position of the fiber tip could easily be seen on

the camera. First, the razor edge was moved using the x translation stage to a location in front of the fiber tip; the razor edge was moved to the same micrometer position for each measurement of *z* to decrease possible error that could have resulted from the razor being slanted in the mount. Next, the fiber was replaced with a "dummy fiber" which was a thin piece of wire, approximately 0.5 mm in diameter, that did not bend without significant force. The advantage of a dummy fiber is that it ensures that the flat cleave of the fiber under test is not compromised. The wire was placed in the fiber clamp and the z micrometer was used to move the wire up until it touched the razor edge. The reading on the z micrometer was recorded and the wire was moved away from the razor edge by the desired *z* distance, usually 10 mm. The camera was used to find the position of the wire tip. The camera and TV lens were adjusted so that the wire was in focus. The wire was replaced with the test fiber and the position of the fiber on the ruler was recorded. Since the fiber is extremely thin, an extra light source, such a desk lamp, was sometimes necessary to see the fiber in the camera. Since it was extremely difficult to place the fiber in the same location as the dummy fiber, the tip of the fiber was repositioned with the z micrometer, using the ruler as a guide.

Prior to taking data, the laser source was turned on and left to warm up for approximately 15 minutes. If the z value being used was significantly different from previous data runs, an IR card was used to check the alignment of the lens and power meter. Initially, the data-taking process started with moving the razor so that it blocked all of the light exiting the fiber. This method, as opposed to starting out with the razor blocking none of the light exiting the fiber, allowed the experimenter to see at which x-value the data set should end. By removing an increasing number of data points from both ends of a data set until a significant change in MFD occurred, it was determined that there should be at least 5 data points of a constant power at either end of the data set. Since the razor is placed in a way that guarantees 5 points of constant low power, starting at low power allows for the last data point to be determined by the experimenter. After the range of x-values that should be used for data taking were determined, the data-taking process was started with the razor moved out of the way so that it wasn't blocking any light.

Once the razor edge was in place for the first data point, the average power over 20 seconds was recorded. The x micrometer was then moved 0.50 mm in the direction in which the data was being taken and the process was repeated. In order to block the same amount of room light during each 20 sec interval to reduce error, the person doing the experiment stood at approximately the same location while waiting during the data taking process for each data point. After all data was collected, assuming there was not another run of data collected, the laser was turned off.

IV. Calculations and Results

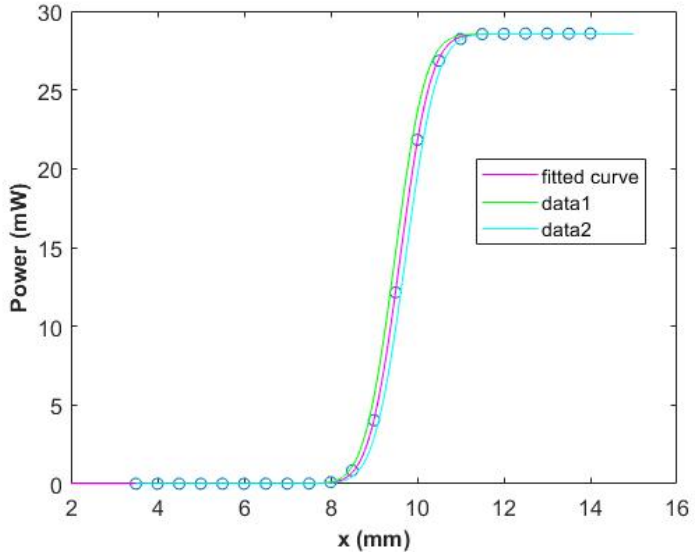

Figure 6: *Graph of data points (open circles) fitted with an error function (fitted curve) and an upper and lower bound (data1 and data2).*

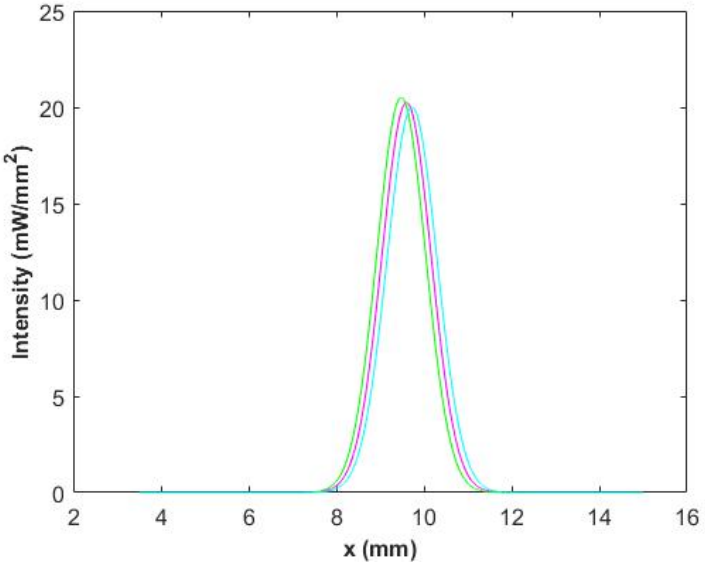

Figure 7: *Intensity vs translation stage position at the location of the razor blade.*

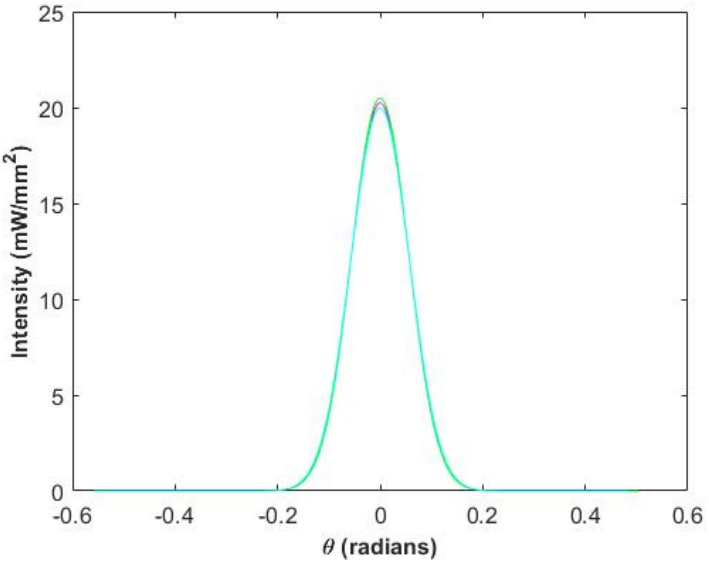

Figure 8: *Intensity vs angular spread θ at the location of the razor blade.*

In order to find MFD from the data, a series of calculations were done. The power vs position data is first fitted with an error function,

$$I = a + b\ \mathrm{erf}(d*x + f) \tag{2}$$

where a, b, d, and f are fitting parameters (Figure 6). The upper and lower bounds of the fitted function are calculated to account for any fluctuation in the laser's power. This data is inherently integrated over position so in order to get intensity vs. position, the numeric derivative over x was found, which results in a Gaussian beam shape (Figure 7).

$$I2 = dI/dx \tag{3}$$

Next, the z measurement was used to calculate the θ, the angular spread, using the following expression

$$\theta = \tan(x/z) \tag{4}$$

where x=0 at peak intensity. Note that x is defined from the location of the peak of the intensity curve, I2. Figure 8 shows the result of this change of variable, I(θ). Now that the I(θ) has been calculated, MFD is calculated using the Petermann II definition of MFD [2].

$$MFD = \left(\frac{\lambda}{\pi}\right)\left(\frac{2\int_0^{\pi/2} I(\theta)\sin(\theta)\cos(\theta)d\theta}{\int_0^{\pi/2} I(\theta)\sin^3(\theta)\cos(\theta)d\theta}\right)^{1/2} \tag{5}$$

where *I(θ)* is the intensity profile shown in Figure 8. The upper and lower bounds of the error function are put through the same analysis to get upper and lower bounds on the MFD.

In order to address potential sources of error in the experimental setup and procedure, the influence of several aspects of the experiment on data was tested. In order to get a baseline of error between trials, MFD was measured from a succession of trials for which nothing about the setup was changed. Next, MFD was measured for a series of trials for which the z was remeasured but kept constant for each trial. This was the dominant source of error and measurements from these trials are reported in Table 1. Then, measurements were performed at different values of z to determine if the z measurement had an impact on MFD. It was found that the value of z didn't have any larger impact on MFD than the error introduced by remeasuring z. This makes sense given that the measurements were made in the far field according to the inequality $z > 30w_0^2/\lambda$. Another potential source of error was if the fiber had an angled cleave. To test this MFD was measured four times with everything kept the same except for rotating the fiber 90° clockwise each trial. Since the MFD wasn't significantly different for each trial, it is suspected that this is not a dominant source of error. Finally, the impact of the length of the test fiber on the calculated MFD was tested to determine if light was coupling into the cladding. Test fibers with lengths 46 cm - 130 cm were tested and it was determined that the fiber length didn't have a significant impact on the calculated MFD.

Fiber Type	Wavelength (nm)	MFD (μm)	Vendor MFD Specification (μm)
1060 XP	1064	6.7 ± 0.1	5.7-6.7 (1060 nm)
SM980	976	5.6 ± 0.2	5.3-6.4 (980 nm)
SM980	1053	6.0 ± 0.1	N/A

Table 1: *Table of final MFD measurements for each fiber-wavelength combination compared to the vendor specifications, if available.*

To determine the final MFD of a fiber at each wavelength, 5-7 data runs were performed and the average and standard deviation for each set of runs was found. For comparison, the error due to power fluctuations between runs was 0.05 μm. As shown in Table 1, the calculated MFD for the 1060 XP fiber at 1064 nm closely agreed with the vendor specification for MFD of that fiber at 1060 nm. The calculated MFD for the SM980 fiber at 976 nm was matched to the vendor specification for that fiber at 980 nm. This demonstrates the accuracy of the setup, data-taking process, and calculations. The MFD of the SM980 fiber, which is a fiber commonly used at LLE, at 1053 nm, was measured to be 6.0 ± 0.1 μm.

V. Conclusion

The purpose of this project was to create a simple setup that could be used to measure the MFD of any single mode fiber at a variety of wavelengths. The setup built and tested here was qualified with two different types of single mode fiber, SM980 and 1060XP. In both cases the MFD was measured to be within vendor specifications.

The next phase for this work would be to create another setup for measuring MFD, such as one using the near-field technique. The near field technique involves focusing the light from a test fiber into a specific camera which takes a detailed picture of the fiber tip in the near field so that MFD can then be measured from this picture. This technique would be more difficult to set up but have an easier data-taking process and offer a 2-dimensional image of the intensity profile, rather than a 1-dimensional image, making it more useful for more exotic fibers that are not rotationally symmetric, like polarization-maintaining fibers. The knife-edge work done here will be critical to validate and test a near-field setup.

VI. Acknowledgements

I would like to first thank my advisor, Sara Bucht, for her unwavering support, patience, and guidance throughout this project; for many reasons, this wouldn't have been possible without her. I'm incredibly appreciative of the experiences I've had and the material that I've learned about. I'm also grateful for the privilege of working in a well-equipped laboratory. I would also like to thank Robert Cuffney for his patience, assistance, and insight. Thank you to Dr. Stephen Craxton for directing and managing the High School Summer Research Program, which gives such amazing opportunities to high school students. This program wouldn't be possible without the work of the technology support team and administrative organizers involved with every aspect of the program. Lastly, I would like to thank my fellow students for their friendship and support.

VII. References

[1] Paschotta, Rüdiger. "Single-mode fibers." *RP Photonics*, https://www.rp-photonics.com/single_mode_fibers.html. Accessed 22 June 2023.

[2] Vastag, Michael R. *Mode Field Diameter and Effective Area*. Corning Incorporated, October 2001.

[3] Franzen, Douglas L. "Precision Measurements on Optical Fibers." *Optics & Photonics News*, May 1991, p. 30.

[4] Otten, William G., et al. "Mode-Field Diameter of Single-Mode Fiber by Knife-Edge Scanning in the Far Field." *Journal of Lightwave Technology*, vol. LT-4, no. 10, 1986, pp. 1576-1577.

[5] de Araújo, Marcos, et al. “Measurement of Gaussian Laser Beam Radius Using the Knife-Edge Technique: Improvement on Data Analysis.” *Applied Optics*, vol. 48, no. 2, 2009, p. 393.

Mitigating Rayleigh Taylor Instabilities in the Deceleration Phase of Inertial Confinement Fusion

John Giess

McQuaid Jesuit High School

LLE Advisors: Dr. Valeri Goncharov, Dr. Ka Ming (Jack) Woo

April 2023

Laboratory for Laser Energetics
University of Rochester

1 Abstract

The Rayleigh Taylor (RT) hydrodynamic instability can reduce the temperature in the hot spot and limit target performance in inertial confinement fusion. The RT instability is formed when a lower density material pushes on a higher density material. RT growth amplifies shell imperfections at the outer surface during the shell acceleration and at the inner surface during the deceleration. We investigated mitigation techniques for RT perturbation amplification in the deceleration phase. These include the mistiming of shocks to increase the entropy and reduce the density at the inner part of the shell. These shocks propagate into the shell at the beginning of the implosion. In a nominal design, the shocks are timed so they all merge at the shell's inner surface. We changed the height of the foot during the early part of the laser pulse in order to see the effect of the shocks merging inside the shell. We then calculated the RT growth rate using the change in the density scale length and the inner radius. We found a design with a high foot that has a larger density scale length and limits RT growth.

2 Introduction

2.1 Inertial Confinement Fusion

At the 60-beam OMEGA Laser Facility, inertial confinement fusion (ICF) implosions are created with direct beam irradiation on a spherical cryogenic target. In this process, extremely high densities, pressures and temperatures are reached allowing for the fusion of particles in the inner core of the target. The target typically contains a combination of deuterium and tritium (DT), two hydrogen isotopes, in a gaseous form at the center of the target and in a frozen form surrounding this gas. A layer of plastic, glass or other material encloses the target forming an outermost layer. For the purposes of this study, a plastic layer, which is known as an ablator, was

used and two different targets with different layers were used for simulation. However, these targets will not be perfectly spherical as they often have imperfections that are amplified through the ICF implosion. In the beginning of an ICF implosion, the laser irradiation is absorbed in the outer shell layer resulting in the ablation of the outer material. This force accelerates the target's shell inward. The shell then moves into the deceleration phase as the low density plasma hotspot region in the center pushes against the higher density outer region. The target's shell is slowed down during the deceleration phase as return shocks move through the shell. The shell continues to compress and the internal gas grows in temperature creating a "hot spot" region where fusion reactions can occur. After the shell decelerates, peak compression occurs. Bang time, the time at which the fusion rate is maximum, occurs when the fuel reaches maximum compression and this is often called the stagnation point. In this phase, if the self heating rate through alpha particle deposition is greater than the energy loss rate within the hot spot, a burning plasma state occurs that triggers an unstable thermonuclear burn wave. Much higher temperatures and neutron yields are the result. A burn state is required to reach ignition where output exceeds input energy.

2.2 Rayleigh-Taylor Growth

We can see the effects of Rayleigh Taylor (RT) instability, which occurs when a lower density material pushes on a higher density material. It leads to exponential growth in perturbations. It first occurs on the outer surface of the target during the acceleration phase. Perturbations are amplified as the lower density laser plasma pushes against the more dense outer shell. The instability also occurs later, during the deceleration phase. The RT growth is undesirable for two reasons. First, during the compression, the shell's kinetic energy is wasted to amplify perturbations instead of uniformly compressing the target. Second, by the time of peak

compression, the cold dense shell mixes with the inner hot spot region lowering its temperature and therefore lowering the fusion reaction rates.

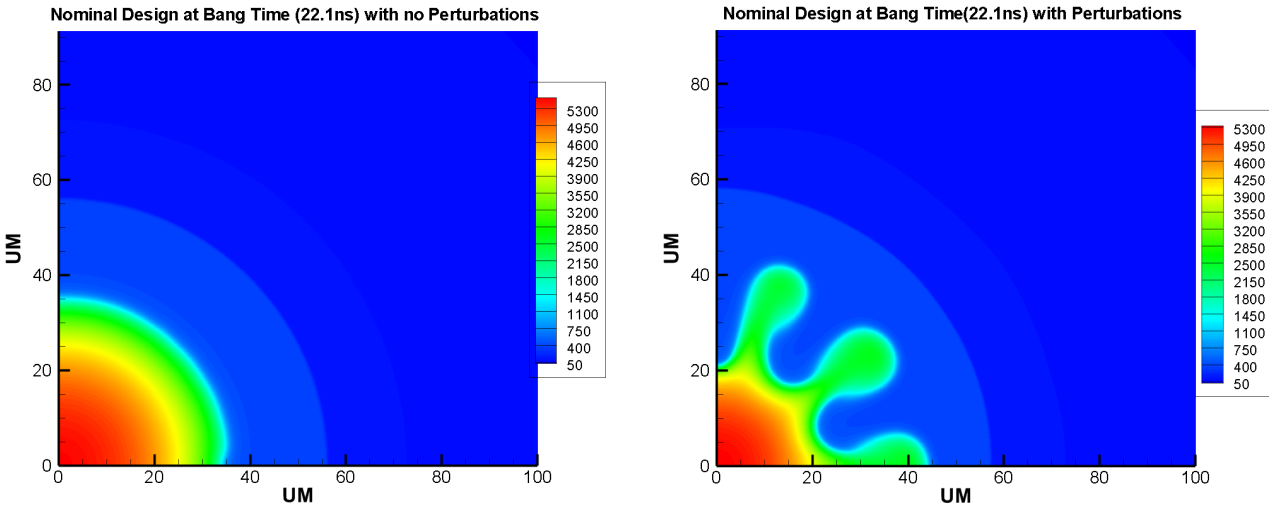

(a) (b)

Figure 1. (a) Temperature contours (in eV) at bang time for a target simulated using the code DEC2D with no RT perturbations. (b) Temperature contours at bang time for a target with RT perturbations. This target has a lower internal temperature. (The temperature scale is the same for both figures)

The RT instability is illustrated in Figure 1 for two simulations, one (Figure 1a) for a target without perturbations and the other (Figure 1b) for a target with perturbations. These temperature contour plots are shown at bang time with distances in μm using Cartesian geometry. The simulations were done by first running the 1D radiation-hydrodynamics code LILAC [1] for the entire length of the pulse. Profiles of required data were transferred to the 2D simulation code DEC2D [2] at the beginning of the deceleration phase and a perturbation on the density, pressure,

or temperature with a selected mode number was then added. DEC2D followed the implosion through the deceleration phase to slightly after the bang time. The green fingers are where there is higher temperature and between them the blue fingers indicate higher density. The target imploded contained an inner gaseous DT region of radius 850 μm, enclosed by a frozen DT region which is 450 μm thick, followed by a thin outer plastic shell which is 110 μm thick. The pulse shape used is shown in Figure 2. We can see the decrease in size of the hot spot at bang time, the area inside the yellow contour in Figure 1, whose radius is approximately 1.8% of the size of the initial target's radius 1410 μm, as it is around 25 μm in Figure 1(a) and 17.5 μm in Figure 1(b).

2.3 Adiabat Shaping

There are many techniques to reduce RT growth. The approach we analyzed was changing the shape of the pulse. [3] One method is called a decaying shock, where a prepulse causes a decaying shock in the shell. Another is the relaxation method, where a prepulse is used and the adiabat is shaped by the foot of the main pulse.[4] This adiabat, defined as the pressure divided by the Fermi pressure (the minimum pressure due to degeneracy), is given by the equation [5],

$$\alpha = \frac{P(Mb)}{2.18\rho(g/cc)^{5/3}}$$

with the pressure (P) given in megabars and the density (ρ) given in (g/cc). A higher adiabat means that we will have higher internal temperatures which would lower the density gradient and limit RT growth. We can change the adiabat to cause these conditions by using various shaping

techniques which modify the pressure and density in different regions.

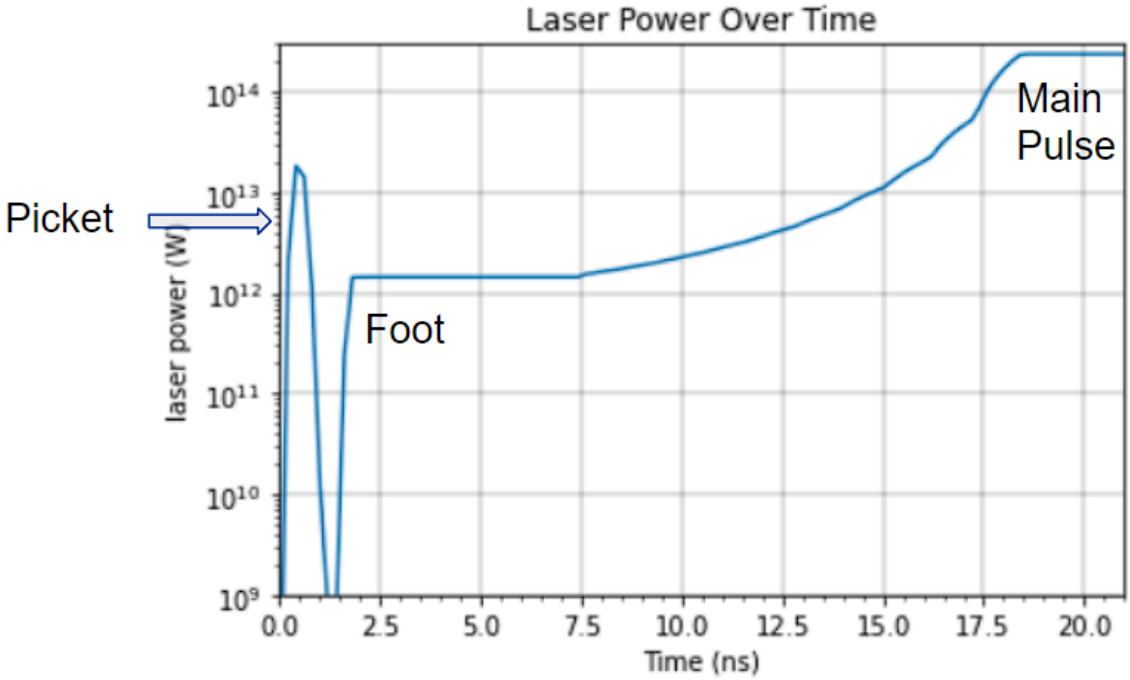

Figure 2. The initial laser pulse design used, with the strong prepulse (picket), foot (that drives a supported shock) and main pulse labeled. The main pulse continues until 22.5 ns. The foot is characterized by a power of 1.45 TW.

Our design used the laser pulse shown in Figure 2, which included a picket, a foot, and a main pulse that is ramped up to and begins at 18.6 ns. Both the height and duration of the foot and picket can be changed by adjusting the laser power. Through studies of 1D LILAC simulations, we decided to focus on modifying the height of the foot, leaving the picket pulse unchanged, to shape the adiabat. In the nominal design, the height and start time of the foot and the picket were arranged so that these two shocks would merge at the shell's inner surface. We looked at the effect of raising the height, or laser power, of the foot, so that the shocks would instead merge inside of the shell of the target.

2.4 Rayleigh-Taylor Growth Calculations

The main goal of these shaping techniques is to reduce the RT growth, which can be linearly modeled by the equation,

$$perturbation\ growth = exp \int_{t_{Begin}}^{t_{End}} \gamma\, dt$$

where the growth rate is given by

$$\gamma = \sqrt{\frac{kg}{1 + kL}}$$

with $k = \frac{2\Pi}{\lambda}$ where λ is the wavelength of the perturbation, $\lambda = \frac{2\Pi R}{l}$ where l is the mode number (the number of wavelengths going around the circumference), R is the shell radius and L is the minimum value of the density gradient scale length at the unstable interface, which for the deceleration instability is the boundary between the hot spot and the imploding shell. The quantity g is the shell acceleration or deceleration and is analogous to gravity. The beginning time t_{Begin} is the start of the deceleration phase and the end time t_{End} is bang time. By using this formula, if we are able to maximize the density scale length, we can therefore minimize the growth of perturbations if the duration of the acceleration phase does not change. This can be done by reducing the difference in densities between the hot spot and the imploding shell through adiabat shaping techniques. However, if the time it takes to reach the bang time increases with the increase in density scale length, the perturbations will have more time to grow, therefore minimizing the effect of a larger density gradient scale length.

2.5 Simulations

Two different simulation codes were used to evaluate the effects of our adiabat shaping techniques. The first used was LILAC. By simulating different input laser pulse shapes and target conditions this code allowed us to view the effect of the shocks through changes in pressure and density over time. By modifying both of these inputs, the energy output (neutron yield) and changes in bang time (the stagnation point) could be quickly analyzed to compare with early designs. Profiles of promising 1D simulations were then imported into DEC2D using output from the LILAC simulation at the beginning of the deceleration phase and the addition of a 2D perturbation. DEC2D allows us to directly analyze the effects of these perturbations. The sizes of the perturbations were then measured over time, which allowed for a comparison of the results from the different designs.

3 Initial Optimizations

3.1 Initial Parameters and Shell Design

For these tests a NIF-scale implosion was simulated. The initial target design contains an inner gaseous DT region of radius 850 μm, enclosed by a frozen DT region which is 450 μm thick, followed by a thin outer plastic shell which is 110 μm thick. Burn conditions would begin when the neutron yield was around $10^{17}$and this would lead to a rapid increase in the yield to around 10^{19}. As shown in Figure 2, the length of the laser pulse was 22.5 ns with a picket, a foot pulse, and a main pulse with a maximum power of 240 TW. In order to achieve a greater density scale length the height of the foot pulse was systematically increased in LILAC simulations.

3.2 1D simulation results

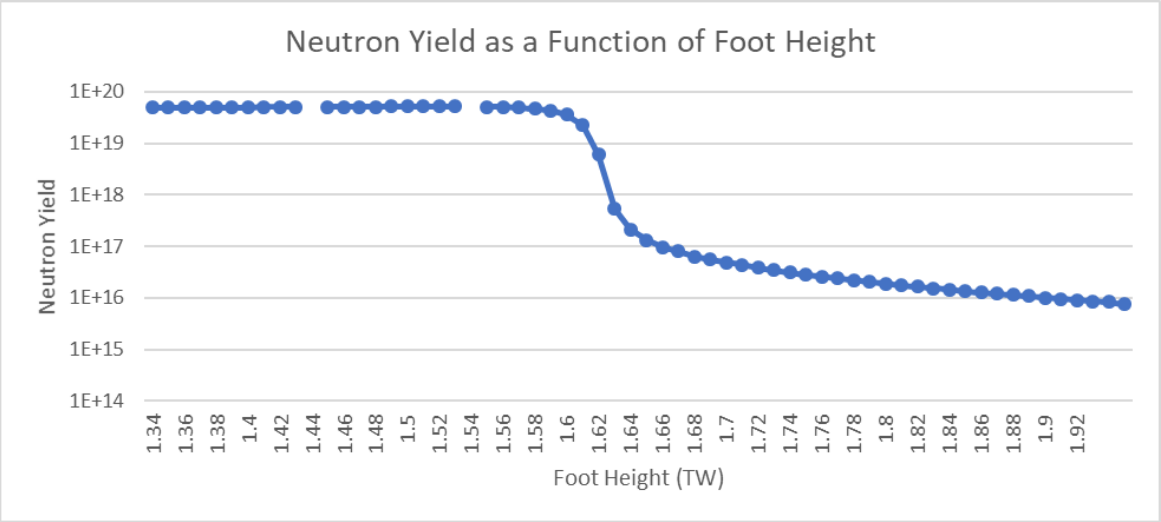

Figure 3. The neutron yield as a function of the power in the foot. Each dot represents an increase in the height of the foot by 10 GW.

As seen in Figure 3 the neutron yield decreased slightly as the height of the foot increased until the height of the foot reached 1.62 TW, where the neutron yield had a steep drop off. This drop off represents the target not reaching burn conditions. Through this initial round of testing we identified the range of possible foot heights to be from 1.45 to 1.62 TW. Also, as the height of the foot increased, so did the density scale length. We ruled out foot heights lower than 1.45 TW, which was the foot height in our nominal design, because when the heights were lowered from the nominal height the density scale length decreased. Our best design increased the average density scale length from 2.3 to 3.6 μm. This is promising because 1D LILAC simulations are

not affected by the perturbations. So even though the 1D simulations showed a lower neutron yield or output, it is likely that the increased scale length could lead to reduced perturbations and therefore more stability in the 2D simulations.

3.3 2D simulation results

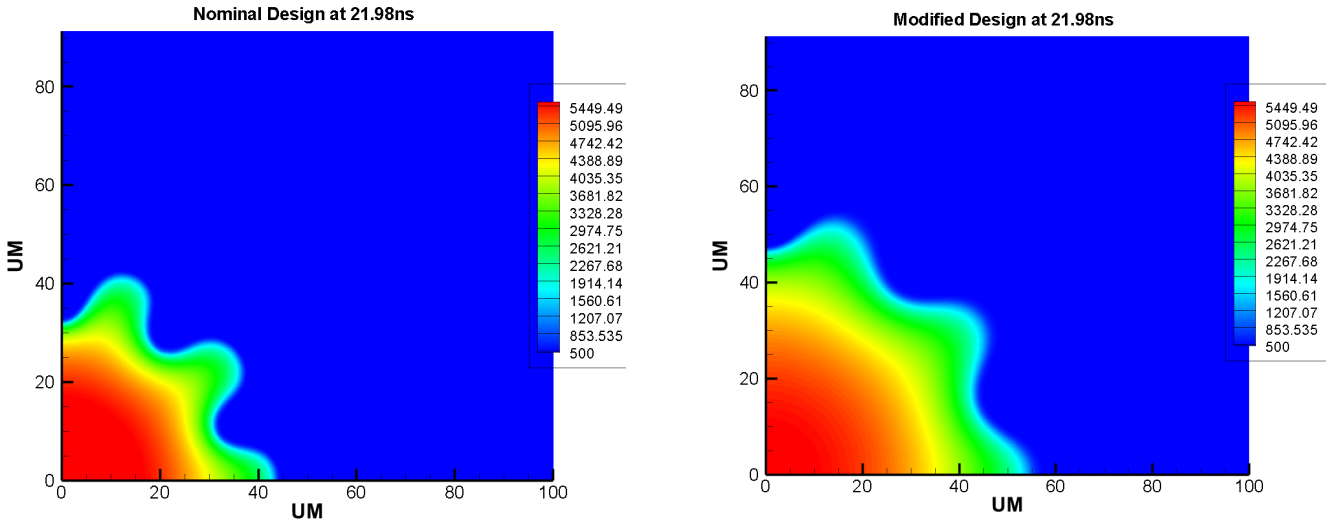

Figure 4. Temperature contours at 21.98 ns for the nominal design, the initial design (left) and the modified design, the higher foot design (right). The temperature is plotted in electron volts.

The anticipated improvements were indeed seen in the 2D simulations, where the rate of growth of the perturbations was greatly decreased in the higher foot designs by the increased density scale lengths at similar times. This can be seen in Figure 4, which compares the temperature contours for the nominal design (foot height 1.45 TW) and a modified design (foot height 1.61 TW) at the same time (21.98 ns). The perturbations are much smaller in the modified design. However, the problem was that the bang time increased by 0.22 ns. This time increase was

because the target became harder to compress. As a result, the perturbations had significantly more time to grow in all of the higher foot designs and eventually became larger than the perturbations in the nominal design.

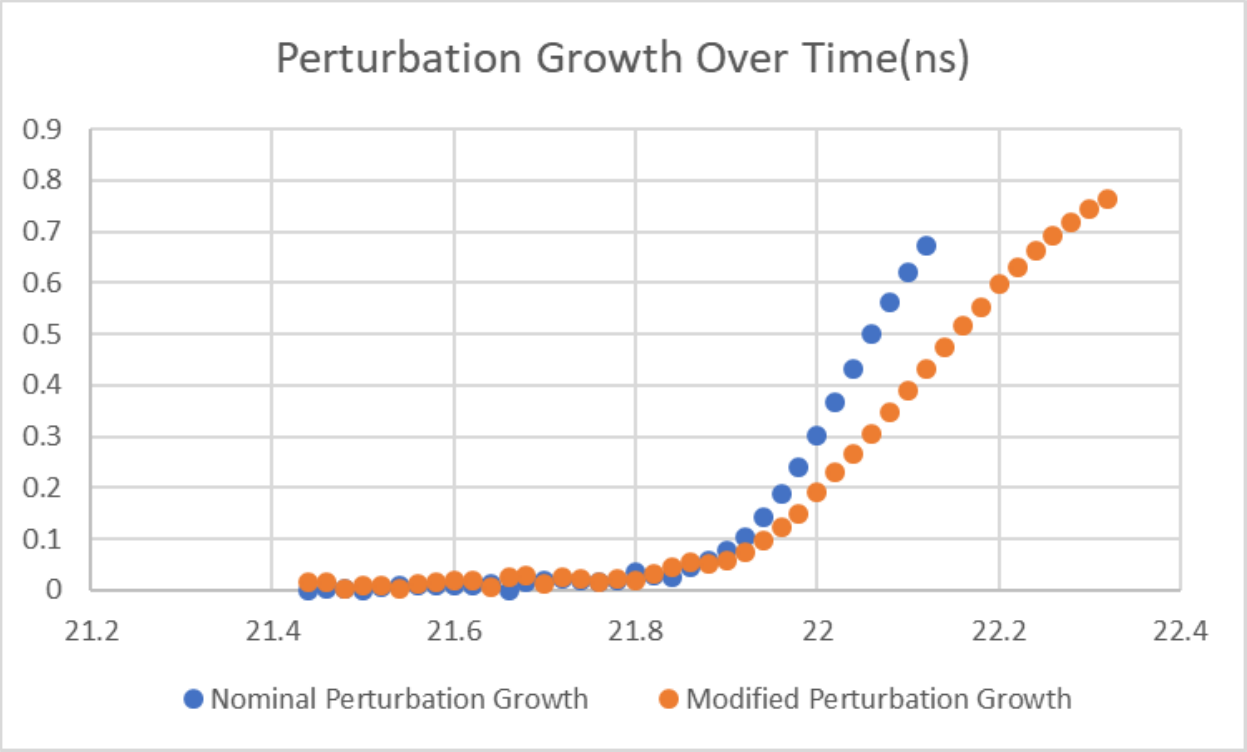

Figure 5. Perturbation growth for the nominal and modified (higher foot) designs as a function of time(ns). The data begin at the start of the decceleration phase at 21.44ns and end at bang time. Perturbation growth is calculated as the radius to the edge of the perturbation divided by the perturbation wavelength.

This is illustrated in Figure 5, which plots the perturbation growth as a function of time for the nominal and modified designs ending at bang time. The edge of the perturbation can be seen in Figure 4 where the temperature contour shows light blue. It is seen that the nominal design had less growth than the higher foot design by the time they both reached bang time. It can therefore be concluded that the increase in foot height can lead to a decrease in the rate of perturbation

growth because of the lower density slope, but an increase in the bang time. Using these results we hypothesized that if we could decrease the time it takes for the target to implode using a modified target design we could mitigate this increase in time and utilize the improved scale length and growth rate to have less total perturbation growth.

4 Improved Shell Design

4.1 Parameters and 1D Results

The new shell design had a much smaller DT ice region of 180 μm thickness (reduced from 450 μm) with a gaseous region of radius 1305 μm (increased from 850 μm), so that it would implode earlier than the previous design. The plastic layer was kept at the same thickness of 110 μm to absorb the laser and ablate off, causing the inward shell acceleration.

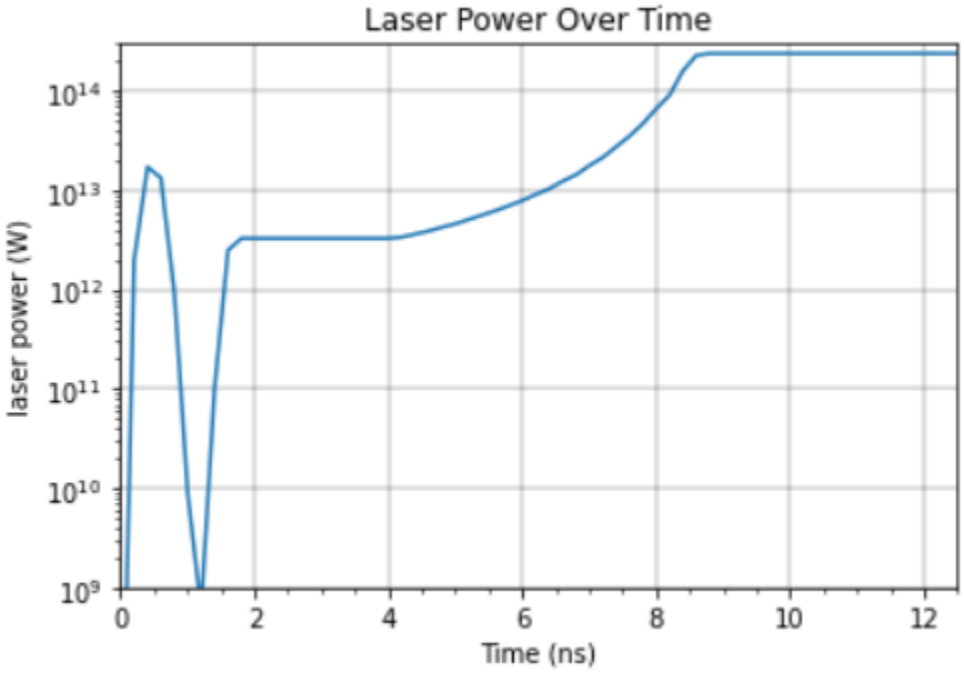

Figure 6. The shorter laser pulse for the thinner shell design.

The nominal laser pulse design was modified along with the shell to be much shorter to account for the quicker implosion (see Figure 6). The heights of the main laser pulse and picket were the same as in the previous design (Figure 2). Using this new design, multiple foot height changes were simulated with LILAC. These initial simulations showed a large increase in density scale length compared with the nominal design as well as only slight bang time increases. The average density scale length from the start of deceleration to bang time was almost double in the thinner-shell design.

4.2 Results

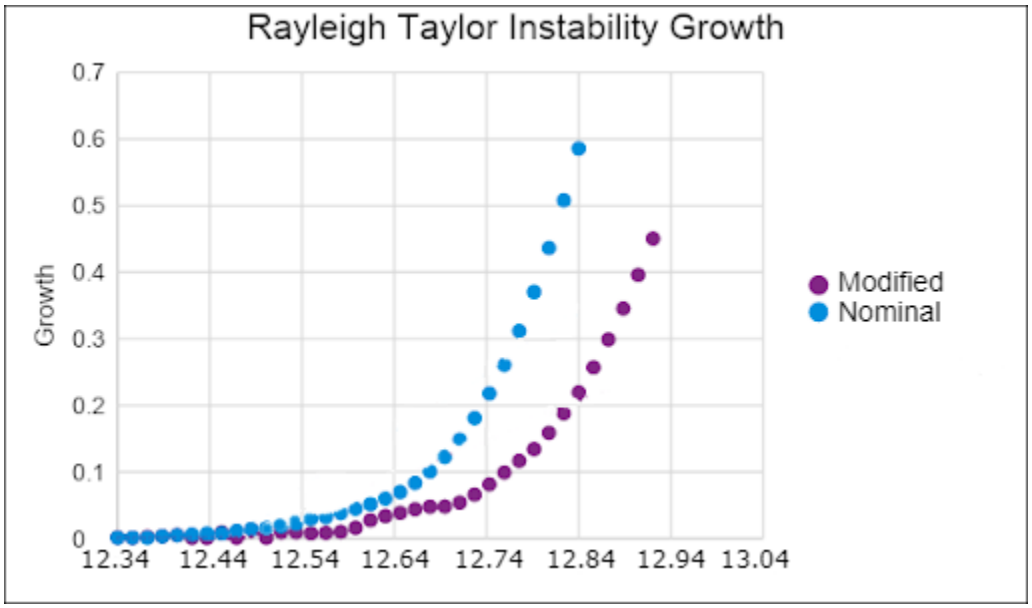

Figure 7. Perturbation growth for the nominal and modified (higher foot) designs as a function of time (ns) for the shorter laser pulse. As in Figure 5, the data runs from the start of deceleration until the bang time. Here the modified design has a later bang time, but smaller overall growth.

Similarly to Section 3 we considered two pulse shapes: nominal (foot height 3.7 TW) and modified (foot height 5 TW). Figure 7 is the same as Figure 5, but for the shorter laser pulse. It

shows that although our higher foot design took longer to reach bang time the perturbation growth was still ultimately less than for the nominal design. Therefore, because the perturbation growth was minimized while still reaching burn conditions, the design became more stable due to the much higher density scale length.

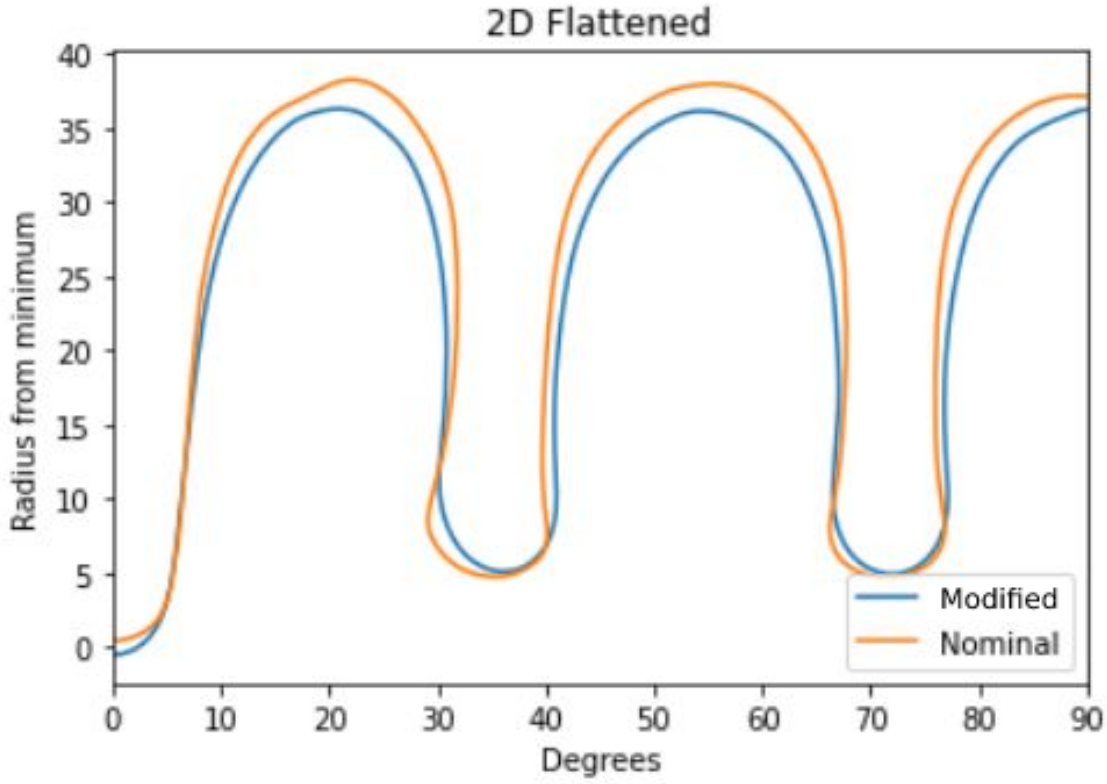

Figure 8. A flattened comparison of the perturbations in the nominal design (orange) and the modified design (blue) of Figure 7 at bang time, plotted against angle from the vertical in the temperature contour plot. Perturbation radius from the minimum is calculated as the distance from the center to the edge of the perturbation minus the lowest part of the perturbation for a DEC2D plotted temperature contour. This is illustrated in Figure 1(b) where the maximum radius of the perturbation would be approximately 42 μm and the lowest part of the perturbation is 21 μm.

Figure 8 shows that there was a reduction in the RT growth; however, due to the time increase this reduction is very minimal. Also, this higher foot design had a slightly lower neutron yield output. The curves show a minimal reduction while Figure 7 shows a greater reduction because the results in Figure 7 used a higher initial perturbation level than the simulation shown in Figure 8. This shows that at higher levels of perturbation the reduction techniques have a greater mitigating effect in relation to the nominal design.

To further improve the design, more precise tunings could first be used. This could be done through utilization of a neural network or gradient descent optimization while modifying the height and space between the picket and the foot. Other modifications, such as the type of outer plastic as well as different target shapes, could be used to help with stability and neutron output.

6 Conclusions

RT growth leads to a waste of the shell's kinetic energy that could otherwise be used to compress the hotspot and a cooling effect within the hot spot region. To reduce the growth of these perturbations, adiabat tuning methods can be used. We modified the height of the foot to make the shocks merge in the shell of the target, increasing the density scale length and reducing the RT growth rate. Different foot heights were simulated in 1D simulations that still reached burn conditions. The density scale length was found to increase as expected. However, 2D simulations showed that while the density scale length was increased and the growth rate was decreased, the implosion took longer, which meant that the total growth of the perturbations increased. Through the use of a new, thinner DT ice layer, a higher foot design was developed that decreased the RT growth rate and also had an earlier bang time than the previous designs. This design showed a slight perturbation reduction, but due to the substantial increase in density scale length for these

higher foot designs, additional optimization could be used to produce a larger perturbation reduction.

7 Acknowledgements

Massive thanks to Dr. Woo and Dr. Goncharov. They spent countless hours teaching me about the fundamentals of fusion and shockwaves and mentored me throughout this project. Dr. Woo also spent additional time helping me learn Python and the various simulators. Many thanks to Dr. Craxton for the time he put in to organize the program. I would also like to thank Ms. Truebger for helping to make the program run smoothly as well as Yousef Lawrence for his initial guidance and materials. Lastly, thanks to all of the other students in the program for their help and making the eight weeks of the summer so enjoyable.

8 References

1. J. Delettrez, R. Epstein, M. C. Richardson, P. A. Jaanimagi, and B. L. Henke, “Effect of Laser Illumination Nonuniformity on the Analysis of Time-Resolved X-Ray Measurements in UV Spherical Transport Experiments,” Phys. Rev. A **36** (8), 3926-3934 (1987).
2. K. M. Woo, R. Betti, D. Shvarts, A. Bose, D. Patel, R. Yan, P.-Y. Chang, O. M. Mannion, R. Epstein, J. A. Delettrez, M. Charissis, K. S. Anderson, P. B. Radha, A. Shvydky, I. V. Igumenshchev, V. Gopalaswamy, A. R. Christopherson, J. Sanz, H. Aluie. (2018) Effects of residual kinetic energy on yield degradation and ion temperature asymmetries in inertial confinement fusion implosions. *Physics of Plasmas* 25:5, 052704.

3. K.S. Anderson. *Adiabat shaping in direct-drive inertial confinement fusion implosions*. Ph. D. thesis, University of Rochester, New York, Jan. 2006.
4. R. Betti, K. Anderson, J. Knauer, T. J. B. Collins, R. L. McCrory, P. W. McKenty, S. Skupsky. (2005) Theory of laser-induced adiabat shaping in inertial fusion implosions: The relaxation method. *Physics of Plasmas* **12**:4, 042703.
5. S. Atzeni and J. Meyer-ter-vehn, The Physics of Inertial Fusion: Beam Plasma Interaction, Hydrodynamics, Hot Dense Matter, International Series of Monographs on Physics (Oxford University Press, Oxford, 2004).

Characterizing a Cryosorption Pump for Collecting Tokamak Exhausts

Samuel Gray

Brighton High School

Advisors: Walter Shmayda and Eric Dombrowski

Laboratory for Laser Energetics

Rochester, New York

January 2024

I. Abstract

SPARC, a high-field toroidal tokamak being constructed by Commonwealth Fusion Systems, will utilize the fusion reaction between tritium and deuterium. The exhaust gas contains hydrogen isotopes, helium ash, and inert gases used to control the plasma. High-vacuum turbomolecular pumps evacuate this gas from the torus. Cryosorption pumps accept gas from these pumps and deliver the effluent to the Torus Exhaust Purification system, where unspent hydrogen is recovered and purified. Cryosorption pumps can selectively pump hydrogen at high speeds in the presence of inert gases. A novel prototypic cryosorption pump was constructed and packed with molecular sieve 4A that is cooled to liquid nitrogen temperatures (-196 °C). The pump design requires a hydrogen capacity of 28 sL with an effective pump speed of 120 sL/second at 1 torr under predicted conditions. Its hydrogen capacity and pumping speed below 1 torr were measured to determine viability in the final application. Precooling with helium was found to have a thermalizing effect in the pump, allowing for a 1,740 % increase in hydrogen capacity (0.25 sL to 4.6 sL) at a pumping speed of 0.5 sLpm. Future experiments will test alternative cooling systems to maximize cooling uniformity during pump operation.

II. Introduction

Commonwealth Fusion Systems is a startup company based in Cambridge, Massachusetts with the goal of demonstrating the viability of fusion as a commercial energy source. They have begun construction of SPARC, a high-field, toroidal, magnetically confined fusion device (*see figure 1)*. SPARC will use novel high-temperature superconducting magnets to confine plasma and will utilize the fusion

reaction between the components of deuterium-tritium (DT) fuel.[1] Gaseous DT will be injected into the device, whereupon the fuel mixture is heated to tens of million degrees Celsius. This is achieved by running high current through the gas (induced by a changing magnetic field in the central coil), high frequency electromagnetic waves similar to those in a microwave oven, and injection of high-speed deuterium atoms.[2]

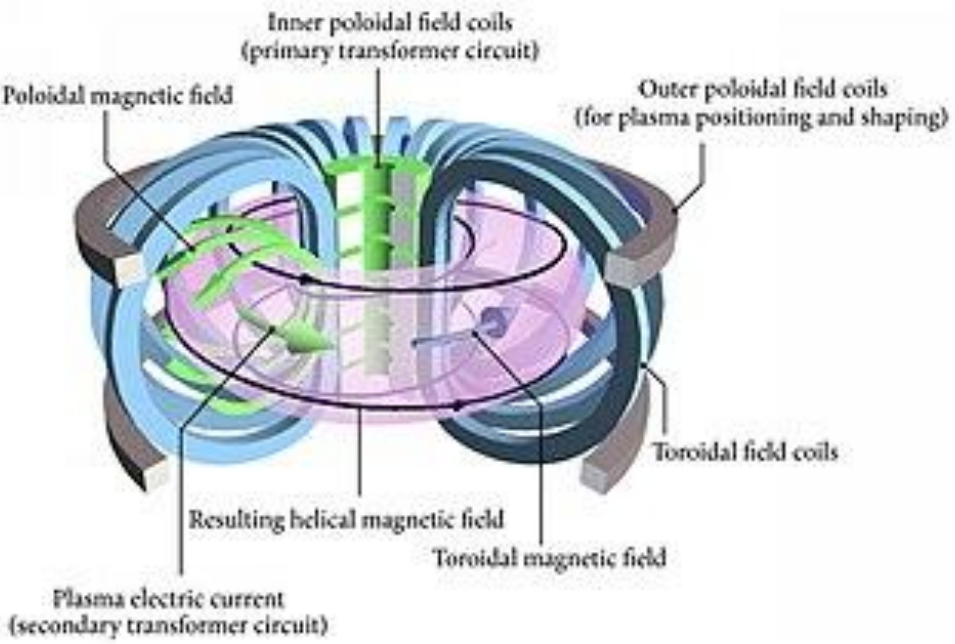

Figure 1.
High-level overview of the magnetic confinement of plasma in a toroidal fusion reactor like SPARC. This figure demonstrates how the toroidal and poloidal magnetic fields allow researchers to confine and form the toroidal plasma shape as well as how the central coil acts as the primary of a transformer to induce high current in the plasma "coil," which acts as the secondary.

At these high temperatures, the DT mixture will turn into plasma, which can be confined and compacted by high strength magnetic fields shown in figure 1. Under these conditions, D and T atoms will collide with each other with sufficient energy to

overcome Coulomb repulsion (the effect of like charges repelling) and fuse. When the hydrogen nuclei combine, they form a single helium nucleus, which releases around 18 MeV and a free neutron each reaction due to the lower binding energy of helium.[3] The purpose of SPARC is to demonstrate this fusion reaction and prove that a net energy gain can be achieved.

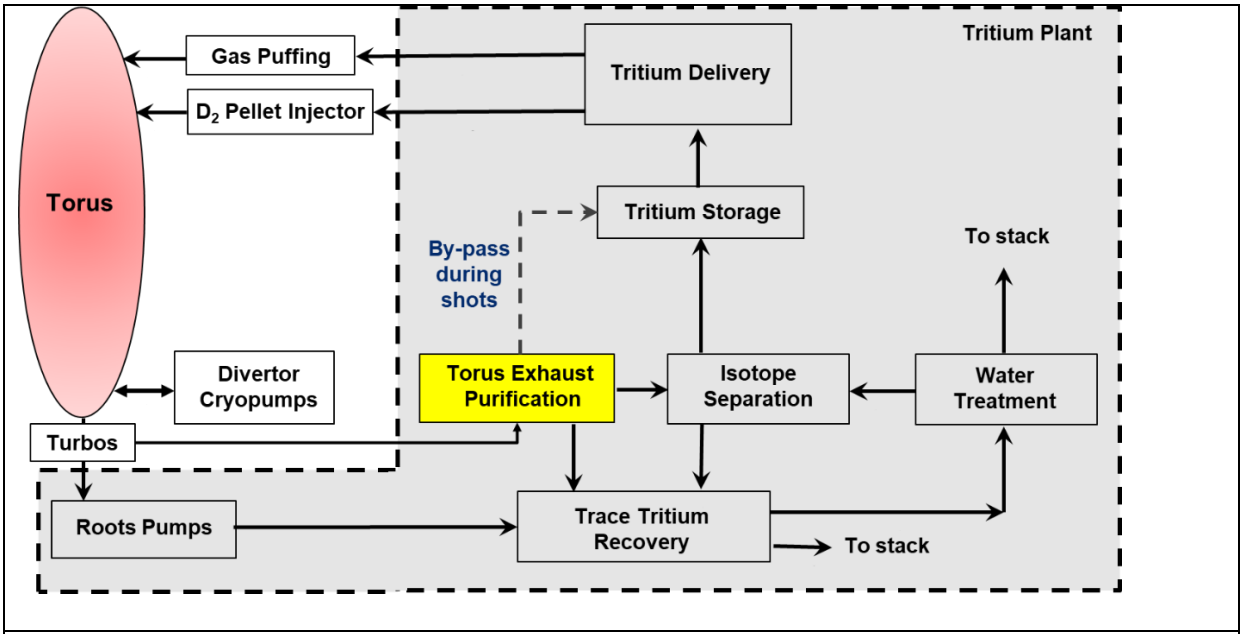

Figure 2.
Schematic diagram[4] of the tritium handling infrastructure to be used in SPARC. After a shot, turbomolecular pumps evacuate the torus. In low tritium operation, exhaust is sent directly to Trace Tritium Recovery (TTR). When there is high tritium pressure, exhaust is handled by Torus Exhaust Purification (TEP). This system separates hydrogen species (which are sent to isotope separation) from waste gas (which is sent to TTR). At isotope separation, tritium and deuterium are separated from protium (hydrogen with one proton and no neutrons in its nucleus) and the correct DT mixture is sent back to the torus to be used in subsequent shots.

As this reaction occurs, helium and inert gasses used for cooling build up in the reactor, necessitating a system to collect and purify exhaust gasses. Since only a small amount of DT is consumed in each shot, SPARC must also have the ability to recover unspent fuel from the effluent exhaust gas mixture. The Torus Exhaust Purification (TEP,

see figure 2) system is being developed by LLE to separate hydrogen species from waste gas. During high tritium pressure operation, effluent from the torus is pumped into TEP by high-vacuum turbomolecular pumps. A high-speed secondary pump is needed to maintain a low pressure at the effluent side of the turbo pumps and collect a volume of hydrogen and deliver it to TEP when needed. A prototypic cryosorption pump was tested to determine its viability in this application.

The torus turbomolecular pumps evacuate gas from the reactor. These pumps require vacuum to be pulled on the exhaust side; the requirement for SPARC is a maximum exhaust pressure of 1 torr. Cryosorption pumps are used for this application not only for their ability to collect hydrogen from the torus effluent stream, but also for their lack of hydrocarbon oil that most other pumps use. Hydrocarbons introduce contaminants which can be eliminated by using cryosorption pumps.

These pumps utilize cryosorption, which is the adsorption of gas onto the surface of a material at cryogenic temperatures (-196 °C). [5] The pump is packed with molecular sieve 4A, a highly porous material having ample surface area which hydrogen can be deposited onto. Characterization of this pump will test the effectiveness of the cooling system to bring molecular sieve to cryogenic temperature, and the ability of the heating system to recover deposited hydrogen. It will also measure the hydrogen capacity at pressures below 1 torr with the goal of reaching 28 sL.

III. Experimental Setup

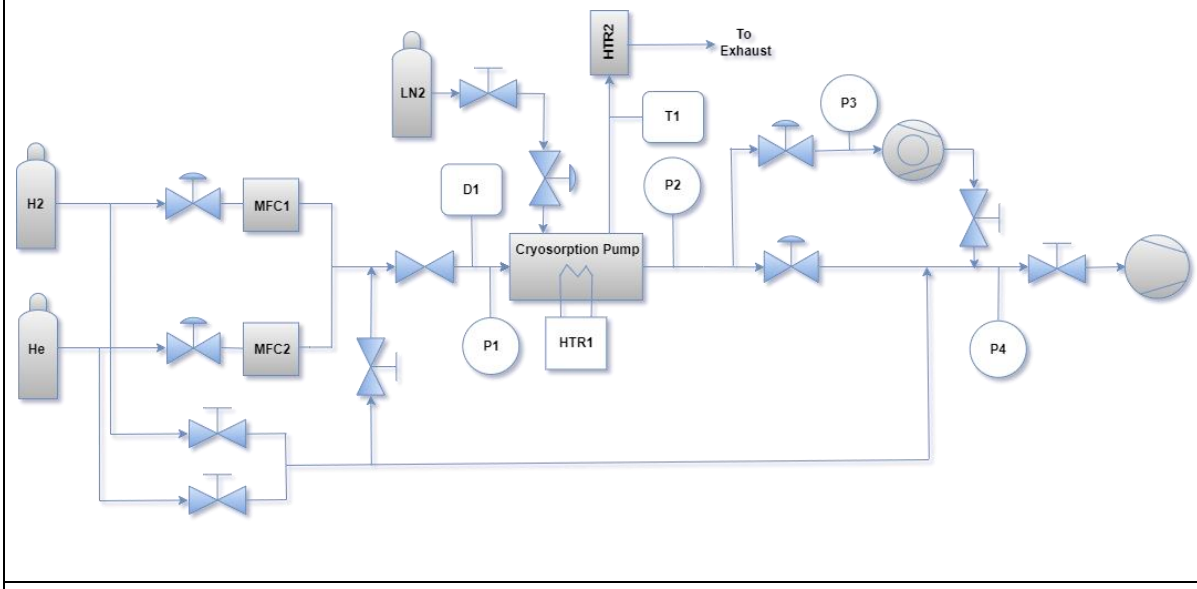

Figure 3.
Schematic of the experimental test stand to characterize the cryosorption pump.

The experimental test stand (*see figure 3*) contains 2 mass flow controllers (MFC1 and MFC2) that can supply precise amounts of hydrogen (H2) and helium (He) to the cryosorption pump. Just upstream of this pump, the influent dewpoint (D1) and pressure (P1) are measured before entering the cryopump. This pump contains an internal heater (HTR1) as well as an internal liquid nitrogen (LN2) coil that heat the molecular sieve during bakeout and regeneration and cool it for actual operation. Liquid nitrogen is boiled off at the effluent (HTR2) and exhausted. Temperature (T1) is monitored here to make sure that liquid nitrogen is not leaking out of the test stand. The cryopump is backed by a turbo pump and roughing pump and the system can be configured to use one or both. The

pressures at each of these pumps (P3, P4), including the cryopump (P2) are measured as well.

IV. Temperature Control of Cryosorption Pump

Bakeout of the cryopump (*shown in figure 4a*) involves heating of the molecular sieve to 400 °C while drawing vacuum downstream of the pump. This is required to completely purge the pump of all gas adsorbed to the molecular sieve as well as to remove water and inert gasses that may be present. Over the course of 50 minutes, the temperature was raised to the target temperature with internal heaters as well as external heater tape to ensure uniform heating of the molecular sieve. The temperature was measured with 3 thermocouple bundles: one at the center, one in the middle, and one towards the outer edge of the pump. Each bundle contains 3 thermocouples to measure temperature at 3 different depths: top, middle, and bottom.

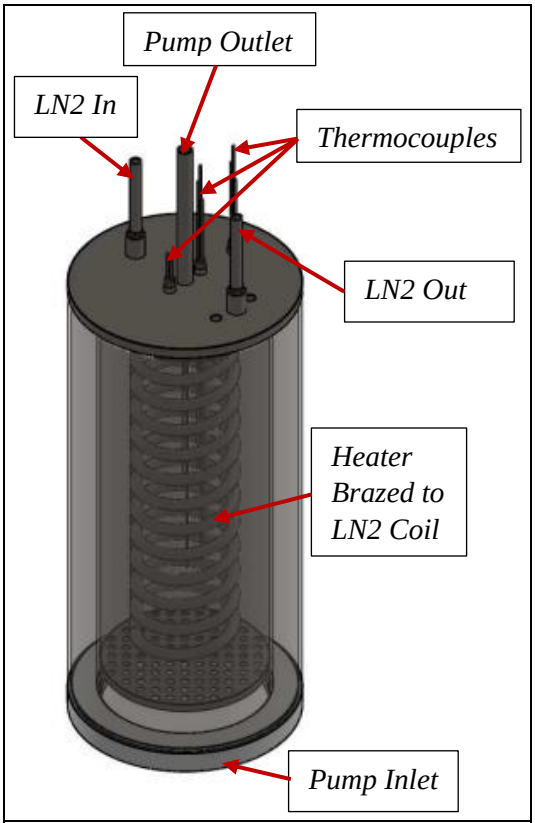

Figure 4a.
This is a 3D rendering of the cryosorption pump design. The pump is transparent to show the inlet, outlet, LN2 and heating coils, as well as the 3 thermocouple bundles.

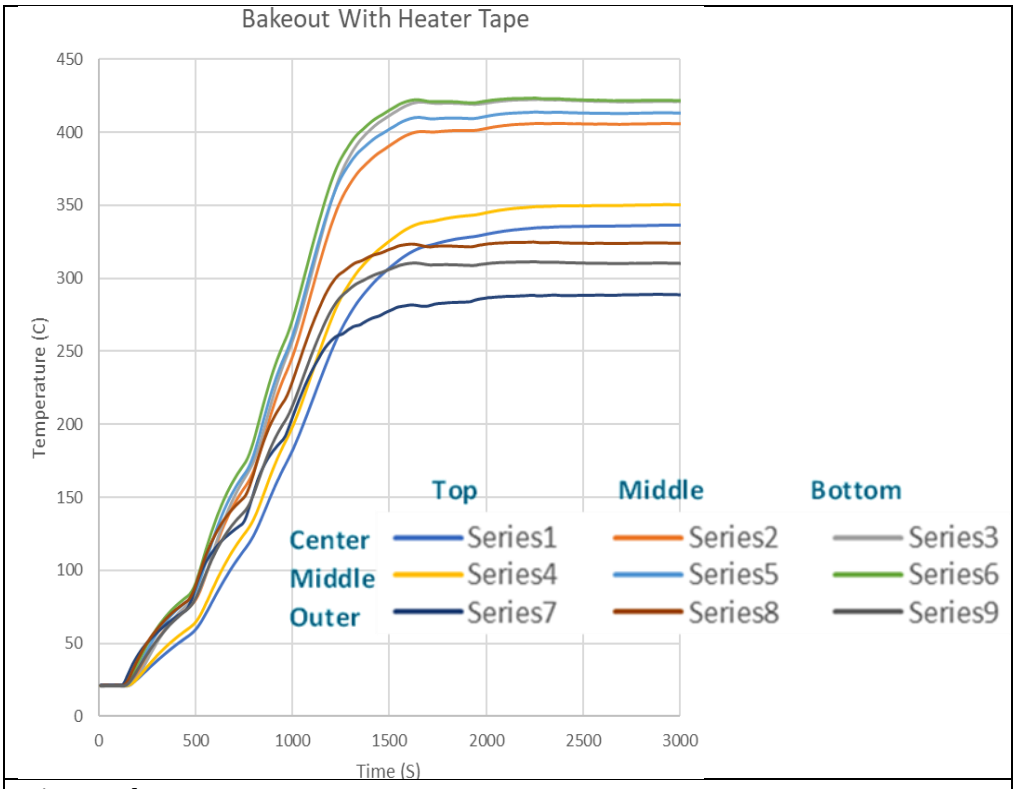

Figure 4b.
Example bakeout run showing thermocouple temperature in Celsius over time at nine different locations. Temperatures reach steady state in around 30 minutes, but there are large temperature variations throughout the volume of the pump.

During bakeout, temperatures (*see figure 4b*) increased from room temperature to steady-state temperature in around 1750 seconds. There was, however, a large difference in temperature (150 °C) measured by thermocouples in different locations of the pump. A minimum of 275 °C was measured at the top-outer thermocouple, while a maximum of 425 °C was measured at the inner and middle-bottom thermocouples. Based on the thermocouple readings, the top and outer parts of the molecular sieve bed are being heated less than the rest, indicating potential insulation issues through the jacket of the pump as well as the sheaths of the thermocouples. If the pump had been recently exposed

to atmosphere, it was left at this steady state temperature until the dewpoint sensor read that the pump effluent was dry.

After bakeout, the contents of the cryopump must be cooled to cryogenic temperatures by first bringing the temperature down to 50 °C with gaseous nitrogen, then cooling down the rest of the way with liquid nitrogen. It was demonstrated that the thermal conductivity of the molecular sieve is poor, but that adding helium gas during liquid nitrogen cooling is effective in bringing temperature down further and more uniformly.

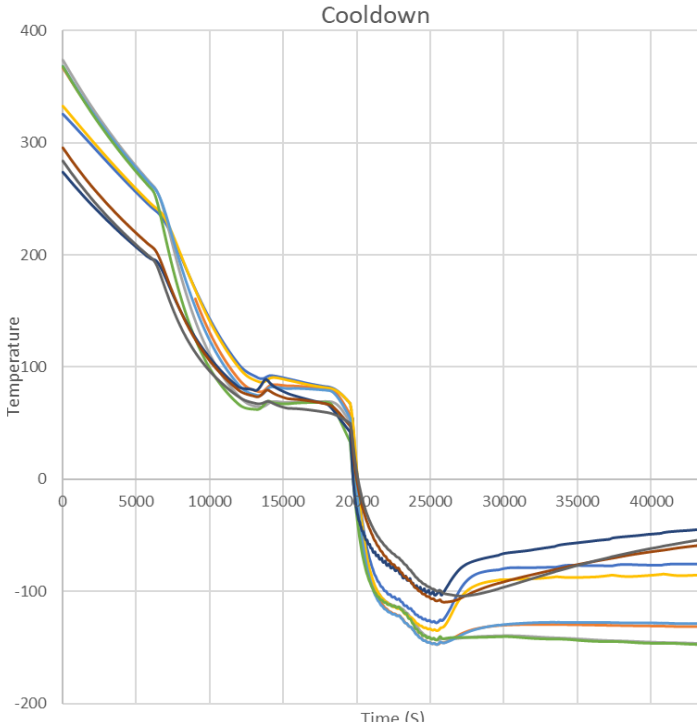

Figure 5a.
Thermocouple temperatures (°C) in the cryopump over time. This is a preliminary cooling in two stages: first gaseous, then liquid nitrogen after 20,000 s. At the end of this run there are large temperature differentials within the pump (color codes as in figure 4b).

The bulk of the cooling is handled by gaseous nitrogen, which is fed through the pump with a mass flow controller. This effectively removes heat, bringing internal temperatures to the 70 to 90 °C range. At this point, nitrogen was evacuated from the pump and liquid nitrogen was fed through internal coils to bring the temperature down even further to range from -100 to -150 °C. An insulation problem became apparent after this minimum

temperature was reached (*see figure 5a)* as the temperatures diverged over time to a 100 °C temperature difference from the warmest to the coolest thermocouple. The system was left running for several hours with automated liquid nitrogen filling and the temperatures reached a steady state, but the large temperature differences were retained. Similarly to the heating run in figure 4b, the farthest from the target temperature, and the most affected by insulation issues, are the top and outer thermocouples.

When helium was pumped into the volume of the cryopump, there was a significant cooling effect (*as seen in figure 5b*): while the minimum temperature stayed close to -170 °C, the warmest dropped significantly from -30 to -140 °C, bringing the overall temperature difference down to 20 - 30 °C. It was evident that the thermal conductivity of the molecular sieve in vacuum conditions was not enough for the liquid nitrogen coil to uniformly cool the volume of the pump. The temperature difference was brought closer to an acceptable level because the helium gas was convectively cooled and was able to reach the places in the pump that were experiencing conduction to the outside. When the helium was pumped out in preparation for hydrogen dosing, there was a sharp increase in temperatures. This warming can be attributed to conduction along the sheaths

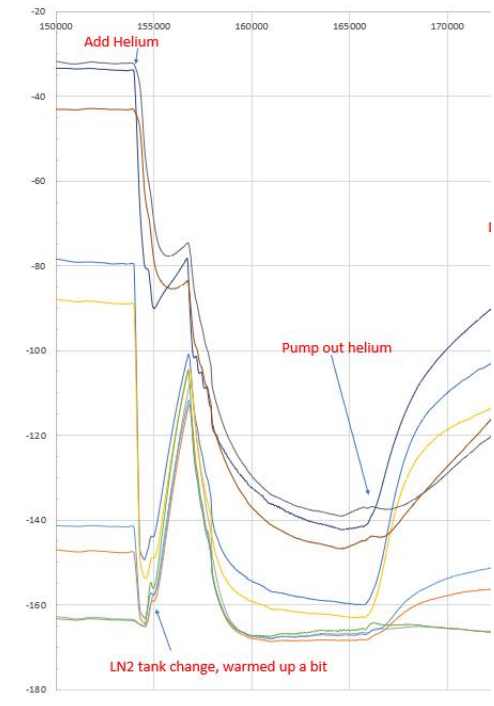

Figure 5b.
Continuation of run in fig. 5a with an expanded temperature scale. This demonstrates the effect of adding helium during cooling to cool further and increase temperature uniformity.

of the shorter, top-level thermocouples, which saw the sharpest rise in temperature (*see figure 5b).* In future designs, the thermocouples will be chosen to eliminate conduction along the metal sheath and improve the accuracy of temperature measurements.

V. Hydrogen Dosing

In a new run, hydrogen was introduced and regulated by a mass flow controller. Three dosing schemes were tested: Hydrogen was flowed at 0.5 sLpm without helium precooling and yielded a capacity of 0.25 sL of hydrogen. At the same flow rate, the addition of helium precooling increased the capacity to 4.6 sL. The third dose was done at 5 sLpm with precooling and yielded 2.3 sL hydrogen capacity. During hydrogen dosing, the temperature was measured with the aforementioned thermocouples and the upstream pressure was measured with a 10 torr transducer.

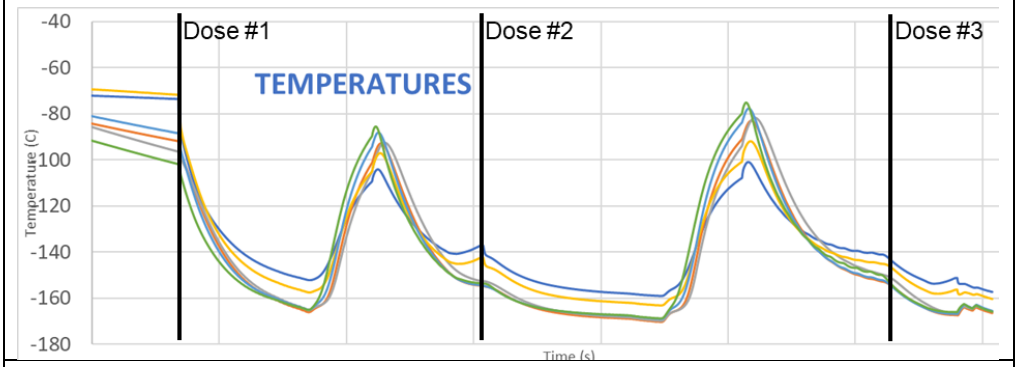

Figure 6a.
Temperature readings during hydrogen dosing run (each time interval corresponds to 2000 seconds). Each bold vertical line represents the start of a dose. Temperatures decrease as hydrogen is added, then spike when the hydrogen is baked off. Doses 2 and 3 use helium to bring the temperature down after the spike rather than immediately flowing hydrogen. Color codes as in figure 4b.

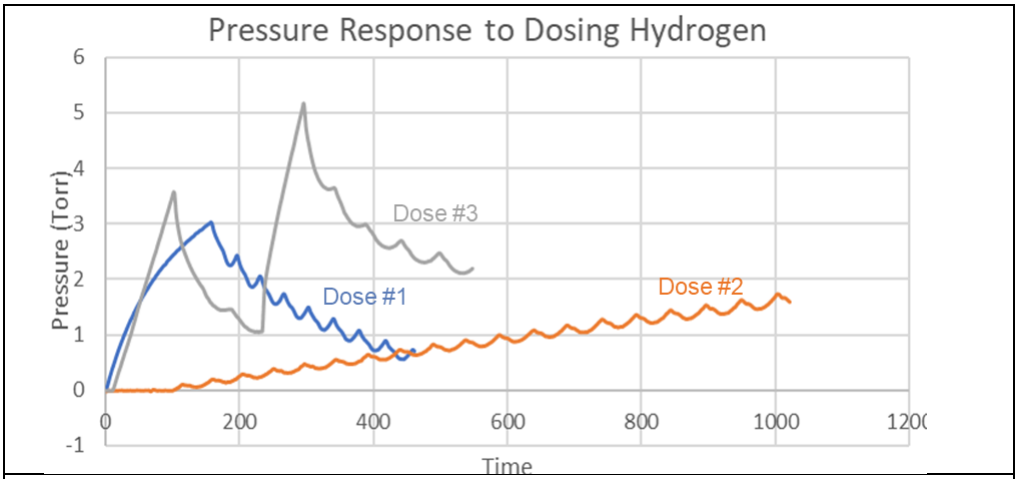

Figure 6b.
Overlay of pressure over time (s) during three dosing schemes, each starting when hydrogen began flowing into the pump. Capacity was calculated based on the amount of hydrogen that flowed before the pressure reached 1 torr.

The first of 3 doses began when the pump was still "partially" cooled, meaning that there were large temperature variations throughout the pump. When hydrogen was added at the start of Dose #1, it brought the temperature down with the same convective effect that helium had (*see figure 5b)*. The beginning of the run occurred at higher temperatures, however, which resulted in a quick increase in pressure (*see figure 6b Dose #1)*, surpassing the 1 torr threshold in 30 seconds. Based on this reading, the hydrogen capacity was calculated with the following equation:

$$C = F * t$$

where C is hydrogen capacity in sL, F is hydrogen flow rate in sLpm, and t is time to threshold in minutes. With 0.5 sLpm for 0.5 m, the capacity was measured to be 0.25 sL for Dose #1. Directly following subsequent doses, hydrogen was "regenerated" from the molecular sieve. The bed was heated to around -100 °C and helium was flowed to purge the hydrogen that was cryosorbed to the molecular sieve.

Precooling the sieve bed (done for Doses #2 and #3) involved allowing 5 torr of helium into the pump volume while cooling with liquid nitrogen. This brought the temperatures down back to their previous levels before the second addition of hydrogen (*figure 6a).* The effect of bringing the temperature down before flowing hydrogen was demonstrated in Dose #2. The pressure upstream of the pump rose significantly slower compared to the first dose, thus allowing for a much longer time to threshold and a greater capacity (*see figure 6b Dose #2)* of 4.6 sL (0.5 sLpm for 9.2 m) compared to 0.25 sL without precooling.

The third dose demonstrated the effect of increasing the flow rate of hydrogen to 5 sLpm. This proved to negatively affect the capacity as the pressure sharply rose to the 1 torr threshold in 27.6 seconds (*see figure 6b)*. The capacity measured in this run was 2.3 sL. This was greater than that of the non-precooled run but half that of the precooled run with 0.5 sLpm flow rate.

VI. Conclusion

SPARC requires a pumping system to evacuate exhaust gas from the device's volume. High powered turbomolecular pumps used for this purpose need to be backed by secondary pumps at the effluent side. Cryosorption pumps are a good candidate to back the turbo pumps for several reasons. They can pump at high speeds up to ultra-high vacuum, they do not introduce contaminants, and they can selectively retain hydrogen species on cryogenically cooled molecular sieve. We sought to test the hydrogen capacity and thermal properties of a novel cryopump designed specifically for SPARC.

Molecular sieve 4A is not a very effective conductor of heat and a large volume of it is packed into the cryosorption pump. Thus, it proved very difficult to maintain uniform temperature within the pump, although conduction through the sheaths of the thermocouples caused readings to be higher than what they are supposed to be. The efficacy of an adsorbent material depends greatly on the temperature, [6] so the large temperature differentials inside the pump had a potentially detrimental effect on the performance of the pump.

During hydrogen dosing, it was measured that precooling the sieve with 5 torr of helium increased capacity by a factor of 17.2 (from 0.25 to 4.6 sL) at a hydrogen flow rate of 0.5 sLpm. Increasing the flow rate to 5 sLpm decreased the capacity to 2.3 sL, so 0.5 sLpm was the preferred flow rate of those tested. Despite lack of thermal insulation to the outside of the pump and the lack of thermal conductivity inside the pump, the addition of helium proved to significantly increase internal conductivity and, thus, hydrogen capacity.

The next steps for this cryosorption pump should be centered around the thermal issues that were encountered. A better (or double) vacuum jacket around the pump should eliminate the need for other insulation materials and significantly reduce conduction from the atmosphere. Better insulated thermocouples are a necessity to ensure accurate temperature measurements. New cooling designs should be explored including liquid nitrogen-cooled baffles, or the addition of conductive material interspersed with the molecular sieve.

Eventually, once thermal issues are resolved, the ability to reliably contain tritium is very important and will be necessary for implementation in a commercial fusion reactor.

VII. Acknowledgements

I would like to thank Dr. Stephen Craxton for his unwavering support during as well as after the conclusion of the program. Also, many thanks to Dr. Walter Shmayda and Dr. Eric Dombrowski for giving me valuable hands-on experience in research and teaching me so much throughout the summer. Finally, my fellow students were instrumental in motivating me and I was very impressed by the work they presented at the end of the program.

VIII. References

1. A. J. Creely, M. J. Greenwald, S. B. Ballinger, et al. Overview of the SPARC tokamak. *Journal of Plasma Physics*. 2020;86(5):865860502. doi:10.1017/S0022377820001257
2. "External Heating." *ITER*, www.iter.org/sci/PlasmaHeating.
3. "Nuclear Fusion Power." *World Nuclear Association* , world-nuclear.org/information-library/current-and-future-generation/nuclear-fusion-power.aspx#:~:text=With%20current%20technology%2C%20the%20reaction,4%20MeV%20for%20D%2DD%20fusion).
4. H. K. Mutha. "Tritium Fueling, Processing and Handling." Jun. 2021. PowerPoint Slides.
5. P. J. Gareis and G. F. Hagenbach, *Industrial & Engineering, Chemistry* **1965** *57* (5), 27-32, DOI: 10.1021/ie50665a006
6. J. E. A. John and W. F. Hardgrove. "Cryosorption A Method for Simulating the Space Vacuum Environment." *Space Simulation Testing Conference*, 1964, https://doi.org/10.2514/6.1964-1401.

Design, Fabrication, and Testing of a 3D-Printed Optomechanical Assembly for MIFEDS Coil Characterization

Micah C. Kim

Homeschool

Rochester, New York

Advisor: Dr. Douglas Jacobs-Perkins

Laboratory for Laser Energetics

University of Rochester

Rochester, New York

November 2022

1. Abstract

Engineering design principles were developed to provide an inexpensive and rapid production method for optomechanical assemblies using 3D-printing technology. The ultimate goal is to establish principles through the development of an optomechanical housing. Several iterations led to optic holders that maintain the axial and radial location of individual optics. Future research will integrate these holders into a monolithic structure.

2. Introduction

The Magneto Inertial Fusion Electrical Discharge System (MIFEDS)[1] produces high-intensity magnetic fields for plasma physics and astrophysics experiments at the University of Rochester Laboratory for Laser Energetics (LLE). Figure 1 shows the MIFEDS device with a closeup of its coil. The MIFEDS device stores 400 Joules of electrical energy in capacitors and then rapidly discharges a 20 kV, 50 kA pulse into a ~1 cm diameter coil.

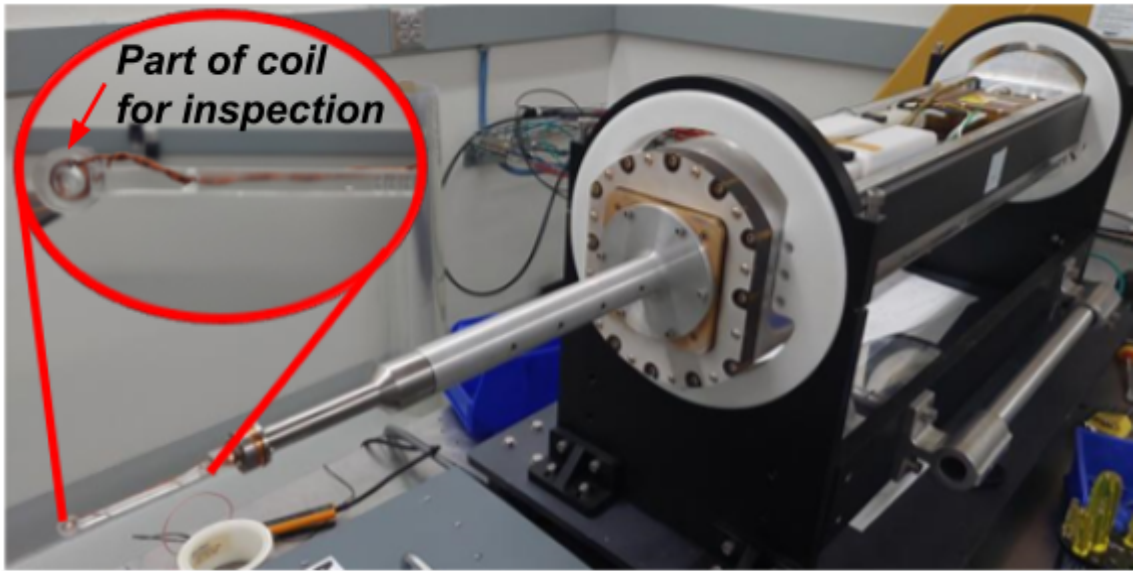

Figure 1 - A MIFEDS diagnostic with close up coil view

MIFEDS coils occasionally fail to meet dimensional specifications, causing interference with laser beams and compromising other aspects of an experiment. These deficiencies need to be identified prior to an experimental campaign to prevent delays and compromised performance. A coil inspection station is being built that will allow for pass-fail dimensional inspection of coils. The inspection station requires two optomechanical assemblies to be built in order to

image a coil assembly from two nearly orthogonal axes. Each assembly houses a telecentric lens assembly, consisting of two lenses and a field stop, one or more mirrors and beam splitters, a camera, and an illumination source. A telecentric lens maintains a constant magnification over an extended depth of field, allowing accurate measurements to be taken from resulting images.

The goal of this work was to develop design principles for the fabrication of high-precision monolithic 3D-printed optomechanical structures and apply them to this system. Monolithic is defined as “consisting of or constituting a single unit” (Merriam Webster 2c) and is a design principle that allows for quick assembly. As these principles are further refined, they will provide an inexpensive and rapid production method for optomechanical assemblies.

3. Optical Layout

Figure 2 shows the telecentric lens system[2] design being packaged. A linear beam path is too long for practical use so a folded design was pursued. The four optical components in the folded setup are lens 1 (50 mm diameter), lens 2, mirror, and beamsplitter (all 25 mm diameter). A field-stop aperture located at the beam-waist is required to achieve telecentric performance. Figure 3 shows the folded arrangement[3], including the camera position. This design is shorter and permits a coaxial illumination source behind the beamsplitter to be injected through it or a ring illuminator in front of the 50mm lens.

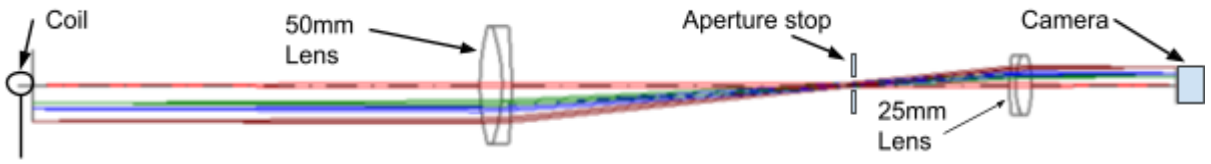

Figure 2 - An optical model created using CODE-V software showing the location of key elements in the telecentric lens assembly

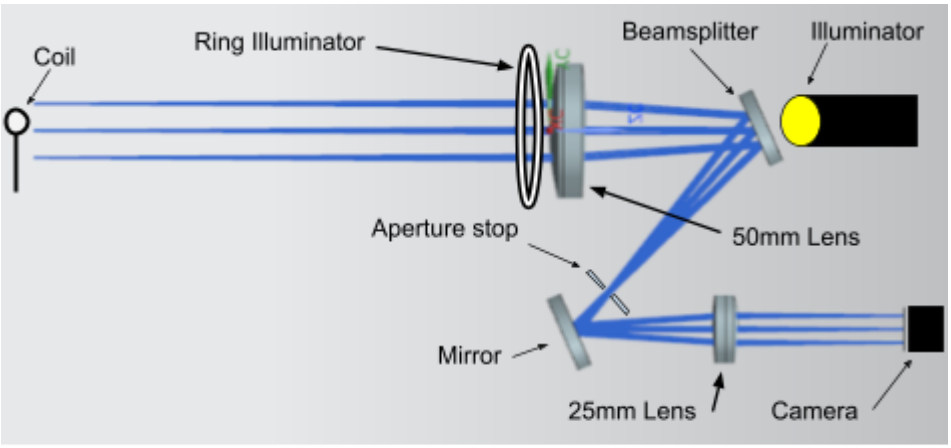

Figure 3 - Preliminary folded layout of optical assembly

4. Stereolithographic 3D-printing And Design Challenges

3D-printing is an additive manufacturing process that forms three-dimensional objects one layer at a time. Stereolithography (SLA) is a photopolymerization printing method. A build plate is lowered into a vat of liquid resin where a laser “writes” a pattern, causing the resin to solidify into a thin layer of hardened plastic. The plate is then raised a small distance (e.g., 0.05 mm) and the process repeats. LLE has Formlabs™ SLA printers which suit this project given their high resolution and accuracy. SLA printing creates the first actual layers of a part after establishing a base “raft” on the build plate. The layers which form the raft sacrifice dimensional accuracy for adhesion. The printer then creates “support structures” which support the part during the printing process. Once the print is complete, the supports are broken or cut from the final part. These supports leave remnants where they were connected to

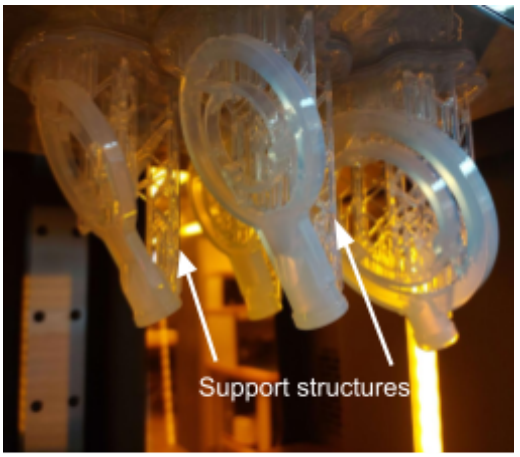

Figure 4 - Supports added by slicer software on a 3D-printed part made with SLA printing

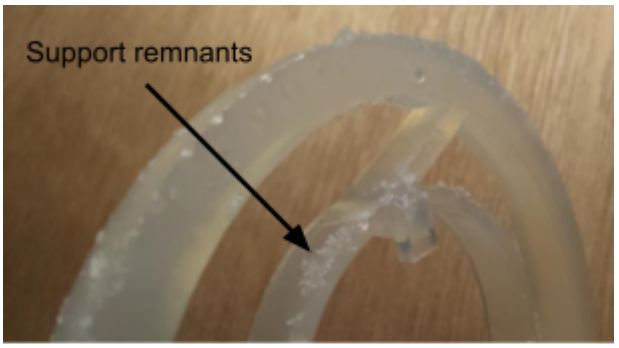

Figure 5 - A close view of support remnants on a printed part

the part. The designer must ensure that these remnants are located where they won't interfere with the functional requirements of the part. Supports are added to a part in a pre-print program known as a "slicer", which slices a model into layers. The slicer used with Formlabs printers is "PreForm"; supports can be added and optimized manually or automatically. Supports are required for any overhanging feature or otherwise unsupported surface. Figure 4 depicts three optic holders with SLA supports that are added to the parts. Figure 5 displays remnants of these supports after removal. These remnants can be smoothed out with the sacrifice of dimensional accuracy.

5. Optic Holder Design Iterations

Figure 6 is a computer-aided design (CAD) model of the first optic holder design. This was inspired by an aluminum optic mount designed by Mark Romanofsky[4]. Three (3) contact points constrain the optic radially; two of these are "fixed" and one flexes to create a radial "clamping" force. In this design, the center line of the supported optic changes for varying diameter components. This is suitable for plano optics (e.g., flat mirrors & windows) as they have large centering tolerance, unlike curved optics (e.g., lenses).

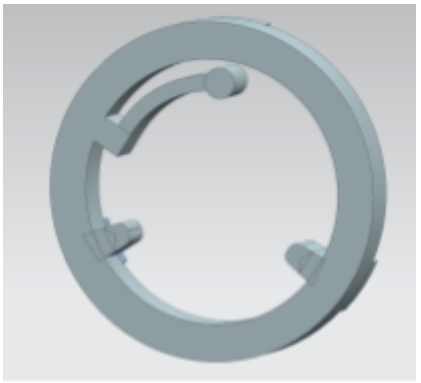

Figure 6 - Design with two stationary contact points and one flexure point

Optical performance depends on precisely aligning the optic axis of all lenses. Figure 7 depicts a design consisting of three "flexure points"; the inner ring deforms symmetrically about its center point upon optic installation. This design maintains the center line regardless of optic tolerance and was used for all components given its versatility. This design was adequate for early development work, facilitating easy installation and removal of optics, but it doesn't constrain the part axially and instead

Figure 7 - Design with three contact points flexing symmetrically with respect to the center of the optic

depends on friction at the three contact points to retain the optic. An option explored later uses 3 screws with plastic washers to properly retain the optic.

Axial stops are needed to locate the critical surface of an optic (e.g., the reflective face of a mirror). These features must accommodate component curvature when applied to lenses while flat mirrors need no such consideration. Figure 8 shows a spring-clip concept that both constrains axial placement and retains the optic.

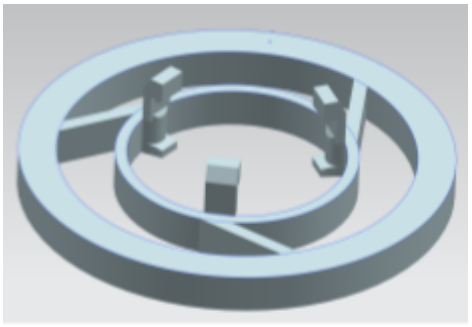

Figure 8 - Design that constrains the optic axially and radially

5.1 Component Holder Variations

Each component requires a unique variation of the holder design. Unlike the lenses, the mirror and beam splitter feature flat surfaces on both sides. Figure 9 is the design of the beam splitter and mirror holder. The beam splitter differs from the mirror as it has a 0.5° wedge to direct reflections from the back of the beam splitter out of the imaging path. This holder iteration uses friction to hold optics in place and has three flat stop points along with extrusions indicating the location of the thickest point on the beam splitter.

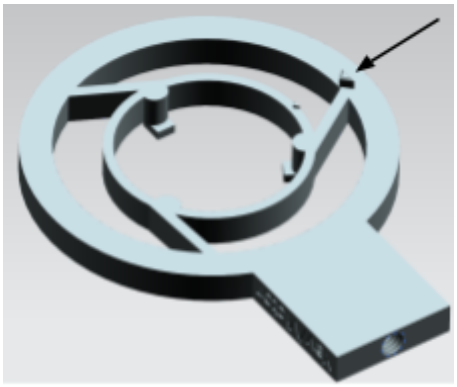

Figure 9 - Beamsplitter and mirror design with arrow to the beamsplitter thickest point indicator

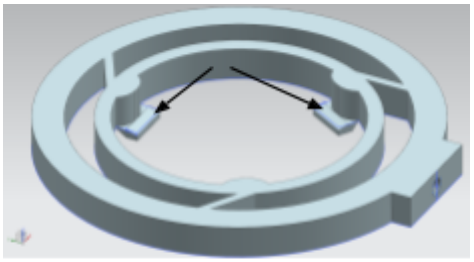

Figure 10a - 50mm optic holder design with arrow to the backstops

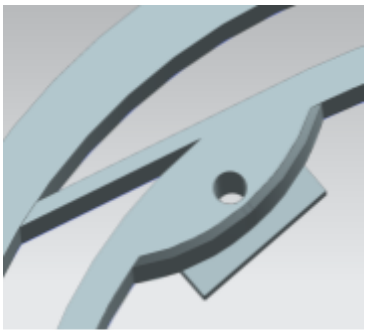

Figure 10b - 50 mm optic holder screw hole

The two lens holders accommodate lens curvature and define the edge position. Figure 10a displays the optic holder for the 50 mm lens. The optic holder for the 25 mm lens follows the same design concept. Figure 10b shows a recent design developed that has a screw hole to facilitate

optic retention using a screw and washer. Figure 10b, because of the simpler design, requires no supports on working surfaces.

The individual component holders need to be mounted to a breadboard for testing. Figure 11 shows a design created to be compatible with a commercial breadboard clamp allowing for breadboard testing. This feature was added to all component holders to locate the optic axis at the correct height.

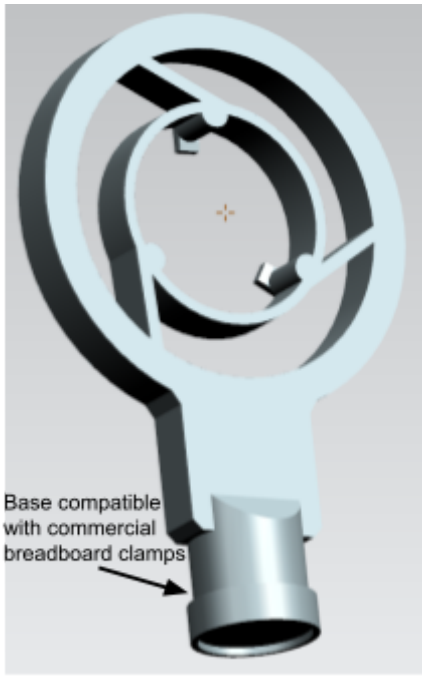

Figure 11 - Commercial breadboard clamp design

6. Preliminary Breadboard Testing

Using the optical layout depicted in Figure 12, a breadboard prototype was constructed following the layout from Figure 3 using either a monochromatic red coaxial illuminator or a white-LED ring illuminator[5] in front of the first lens (a.k.a. front-side illumination). Several problems were encountered in the preliminary tests. The coaxial illuminator scattered light in the translucent resin, causing poor image contrast. Scattering also renders a translucent aperture stop ineffective.

An image taken of a test MIFEDS coil using the ring illuminator (Figure 13) was far superior. After the preliminary testing, it was found that the 50 mm lens was mounted backward, which likely contributed to poor image quality along with the lack of the aperture stop.

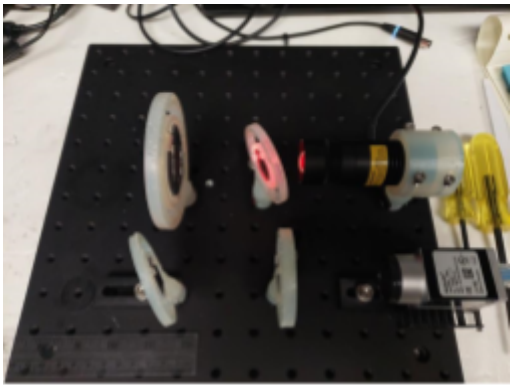

Figure 12 - Breadboard Setup. The components match those shown schematically in Figure 3.

Figure 13 - Image from breadboard setup using ring illuminator

7. Conclusion

Engineering design principles for 3D-printed optical mounts were developed to provide an inexpensive and rapid production method for optomechanical assemblies. Optic holders were successfully produced which met all desired criteria.

8. Future Research

Illumination issues will be resolved through the testing of front-side and coaxial illumination separately and in tandem. Due to light scattering in translucent 3D-printing material, opaque alternatives, and their qualities will be tested. Optimization is required on the optic holder design to minimize size by reducing the flexure arm length as well as the thickness of all features. A method for retaining each optic in its mount must be chosen. The option currently being pursued uses three thread-forming screws positioned near the three points of contact to press plastic washers against the optics. The feasibility of using low-cost, rapid-production 3D-printing for optomechanical systems will thus be demonstrated by the integration of all optic holders into a monolithic assembly. Mounting features need to be designed to install the two optical assemblies into the characterization station. A rail mount system is being considered.

9. Acknowledgments

I thank Dr. Craxton for organizing this program, which provides such amazing opportunities for my fellow students, and my advisor, Dr. Doug Jacob-Perkins, for all the time dedicated to my project this summer. Additionally, I thank Mike Bradley for teaching me SLA 3D-printing and techniques as well as Dave Weiner and Sam O'Conner for sharing their knowledge and expertise on optics. Also, many thanks to the other students in the program for their help and their hard working attitudes.

10. References

1. J. L. Peebles, G. Fiksel, M. R. Edwards, J. von der Linden, L. Willingale, D. Mastrosimone, Hui Chen; Magnetically collimated relativistic charge-neutral electron–positron beams from high-power lasers. Physics of Plasmas 1 July 2021; 28 (7): 074501. https://doi.org/10.1063/5.0053557
2. Weiner, David. LLE Optical Engineer
3. O'connor, Sam. LLE Optical Engineering Intern Summer 2022
4. Romanofsky, Mark. LLE Mechanical Engineering Assembly Group Leader
5. Example Ring Illuminator Product Link: https://www.advancedillumination.com/products/rl208-series/

Viability Testing of Polymer Coating for Optical Cleaning Applications

Jackson McCarten

Webster Schroeder High School

Advisors: Brittany Hoffman, Kyle Kafka

Laboratory for Laser Energetics

University of Rochester

December 2023

1. Abstract

The performance of optics used in high-power laser systems can be limited by surface contamination in the form of particles and films. Viability testing was performed for a commercial polymer (First Contact™) as a strip-coat cleaning process for glass substrates, multilayer dielectric (MLD) coatings, and MLD diffraction gratings. The polymer can be brushed or sprayed onto the desired optic surface; it is then mechanically removed. Contact angle measurements, particle counts, force measurements, and damage testing were all used to determine the polymer's viability as a cleaning process. A process was developed that successfully removed contamination particles from flat optics, and prevented the polymer from leaving behind a thin film of contamination. For structured films such as MLD gratings, preliminary results suggest that a different application process needs to be developed.

2. Introduction

Multi-layer dielectric (MLD) gratings are used in pulse compression and stretching, key aspects of chirped pulse amplification [1]. This process creates high-intensity ultrashort optical pulses. This technique is currently used with the OMEGA EP laser system at the Laboratory for Laser Energetics. Particle contamination on the surface of optical components has been shown to significantly decrease the laser-induced-damage threshold (LIDT), increasing the likelihood of the optics being damaged [2]. Due to diffraction gratings' fragile structure consisting of rows of pillars, cleaning is difficult without damaging their structure; therefore they are often cleaned entirely using chemical processes. The company Photonic Cleaning Technologies [3] offers a commercial mixture of polymers and solvents, First Contact™, designed for strip coat cleaning of optics, including diffraction gratings. When the mixture is applied to the surface, it engulfs contamination, such that the contamination can be removed along with the polymer after drying. Ideally, this process leaves behind no residue, and the removal is mechanically gentle enough to preserve the quality of the optical surface. Practically, any incomplete drying or incomplete removal of

the polymer could potentially introduce its own film of contamination onto the optics, and localized stresses caused during the polymer removal could damage the structure of the diffraction gratings.

An optimized cleaning process that addresses the above concerns could potentially increase the operational lifetime of diffraction gratings. In this work, we take steps toward development of such a process. Using various methods such as contact angle measurements, particle counts, force measurements and damage testing, we demonstrate a process that successfully removes particle contamination from optics, prevents the polymer from leaving behind a thin film of contamination, and subsequently provides a preliminary attempt at cleaning the fragile structure of MLD gratings.

3. Instruments and Evaluation Techniques

Particle density measurements were used to evaluate the efficacy of the polymer for cleaning the surface of the samples. The particle density of a sample is determined through optical microscope imaging. The entire surface of a sample was imaged in a grid pattern; commercial software was then used to count the number of particles (>1.8 μm in diameter) in each image to determine the particle density for each sample. Cleaning effectiveness was evaluated by comparing the particle density before and after a process. The particle density from each image could be plotted to provide a particle density map of a sample, which was a useful tool in evaluating the cleaning effectiveness across a sample.

Contact angle measurements were used to evaluate the cleanliness of a sample and the degree to which the polymer coating was removed from the sample. The contact angle is defined as the angle that a liquid makes with a surface when wetted. See Figure 2(a) below for examples of the measurement. The contact angle is measured by dropping a small fixed amount of water onto the sample and using a camera and computer analysis to measure the angle. Film contamination can be detected by comparing the contact angle from before and after the polymer is used to clean an optic. For this study, clean glass

is very hydrophilic with low contact angles, whereas glass coated with an organic film tends to be more hydrophobic and has higher contact angles.

It was found that the water droplets from the contact angle measurement could contribute to the particle load on the sample, thus possibly altering the particle density results of subsequent cleaning experiments. Three different water droplet drying techniques were tested and the particle density was compared before and after the water application and drying as shown in Figure 1. Figure 1(b) shows that the prompt removal of the water droplets with a nitrogen gun was highly effective in removing the particles contributed by the water and resulted in a small reduction of the particle density (number of particles per unit area on a surface): values on the order of -10 counts/mm^2 are seen in Figure 1(b). In contrast, the other methods resulted in large increases in the particle density. The nitrogen gun method for drying was therefore used in the subsequent experiments.

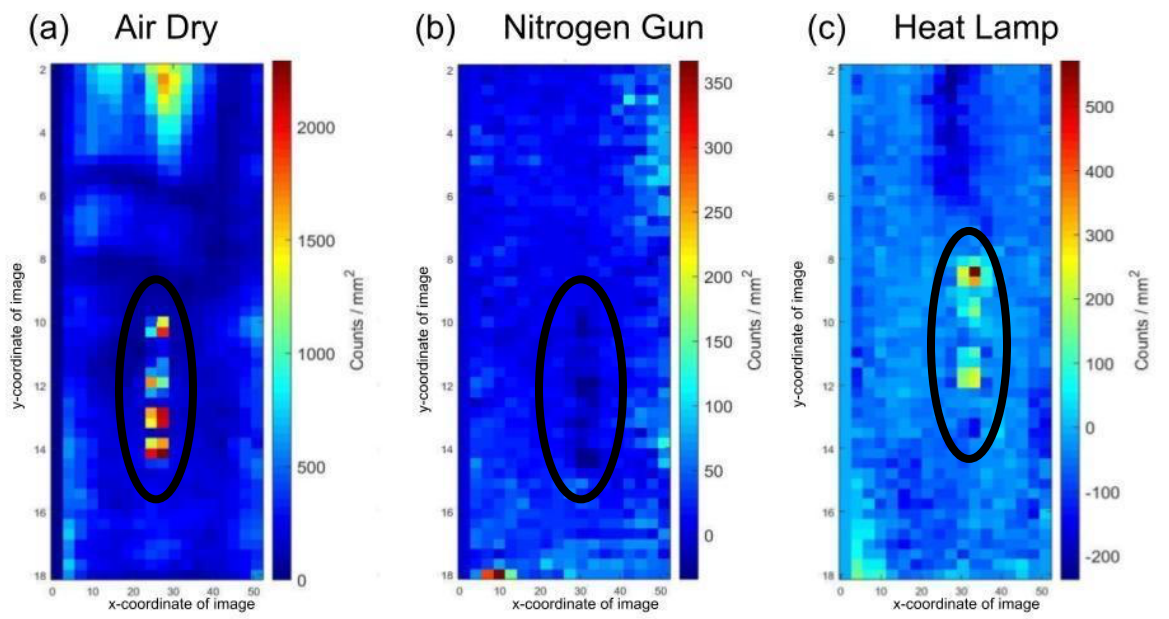

Figure 1: Maps of particle density changes on glass slides for three different methods of removing contact-angle water droplets: (a) allowed to air dry at room temperature, (b) blown off with a nitrogen gun, or (c) air dried with a heat lamp. The black ovals indicate the regions where the water droplets were applied. The X and Y axes correspond to coordinates on the glass slide. The color indicates the difference in particle count per mm^2, counts after minus counts before the contact angle measurement.

Laser damage testing of the MLD mirrors was performed using a laser system operating at 1053 nm and having a tunable pulse duration between 0.6 ps and 100 ps. This system has been described in detail elsewhere [4]. By comparing results before and after polymer use, the laser damage testing characterizes the polymer's impact on optical performance. If the polymer mixture is not fully removed in the processing of a nominally pristine sample, the damage threshold would be anticipated to decrease.

4. Developing an application and removal process

During initial testing of the polymer, the manufacturer's recommended procedures were used. However, measurements performed on the treated samples showed an increase of water contact angle after polymer treatment, suggesting a thin film of residual material from the polymer solution. Given the

sensitivity of the intended application (high-powered lasers) to surface contamination on the optics, experiments were performed to attempt to eliminate this contamination by modifying the process parameters.

In order to effectively develop and implement a cleaning process with the polymer solution, glass microscope slides were used as test subjects. These slides, which possess a less uniform surface and a higher degree of contamination than clean MLD optics, were used to develop a procedure for applying, drying, and removing the polymer.

The general procedure starts with application of the polymer coating onto the samples via brushing or spraying. When brushed onto the optics, the optic was laid flat, polymer was poured onto the optic, and the surface tension between the polymer on the optic and the brush was used to spread the polymer. When sprayed onto the optics, the optic was held vertically, and the polymer was sprayed in multiple light coats to prevent the polymer from dripping. The coating was applied to a chosen thickness, such as, for example, to the appearance of the pink color of the manufacturer's visual aid that corresponded to approximately 5-10 spray coats. Tape was applied around the outer edges of the optic when spraying, to prevent the polymer from getting onto the side edges of the samples, because this caused an increase in the difficulty in fully removing the polymer from the optical surface. In order to later remove the polymer, a mesh or floss peel tab was embedded into the wet polymer coating. Then the sample was allowed to dry for a period of time, after which the mesh or floss tab was used to peel the polymer from the optic.

The initial experiments, which used the manufacturer-recommended instructions, showed that the contact angle increased after the polymer treatment (brush and spray section of Figure 2). Before removal, the polymer coating has a contact angle of approximately 90 degrees, much greater than the baseline contact angle of the glass substrates. Therefore, an increase in contact angle indicates that a film

of contamination is left behind by the polymer because the surface of the optic is more similar to the polymer than it was before. We hypothesized that this was caused by incomplete curing of the polymer. This was tested by applying a spray coating, then allowing the polymer to cure overnight (approximately 24 hours) instead of 1 hour, and alternatively by applying heat with a heat lamp as the polymer cured. However, no significant changes were found with these alternate curing methods (overnight and heat lamp section of Figure 2). Furthermore, there was a significant decrease in particle density after the polymer was used to clean the glass substrates for all cases (Figure 3). This indicates that the polymer was reducing the particle contamination load for the samples, and that the longer or hotter curing provided no advantages. Therefore, subsequent experiments maintained the 1 hour drying time at room temperature.

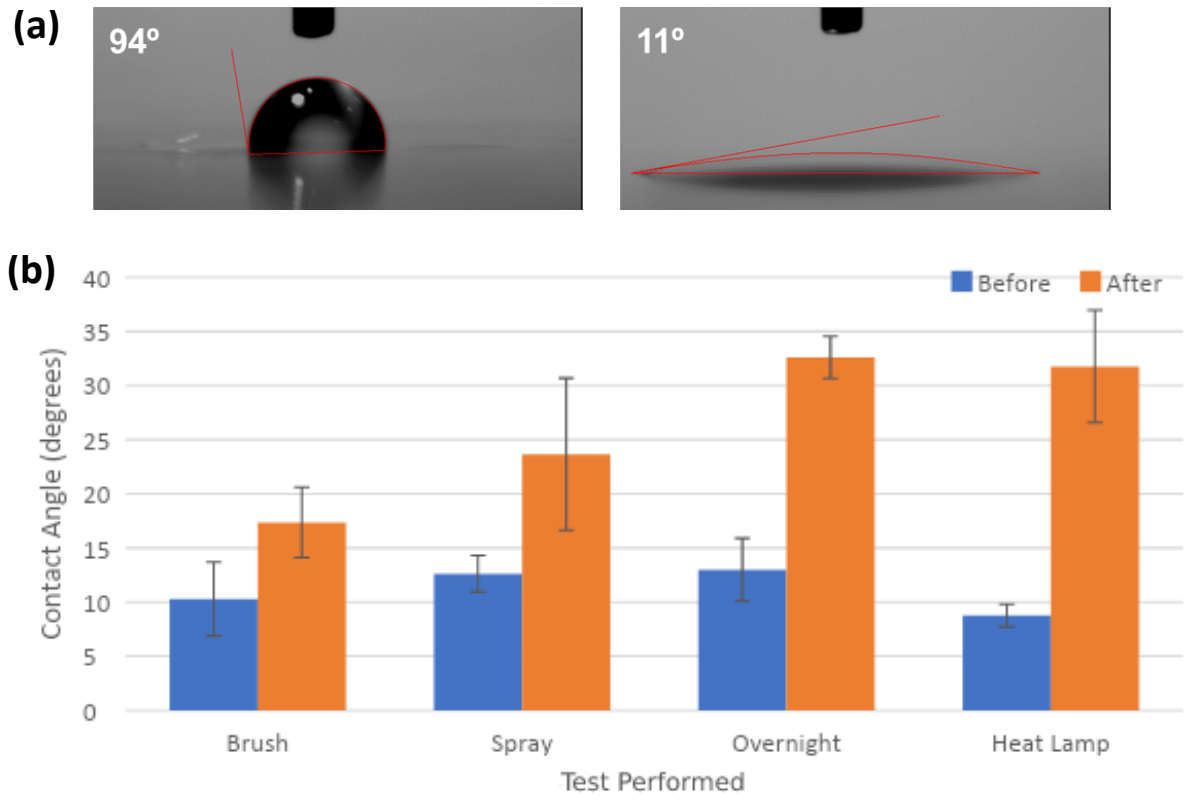

Figure 2: (a) Images from contact angle measurements of the polymer coating (left) and a glass slide (right). (b) Contact angle measurements for different polymer application and drying techniques. The

Overnight and Heat Lamp drying methods were performed with spray-applied polymer coatings. The blue bars are the measurements before application and the orange bars are the measurements after removal.

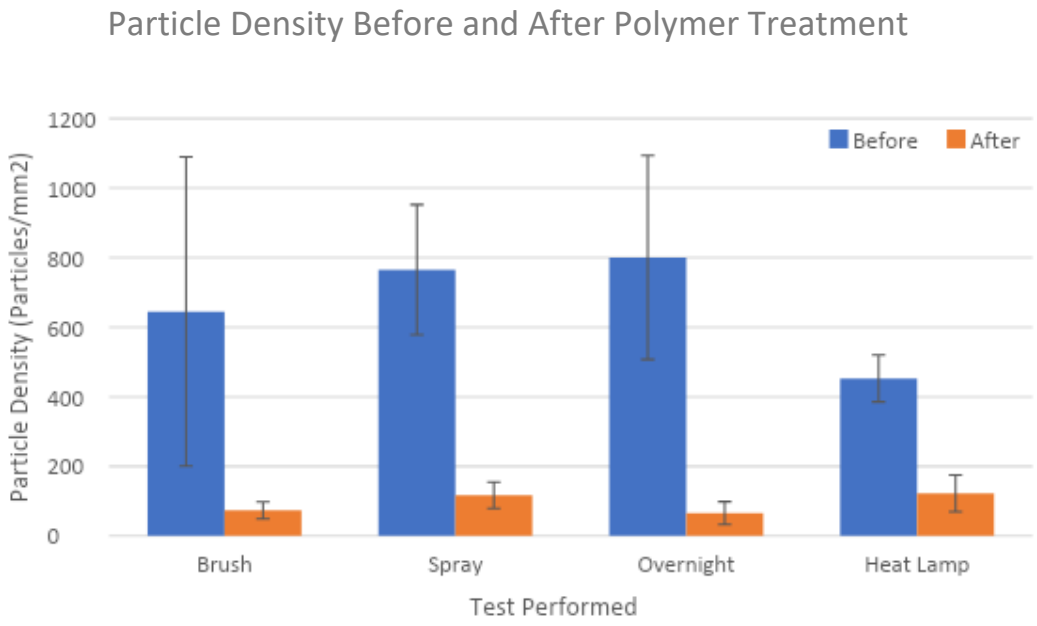

Figure 3: Cleaning efficacy for various application and drying techniques, reporting measured particle density in particles/mm^2 before (blue) and after (orange) the polymer treatment was used to clean the optics. The Overnight and Heat Lamp drying methods were performed with spray-applied polymer coatings.

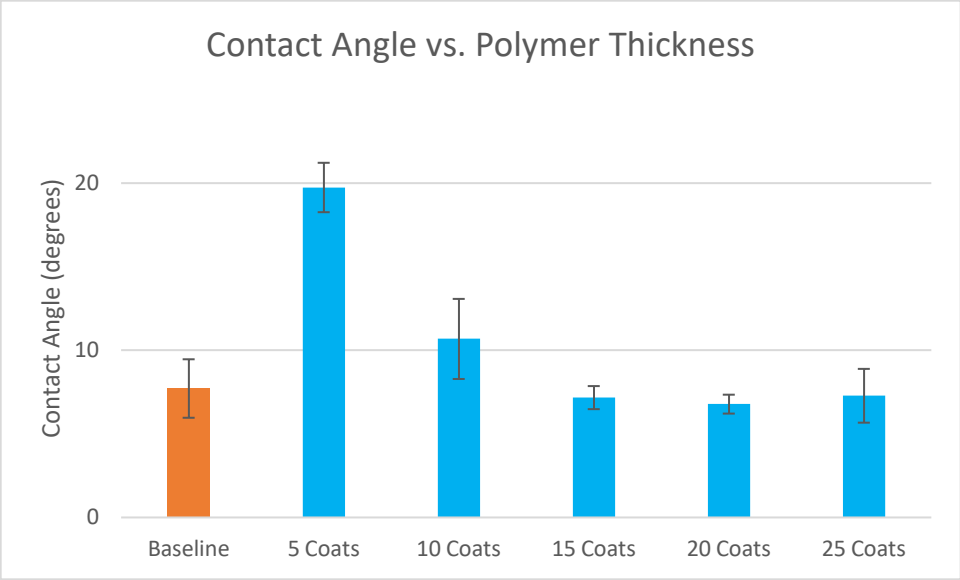

Figure 4: Measured contact angle in degrees after polymer treatment as a function of spray-coat thickness. Baseline shows the average contact angle of all glass substrates before treatment.

Since contact angle measurements indicated that alternate polymer curing methods still resulted in incomplete removal, it was alternatively hypothesized that the thickness of the polymer affected its ability to peel without leaving a film of contamination. This was tested by coating glass substrates with 5, 10, 15, 20, and 25 coats of the spray polymer. One coat was 2-3 pumps from the vendor-provided bottle sprayed at a distance of approximately 12 inches away. The polymer was given 1 hour to dry. As shown in Figure 4, it was found that as the thickness of the polymer increased, the contact angle decreased until around 15 coats when it was the same as or lower than the baseline. With the increased polymer thickness, the polymer was able to remove particle contamination without leaving a film of contamination.

In summary, the final application process resulting from this work with glass slides used 20 spray-coats of polymer, each coat being 2-3 pumps from approximately 12 inches away using the vendor-provided bottle, with at least 1 minute between each coat. The peel tab was embedded in the final 2

coats. The polymer was then given 1 hour to cure at room temperature in horizontal orientation. The polymer was removed using a mesh peel tab in an apparatus using a force gauge and motorized stage.

5. MLD Mirrors and Gratings

Once a process for using the polymer was established, the process was tested on few-square-inch optical component samples that are representative of the optics used in the OMEGA EP laser system, such as MLD mirrors and gratings. The objective was to demonstrate that the developed process effectively cleans particles on actual optics, without leaving its own film of contamination. The MLD mirrors are manufactured by coating multiple layers of dielectric materials (typically silica and hafnia in high-LIDT applications) onto glass substrates. The MLD gratings are MLD mirrors with a thick top layer (typically silica) that has sub-micron lines or grooves etched into it. The MLD mirrors were tested before gratings due to the simpler surface geometry.

5.1 MLD Mirrors

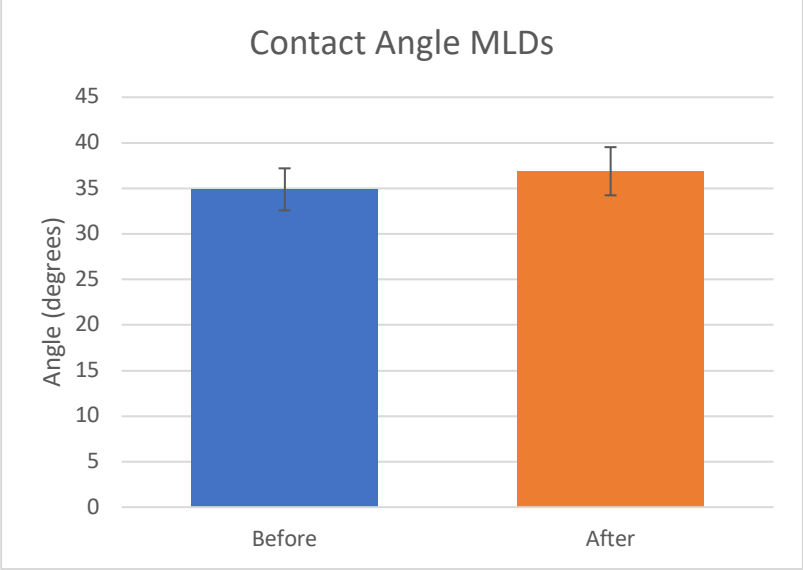

Figure 5: Contact angle before (blue) and after (orange) the polymer was used to clean the MLD mirrors.

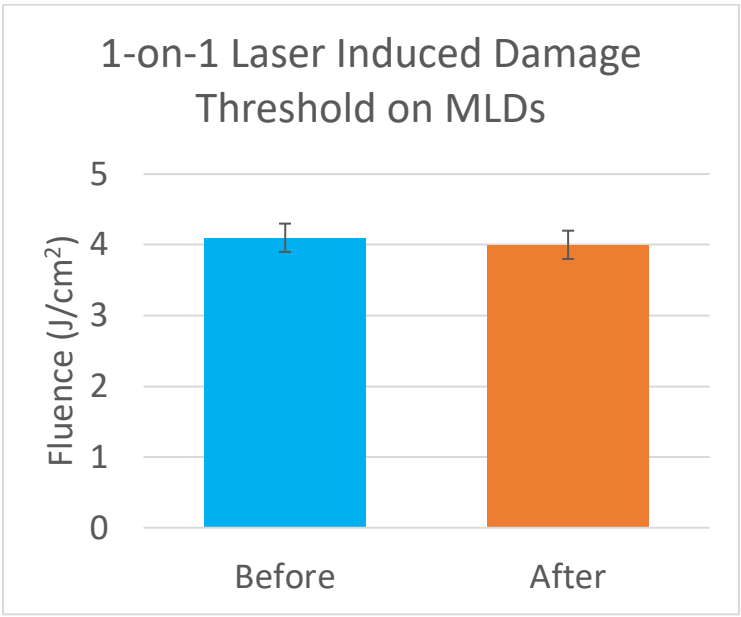

Figure 6: Fluence that the optics could withstand before sustaining damage. This was measured before and after the polymer was used to clean the optics. These measurements were taken in a vacuum with a 42-degree angle of incidence, 10 ps pulse duration, S-polarization, and a wavelength of 1053 nm. These parameters are based on the MLD mirrors' design and conditions the mirror would be exposed to in OMEGA EP.

The results of contact angle measurements, laser-induced damage testing, and particle counting suggest that the process developed with glass microscope slides applies well to MLD mirrors (with no surface structure). Contact angle measurements show no change before and after the polymer was used to clean the optics (Figure 5). Additionally, the laser-induced damage threshold was measured before and after the polymer was used to clean the optics. The LIDT corresponds to the laser pulse energy per unit area that the optics can withstand before sustaining damage. Since there was insignificant change in the LIDT before and after the polymer treatment (Figure 6), this provides an independent and practically relevant result indicating that the polymer left no relevant film of contamination on the optics.

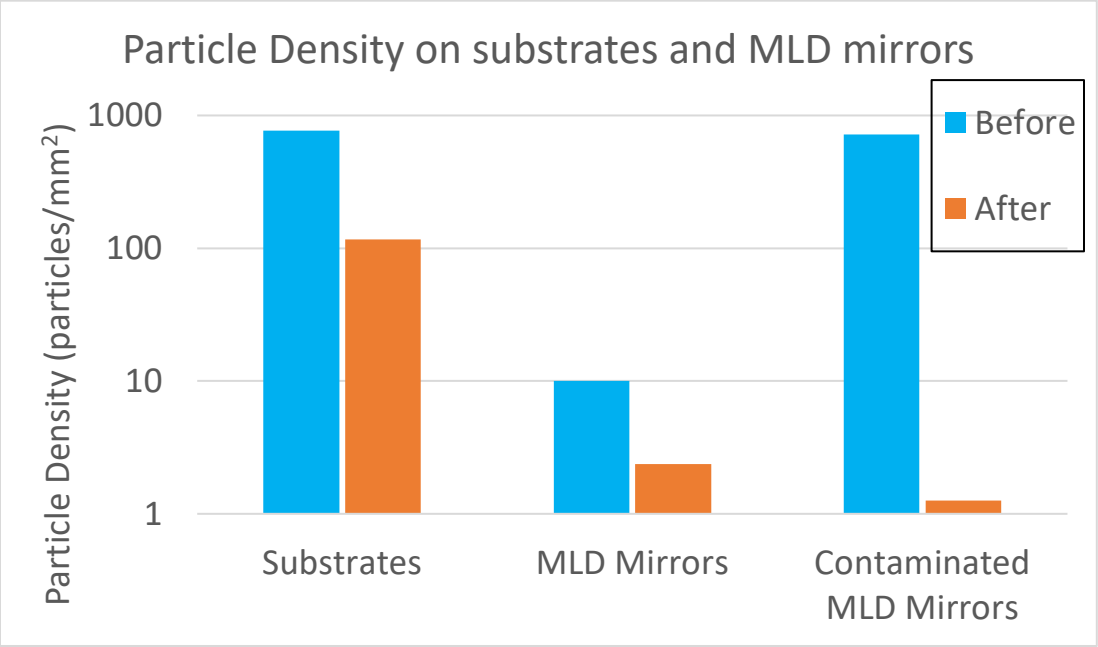

Figure 7: Measured particle density in particles/mm^2 before and after the polymer was used to clean glass substrates, MLD mirrors, and contaminated MLD mirrors.

Particle density was measured on clean glass substrates and on clean and intentionally contaminated MLD mirrors. The "contaminated" MLD mirrors had 325-mesh stainless steel particles gently poured onto the glass while held horizontally; the glass was then tilted vertically and shaken gently until the particles were not visible to the naked eye. In all cases the particle density decreased significantly, indicating that the polymer was cleaning the optics of particle contamination (Figure 7). It is worth noting that some small fraction of the "particles" identified by the microscope image analysis may not actually be particles at all, but may correspond to other defects such as scratches or digs. This implies that the actual cleaning efficacy may be higher, since the after-treatment value of particle density may include such non-particle defects. Furthermore, the extremely low particle density of the cleaned MLDs suggests that the polymer treatment is mechanically gentle on the surface, since any new scratches/digs generated during the processing would be recorded as particles.

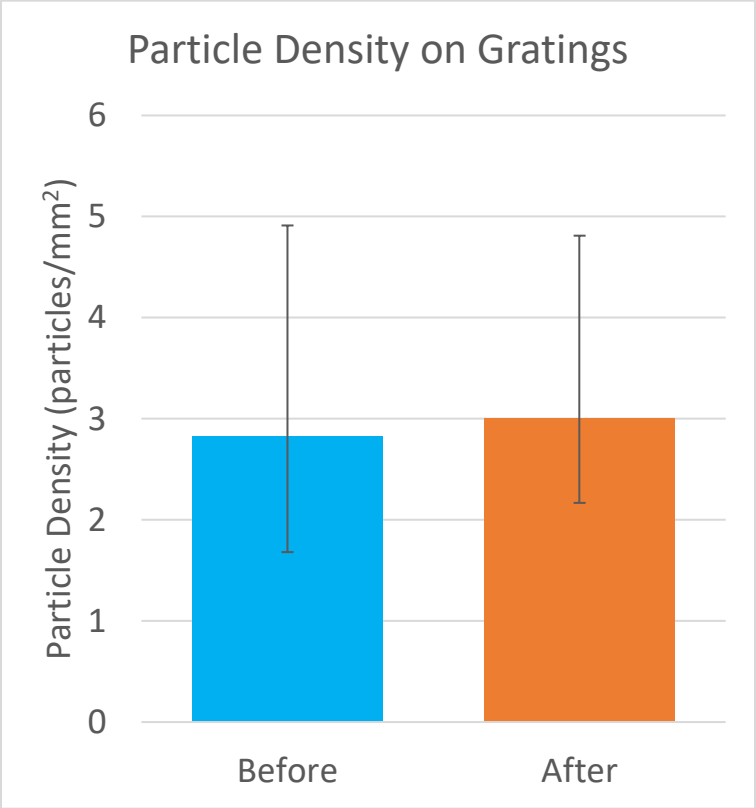

Figure 8: Measured particle density in particles/mm^2 before and after the polymer was used to clean an MLD grating.

5.2 Gratings

The concluding set of experiments in this work involved preliminary testing of the developed treatment process on MLD diffraction grating samples. A grating's structure consists of lines of pillars. For the gratings used, the grating spacing period was 574 nm with 575 nm tall by 200 nm wide pillars. Because of this, the polymer requires a greater cure time to get into the gratings' structure. First Contact™ recommends letting the polymer cure overnight. Aside from this, the procedure for applying the polymer was the same as for the MLD mirrors. When peeling the polymer from the grating, the polymer was peeled parallel to the pillars of the grating to minimize the stress on the pillars.

The initial state of the grating samples was nominally clean, and the particle density did not change after the polymer was used to clean the optic (Figure 8). Since damaged pillars could be counted as particles, as described previously, this indicates that the polymer didn't significantly damage the structure of the gratings. However, in this preliminary work the surface of the polymer after removal did not look to be a replica of the grating surface, which would have generated an appearance of structured coloration. This indicates that the polymer may not have penetrated into the grooves of the grating to properly clean it. Nonetheless, the lack of mechanical damage of the pillars is an encouraging result at this preliminary stage of the research with polymer cleaning of grating samples.

6. Future work

Due to time constraints, it was only possible to successfully peel the polymer from a grating once. Therefore, additional trials are necessary to ensure that the process is repeatable. Another important set of future experiments would involve adjusting process parameters to better clean the structured surface of the gratings. The First Contact™ product line includes a thinner which can be added to the polymer to decrease its viscosity. This could potentially help the polymer to penetrate between the pillars better.

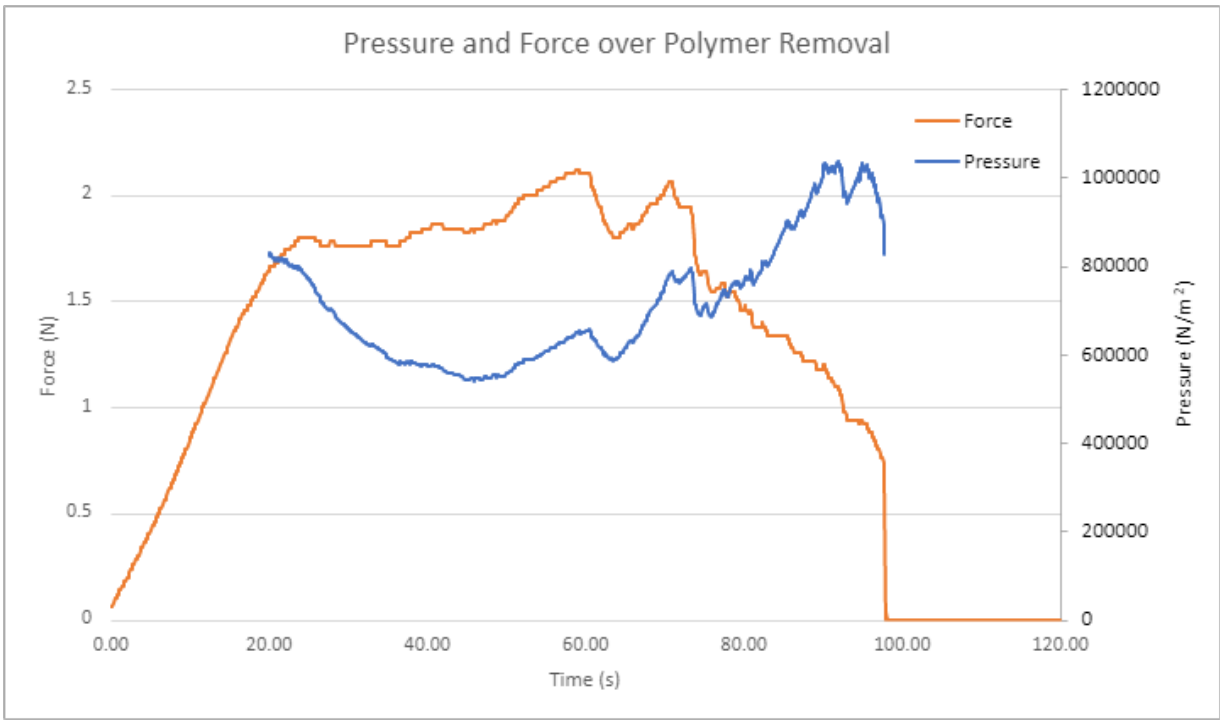

Figure 9: Force and pressure as a function of time during polymer removal from a MLD grating. The pressure, determined using the force, is only plotted over the duration of the polymer coating being peeled.

For structured surfaces such as diffraction gratings, future research could be valuable in the optimization of the polymer removal procedure. Specifically, surface structures change the adhesion of the polymer coating, and the force required may also be a function of the peeling geometry. In our preliminary experiments, the polymer was only peeled parallel to the grating's pillars. Peeling the polymer perpendicular to the grating's pillars may impact the cleaning effectiveness and/or the resistance to mechanical damage of the pillars, due to change of local stresses. While the measurement or calculation of the localized stresses in the pillars would require significant effort and resources, measurement of the total force during the peeling of the polymer may be a useful metric for this purpose. An apparatus was developed using a motorized stage and a force gauge attached to the peel tab, thereby measuring the total force applied as the polymer was being peeled.

An example set of force data during removal of the polymer from a MLD grating is shown in Figure 9. The force data shows that as the polymer is peeled, the force remains relatively consistent between 1 and 2 newtons. Though this data does not directly represent the localized stresses on the pillars, we may be able to estimate the average "pressure" P by dividing the measured force F by the approximate area A that is actively being peeled:

$$P = F/A$$

Note that both *F* and *A* can be functions of time, especially since the samples are not generally rectangular. The active peeling area was approximated as a long thin rectangle, with the short side aligned with the peeling force vector and the long side determined by the width of the sample (determined through video analysis due to the gratings' sector shape). For simplicity, the short dimension of the active area was assumed to have a constant characteristic length of 0.1 millimeters.

By measuring the pressure exerted on the optics during the removal of the polymer, we can potentially establish a practical threshold that diffraction gratings can endure without incurring damage. This information would enable us to make informed decisions on the most appropriate peel tab method, whether it be mesh or floss, and the optimal angle for peeling the polymer in order to prevent damage to the gratings.

7. Conclusions

The commercial polymer First Contact™ was tested as a strip-coat cleaning process for glass substrates, multilayer dielectric coatings, and diffraction gratings for high-power laser systems. Contact angle measurements, particle counts, force measurements, and laser damage testing were used to evaluate the effectiveness of the polymer treatment as a cleaning process. The results showed that the polymer was successful in removing contamination particles from flat optics and that the developed process prevented the treatment from leaving behind its own thin film of contamination. However,

preliminary results from the treatment of MLD gratings suggest the need for development of a modified process for treatment of structured surfaces.

8. Acknowledgements

I would like to thank my advisors, Brittany Hoffman and Kyle Kafka, for their guidance throughout my project. I also extend my appreciation to Dr. Stephen Craxton for enabling this opportunity. Thank you all.

9. References

1. D. Strickland and G. Mourou, “Compression of amplified chirped optical pulses,” Optics Communications 56(3), 219-221 (1985).
2. K. R. P. Kafka, B. N. Hoffman, H. Huang, and S. G. Demos, “Mechanisms of picosecond laser-induced damage from interaction with model contamination particles on a high reflector,” Optical Engineering 60(3) (2021).
3. Photonic Cleaning Technologies, Platteville, Wisconsin
4. H. P. Howard, A. F. Aiello, J. G. Dressler, N. R. Edwards, T. J. Kessler, A. A. Kozlov, I. R. T. Manwaring, K. L. Marshall, J. B. Oliver, S. Papernov, A. L. Rigatti, A. N. Roux, A. W. Schmid, N. P. Slaney, C. C. Smith, B. N. Taylor, and S. D. Jacobs, “Improving the performance of high-laser-damage-threshold, multilayer dielectric pulse-compression gratings through low-temperature chemical cleaning,” Appl. Opt. 52(8), 1682–1692 (2013).

Computational Modeling of Liquid Crystals and Related Materials Using Time-Dependent Density Functional Theory

Vinay Pendri

Pittsford Mendon High School

Pittsford, New York

Advisor: Kenneth L. Marshall

Laboratory for Laser Energetics

University of Rochester

Rochester, NY

September 2023

Abstract

The change in electron density distribution of saturated and unsaturated liquid crystals (LC's) and related molecules in response to 113-fs gaussian laser pulses was modeled computationally using real-time time-dependent density functional theory (rt-TDDFT) with the molecular modeling software *NW Chem*. Calculations were conducted using three different orientations of 900 nm linear polarized light incident on two molecules, one saturated and one unsaturated, to study the change in electron density as a function of incident laser polarization. Results show a significant difference between the localized electron densities of CB15 and CCH, the two molecules of interest, resulting from their differences in saturation. This work will serve as the basis for further investigation of rt-TDDFT's applications in LC and optics research to model areas of application interest such as photochemical reactions, laser damage resistance, polarizability and dielectric constant.

1. Introduction

Liquid crystals (LC's) are a form of matter in between a crystalline solid and an isotropic liquid. The highly organized structure of LC's creates optical effects in short path lengths much more effectively than conventional optical materials. As a result, LC's are employed in high-energy laser systems in circular polarizers and waveplates [1].

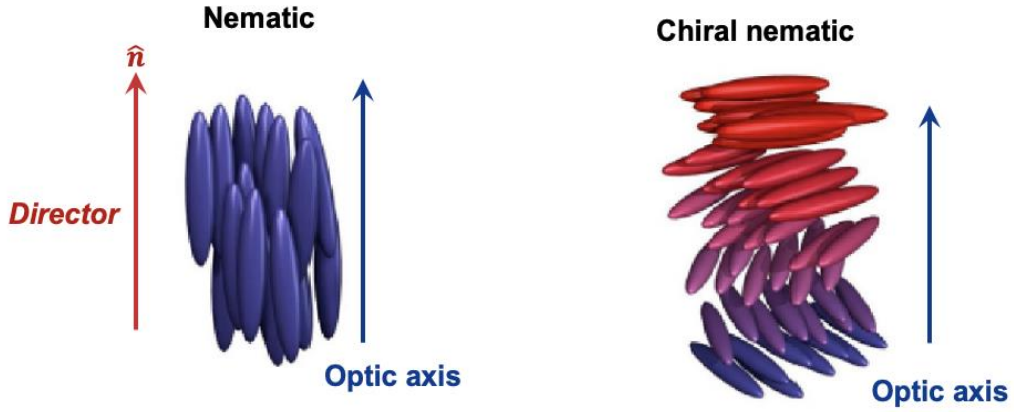

Figure 1: *Nematic and chiral nematic phases of LCs. The optic axis in nematic LC's is parallel to the long molecular optic axis, whereas once a dopant is added to a nematic LC, the chiral nematic LC mixture has an optic axis that is normal to the long molecular axes. The helical structure of chiral nematic LC's is induced by the chiral (asymmetric) functional groups of dopants. [1]*

The three main phases of LCs are nematic, cholesteric, and smectic. This work considers the nematic phase of LC's. Primary applications of nematic LC's are in liquid crystal display (LCD) technology, but they are also frequently used in mixtures with chiral "dopant" materials. The dopants may or may not be LC's. These dopants impart their chirality (twist sense) to the nematic LCs as seen in Fig. 1. Chirality is defined as the intrinsic handedness of a molecule, meaning it is not superimposable onto its mirror

image [2]. Chiral dopants are of interest in optical applications as well because they allow chiral nematic LC mixtures to selectively reflect light by changing the chirality of the host nematic LC mixture [3].

In high-energy laser systems, light passing through the chiral nematic LC mixtures can induce damage by potentially affecting their localized electron density. Electron density is the general representation of the probability of finding an electron in a certain area of an atom or molecule. This factor is important in modeling laser damage in LC's because electron density affects both the chemistry and the optical properties of an LC mixture [2]. The degree of saturation of the LC molecule has a substantial effect on the degree of electron density changes, which in turn impact other optical properties such as dielectric anisotropy and polarizability – respectively, the differences in dielectric responses in different directions and the tendency to induce dipole moments [3].

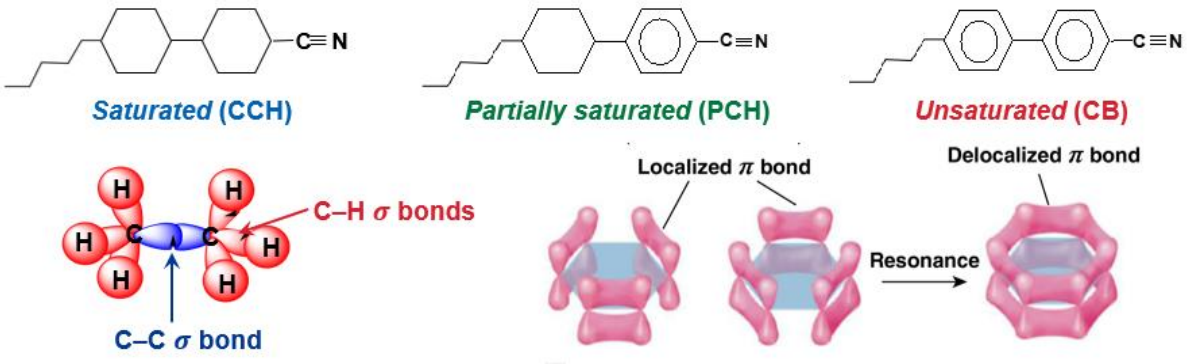

Figure 2: *CCH, PCH, and 5CB (similar to CB15) molecular structures. Delocalized π bonds in the unsaturated 5CB molecule loosely hold electrons while σ bonds in the saturated CCH molecule tightly hold electrons. [1]*

The two molecules used to investigate this phenomenon were 4′-(2-methylbutyl)-4-cyanobiphenyl (CB15) and 4'-pentyl-[1,1'-bi(cyclohexane)]-4-carbonitrile (CCH). Figure 2 shows that there are also variations of these molecules, such as 4-(4-

pentylcyclohexyl)benzonitrile (PCH), that have one saturated and one unsaturated ring. CB15 is an unsaturated molecule with sp hybridization in the ring structures of the molecule, meaning that it has loosely held electrons in delocalized π bonds. In contrast, CCH is a fully saturated molecule with sp^3 hybridization in the ring; it is composed of fully saturated hydrocarbons with only carbon-carbon single bonds [4]. As seen in Fig. 2, the saturated CCH molecule has sigma bonds with tightly held electrons and no *p*-orbitals available for delocalization. All three of these examples, CB15, PCH, and CCH, are of interest for use in high-energy laser optics.

CB15, which is chiral but not an LC, is used as the dopant in chiral nematic LC mixtures used on the OMEGA laser at the Laboratory for Laser Energetics. CCH is a non-chiral LC, but with a minor substitution on the hydrocarbon chain on the left of Fig. 2 could be made chiral. Such a modified CCH is of great interest as a potential replacement with a higher damage threshold for the dopant CB15. Since the damage susceptibility and other properties of CCH and modified CCH molecules depend primarily on the ring structures, the results obtained here for CCH are expected to be valid for the modified molecules.

In order to model how CB15's and CCH's electron densities are affected by high-energy laser pulses and what role the degree of saturation plays in this process, this study used real-time time-dependent density functional theory (rt-TDDFT) [3]. Computational modeling is a much more efficient and cost-effective method for learning about LC properties than manually synthesizing and testing compounds in the laboratory. The main advantage of computational modeling is that a large variety of LC compounds can be

screened simultaneously based on structures and properties, which helps to identify only those compounds that would have the highest probability of possessing the desired properties. This approach minimizes (but doesn't eliminate) the need to synthesize highly complex compounds for testing (which can be difficult for highly chiral structures) and allows one to gain important understandings of molecular interactions that would otherwise be difficult to attain in the lab. An additional benefit is the ability to achieve a deeper understanding of the quantum mechanisms behind the various useful properties of LC's and even predict the chemical and optical properties of yet-to-be synthesized LC's, such as the modified CCH molecules.

2. Previous Research

There are three main methods to perform excited state calculations for a given molecule: *ab initio*, semi empirical, and density functional theory (DFT) [3].

Ab initio, meaning "from the beginning," is an "umbrella" term covering different computational methods such as Hartree-Fock and Configuration Interaction Singles (CIS) [3]. Although *ab initio* can provide higher accuracy excited state calculations than other known methods, it is extremely computationally intensive due to the need to conduct electron orbital calculations and scale up for larger molecules. For instance, the Hartree-Fock method uses the idea that every electron's path is characterized by a single particle function or orbital that doesn't depend on the motion of other particles in the system. The CIS method is similar to Hartree-Fock and incorporates varying electron shells and excitations, but it can only calculate single excitations. Both techniques require starting from basic principles to calculate excited states and heavily neglect electron-

electron interactions and relativistic effects [2]. The result is high computational demand with decreasing accuracy as the size and complexity of the molecules increases, where it is impossible to ignore the interactions of electrons.

In contrast to *ab initio*, the semi-empirical method uses experimental data to fit parameters to reduce computational time. The most common type of semiempirical excited state calculation is Zerner's Intermediate Neglect of Differential Overlap (ZINDO). This method uses superpositions of wavefunctions constructed from ground state orbital configurations [2] and ignores interactions between orbitals, but can account for spin-orbit interactions, which is useful for studying molecular systems with heavier, complex atoms. The use of estimates based on prior data allows for greatly reduced computational time, but less accurate results when compared to other methods such as DFT [2].

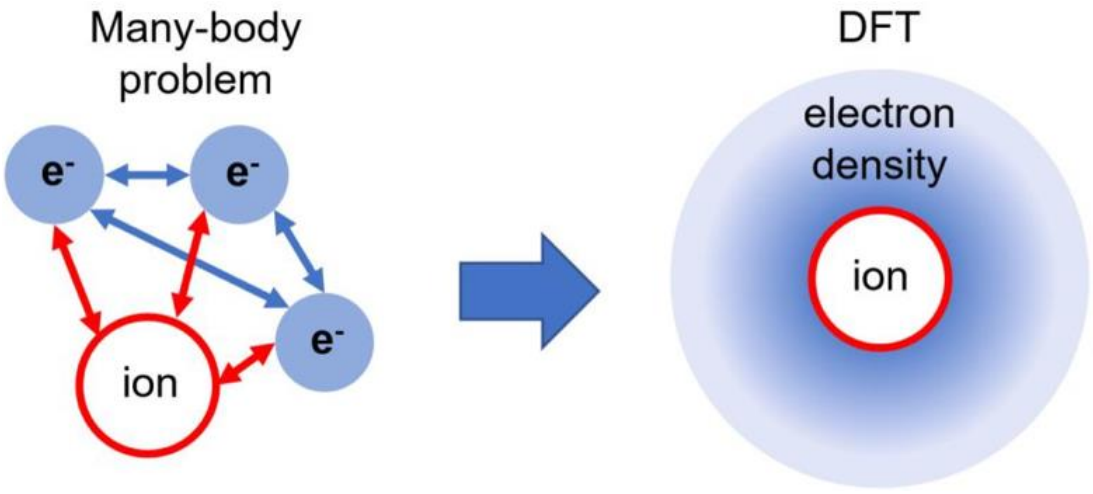

Figure 3: *The many-body problem in regular excited state calculations and electron density used in DFT. The use of electron density eliminates the computational complexity of the many-body problem [6].*

DFT falls between *ab initio* and semi-empirical methods in terms of accuracy and computational intensity. As seen in Fig. 3, DFT replaces the complex many-electron wavefunctions with a three-dimensional spatial function that provides electron density. Since DFT uses electron density in its calculations, it does not rely on the many-electron wavefunction, which contributes to much of the computational strain in the *ab initio* and semi-empirical methods. In the time-dependent Schrödinger equation as seen in Fig. 4, the Hamiltonian energy operator $\hat{H}(t)$ accounts for the energy in the system. Plugging the Hamiltonian operator into the Schrödinger equation solves for the wave function, which gives the system's properties, including electron density [3].

$$\hat{H}(t)\Psi(t) = \mathrm{i}\frac{\partial \Psi(t)}{\partial t}$$

Time-dependent Schrödinger Equation

$\hat{H}(t)$ = Hamiltonian energy operator
$\Psi(t)$ = wavefunction

$$\hat{H}(t) = \hat{T} + \hat{V}_{\mathrm{ee}} + \hat{V}_{\mathrm{ext}}(t)$$

Hamiltonian energy operator

$\hat{H}(t)$ = Hamiltonian energy operator
$\hat{T}$ = kinetic energy
$\hat{V}_{ee}$ = electron electron repulsion
$\hat{V}_{ext}$ = external potential (laser pulse)

Figure 4: *The Time-dependent Schrodinger Equation and Hamiltonian energy operator.*

This idea of using the Time-dependent Schrodinger Equation and Hamiltonian energy operator to input external factors is applied to TDDFT to model disturbances, such as electric fields and laser pulses, that interact with the electron density of a molecule. The variation of TDDFT used in this experiment is rt-TDDFT, which incorporates an external electric field and captures real-time electron density evolution [5]. These time-

dependent calculations can also provide a way to find absorption and emission spectra as well as dielectric constant and polarizability [2].

3. Methodology

The excited state calculations were carried out on the CB15 and CCH molecules after they were first constructed and geometry optimized using the *Maestro* graphical user interface and *Jaguar* computational module in the *Schrödinger Material Science Suite* (see Fig. 5). The atoms, bonds, and bond angles were constructed using *Maestro's* building tools [7]. Then *Jaguar* checked inputted information to ensure it could undergo the energy minimization [8]. This process covered one hundred iterations and optimized the molecule's geometry to minimize energy.

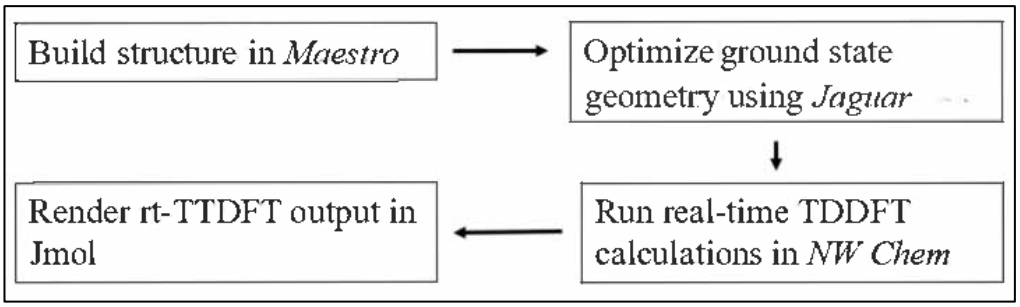

Figure 5: *Methodology overview.*

As depicted in Fig. 6, the next step was to input the energy-minimized molecular structures from *Maestro* into *NW Chem*, where rt-TDDFT calculations were performed [5]. The default basis set, 6-311++G, and hybrid functional, B3LYP, were used for preliminary DFT calculations. A basis set is a collection of functions that represent the electron wave functions of a molecule [3]. The selected sets are usually localized around each atom and impact the accuracy of the DFT calculation. The hybrid functional merges

the exchange correlation energy functional and Hartree Fock density functional in order to adjust for the underestimation of bond strength in DFT. Hybrid functionals also improve the accuracy of excited state calculations [2].

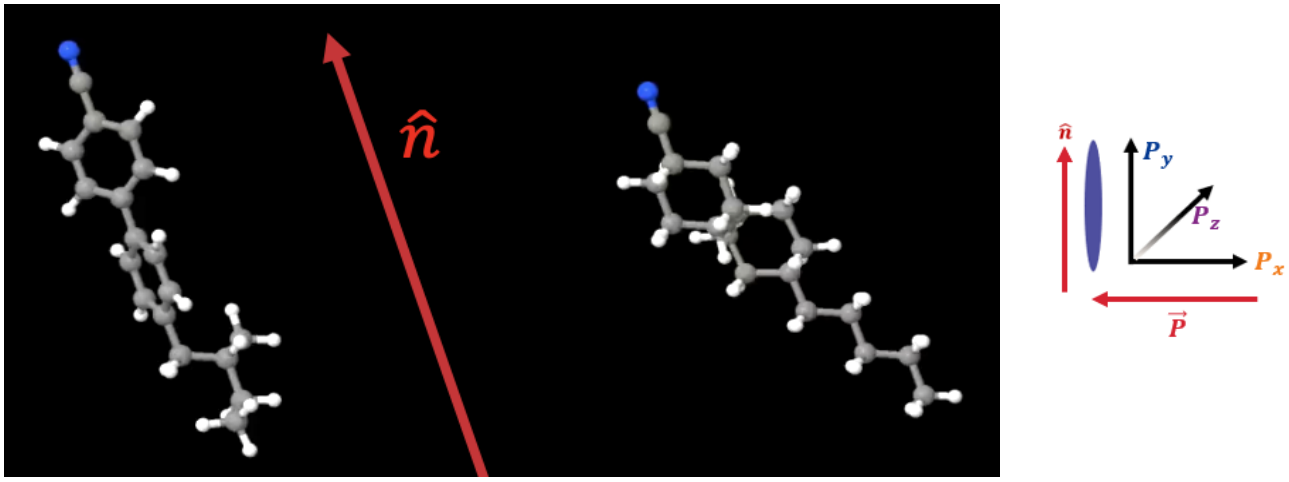

Figure 6: *Optimized energy structures inputted into NW Chem. CB15 (left) and CCH (right) are shown with respect to the director n̂. The director is the net average direction of the long molecular axis of the molecules in the condensed phase [4]. X, y, and z light polarization directions (P_x, P_y, P_z) are displayed in the graphic (right).*

The rt-TDDFT calculations simulated a 900-nm 113-fs Gaussian laser pulse that was polarized with respect to the x, y, and z axes in three separate trials as seen in the small graphic on the right side of Fig. 6. The 900 nm wavelength was chosen to minimize the impact of optical absorbance and selective reflection that can that occur at the 351 and 1053 nm wavelengths. To maximize use of computational resources, this study modeled 65% of the 113-fs Gaussian laser pulse width applied in each simulation. Single molecules in the gas phase were used to minimize the complexity of calculations that would be introduced by electrostatic and Van der Waals forces of neighboring molecules in the condensed phase. The 113-fs time frame was chosen as a compromise to both minimize computational load but still capture the electron density at peak intensity and directly after

the peak. Conducting these same calculations over a broader temporal range (ps) was estimated to take up to *40 years* using six nodes and 240 cores on the LLE supercomputing cluster DELUGE with a total of six simulations run for each polarization of light on each molecule. Total computational times for the femtosecond laser pulse regime were around 168 hours for each incident polarization modeled. Calculations for each polarization direction for CB-15 took 54 hours, while similar calculations on CCH took ~75 hours. This increased computational time can be attributed to a larger number of electron-electron interactions in the saturated CCH molecule.

4. Results and Discussions

Excited state electron densities were calculated for CB15 and CCH for x, y, and z polarized Gaussian laser pulses. The results are show in Fig. 7, rendered using Jmol [9]. Significant differences in the electron densities of CB15 and CCH among different polarizations of light and between the molecules can be seen.

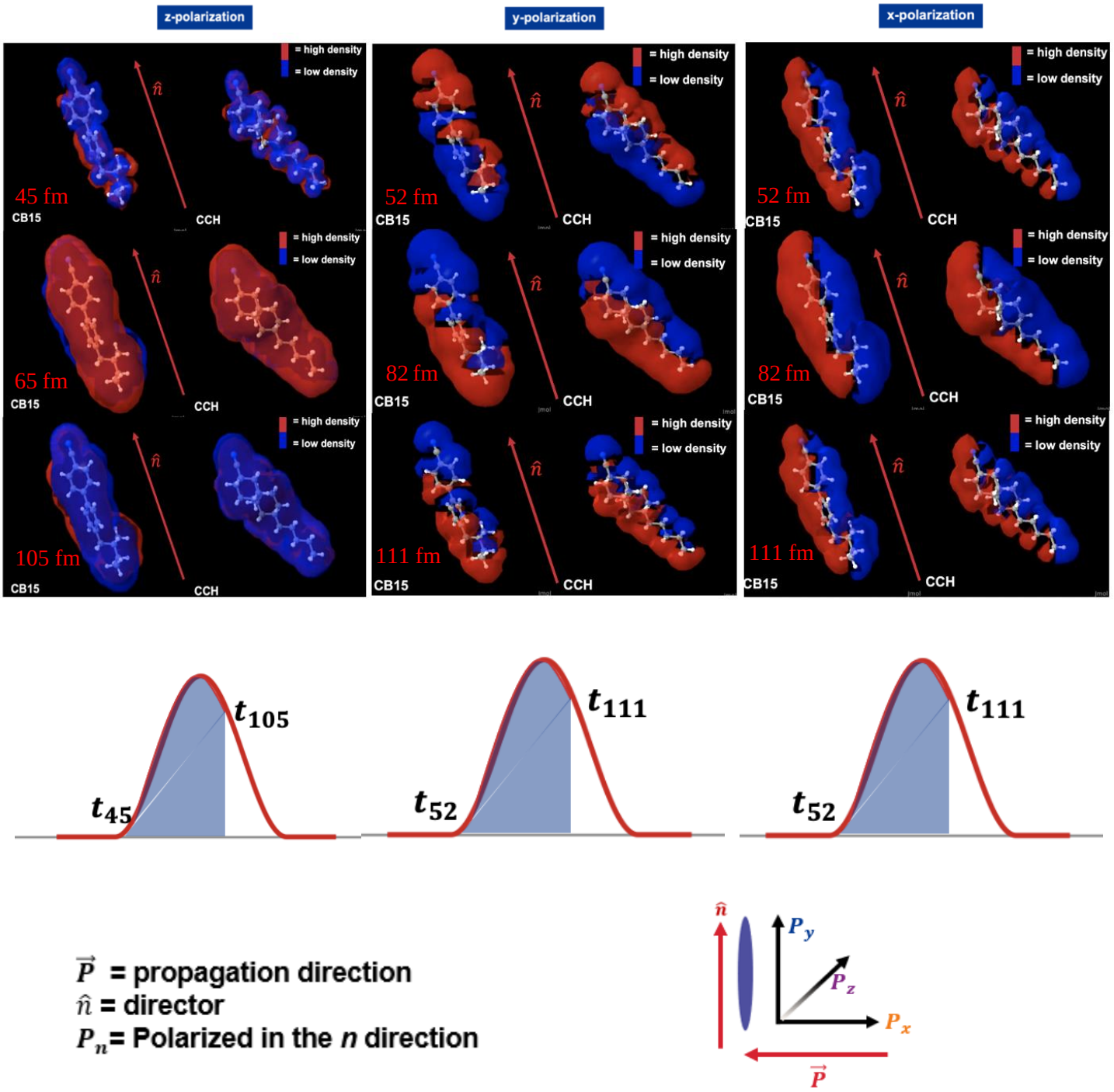

Figure 7: *Time-resolved snapshots of rt-TDDFT electron density maps for CB-15 and CCH for each incident polarization of light. The portion of the femtosecond pulse width represented by each set of electron density maps is shown beneath each map. The vector diagram defines the coordinate axes, the director orientation, and, for z and y polarizations, laser pulse propagation direction. For x polarization, the propagation is along the y direction.*

The incident polarization angle of the laser affects the electron-rich and electron-poor hemispheres of the molecules and suggests that light polarization may vary the impact on electron density. The polarization of the electric field is seen to oscillate perpendicular to the propagation axis. In the simulation, the laser pulse polarization also describes the direction of the electric field's oscillations. Figure 7 shows that the high electron density and low electron density area fluctuations are a response to the varying external electric field polarizations.

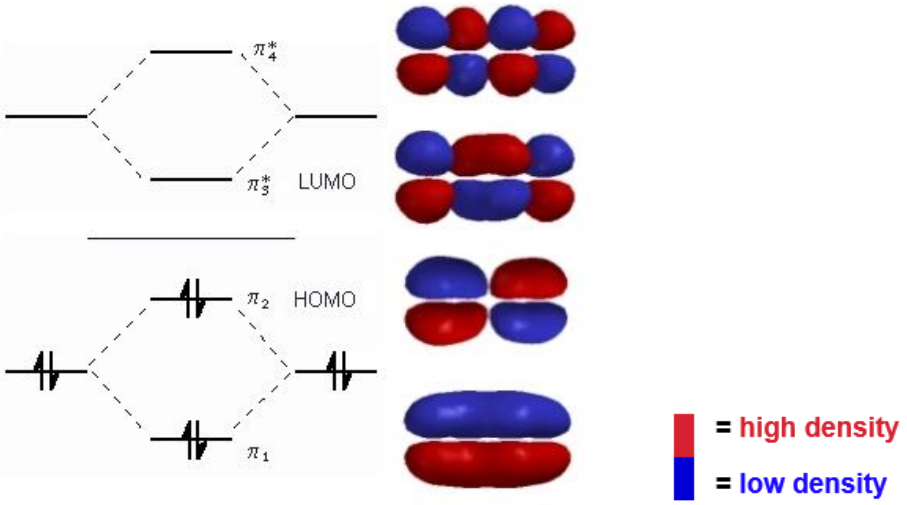

Figure 8: *Example of HOMO LUMO transitions in molecules. The delocalized π electrons cause the electron densities to vary [4]. The variously numbered π symbols represent the energy states of each electron.*

Figure 7 shows that there is a significant difference between the localized electron densities of CB15 and CCH. This is due to differences in saturation. Displayed in Fig. 8, this phenomenon is due to the delocalized π bonds and electrons present in CB15 that contribute to HOMO (Highest Occupied Molecular Orbital) and LUMO (Lowest Unoccupied Molecular Orbital) energy transitions [3]. When a delocalized π electron in an unsaturated molecule like CB15 is excited, changes in the electronic energy of the

molecule occur. The cloud-like formation of π electrons can allow for larger changes in the molecule when perturbed. Figure 7 displays that the electron densities shift to the director's direction of both molecules during the simulation, but more so in CB15 due to greater numbers of π electrons.

5. Conclusions

Real-time TDDFT was used to calculate the excited state electron densities of the molecules CB15 and CCH when perturbed by 900 nm, 113 fs Gaussian test pulses of x, y, and z, polarizations. A methodology has been developed to perform rt-TDDFT calculations on molecules and render images through Jmol in order to capture electron density. The temporal variations of electron density depend on the molecules' inherent π-electron delocalization, the propagation direction, and the incident laser polarization angle relative to the long molecular axis.

This study is the first step into the computational modeling of dopants used in chiral nematic LC mixtures employed in high energy optics, and gives insights on the changes in electron density distribution probabilities during the initial and peak portions of the incident femtosecond-regime pulse. Of even more significance is what happens to the electron density distribution on the trailing portion of the pulse, as non-reversible changes in electron density could indicate the onset of chemical reactions that could be precursors to laser-induced damage (Fig 9).

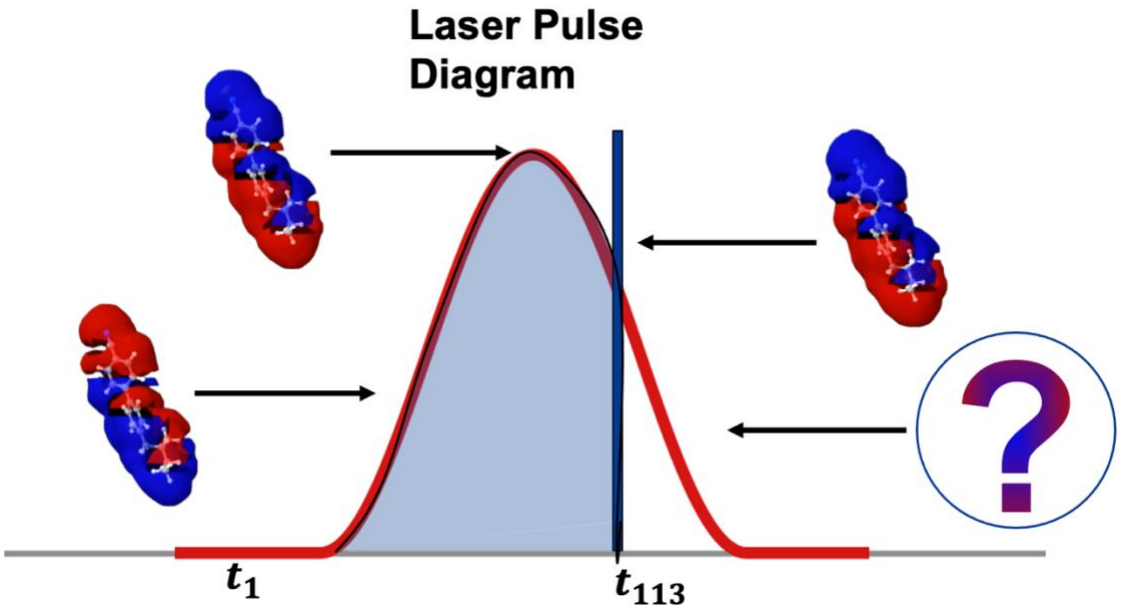

Figure 9: *Laser pulse diagram showing the need for future work modeling the pulse decline, since the pulse's incline and peak have already been modeled. The images shown are taken from Fig. 7 for CB15 and y polarization.*

The success of this method will aid the future development of computational models using electron density to efficiently determine the properties of novel LC materials and better understand the complex mechanisms behind the many useful qualities of these materials. This information is also useful for determining potential decomposition methods for molecules such as CB15 and CCH. This study determined that there is a difference in electron density reactions between different light polarizations, but this phenomenon requires further research in order to better understand the reasons behind it. The saturation levels of CB15 and CCH also affect the electron densities by varying the rate at which the electron density changes.

In this study, the default basis set and hybrid functional were used, so further investigation into different basis sets and hybrid functionals is needed to determine the optimal combination. Once basis sets are optimized, future work can commence on molecular dynamics to involve the solvent in simulations, since current simulations only focus on the electron densities of dopant molecules. This is important because the solvent is just as essential to LC solutions as the dopant.

6. Acknowledgments

I thank Dr. Stephen Craxton for the incredible opportunity to conduct research at LLE; Mr. Kenneth L. Marshall for his endless support and guidance throughout the research process; Dr. Nathaniel Urban for his advice and technical guidance; Dr. William Scullin and Dr. Kenneth Anderson for their assistance in accessing and using computational resources; Julia Kubes and Leonid Solodov for their mentorship; Ms. Kim Truebger for managing the program's logistics; Jacob Deats and Eugene Kowaluk for their photography. Lastly, I am grateful to the University of Rochester, the U.S. Department of Energy, and the National Nuclear Security Administration for funding this research.

References

[1] Marshall, K. L. et al; “The Effect of Incident Polarization Handedness and Ellipticity on the Laser-Damage Resistance of Oriented Liquid Crystals in the Nanosecond Regime” (Conference Presentation); SPIE proceedings, October 2021.

[2] Wang, R., “Computational Modeling of Spectral Properties of Nickel Dithiolene Dyes”; LLE Summer High School Research Program, 2006.

[3] Collings, P. J. and Patel, J. S., Handbook of Liquid Crystal Research, Oxford University Press, 1997.

[4] Vollhardt, K. Peter C. and Schore, Neil E. Organic Chemistry: Structure and Function. Fifth Edition. New York, N.Y.: W. H. Freeman Company, 2007.

[5] Real-Time TDDFT, NWChem, https://nwchemgit.github.io/RT-TDDFT.html.

[6] Posysaev, S., “Applications of density functional theory for modeling metal-semiconductor contacts, reaction pathways, and calculating oxidation states,” University of Oulu Graduate School Report Series in Physical Sciences, Report No. 123, 2018.

[7] Schrödinger Release 2023-2: Maestro, Schrödinger, LLC, New York, info@schrodinger.com, 2023.

[8] Bochevarov, A.D.; Harder, E.; Hughes, T.F.; Greenwood, J.R.; Braden, D.A.; Philipp, D.M.; Rinaldo, D.; Halls, M.D.; Zhang, J.; Friesner, R.A., "Jaguar: A high-performance quantum chemistry software program with strengths in life and materials sciences," Int. J. Quantum Chem., 113(18), 2110-2142, 2013.

[9] Jmol development team. (2016). Jmol. Retrieved from http://jmol.sourceforge.net.

Investigation of Microwave-Induced Chemical Etching in CR-39

Jayden Roberts

Brockport High School

Brockport, NY

Advisor: Steven Ivancic

Laboratory for Laser Energetics

University of Rochester

Rochester, NY

December 2023

Abstract

CR-39 is a solid-state nuclear track detector that can be used to collect information on critical performance metrics of inertial confinement fusion implosions, such as the areal density of the confined fuel. Charged particles emitted from reactions occurring inside the target damage polymer bonds in the CR-39. These damages are on the scale of nanometers, and thus require further treatment to be recorded by instruments such as optical microscopes. LLE currently uses a several-hour chemical etching process to develop particle tracks. Microwave radiation has been proposed to work in tandem with chemical etching to greatly increase the rate at which tracks develop. A study of microwave-induced chemical etching was undertaken and found to fully develop alpha particle tracks in CR-39 in 30 minutes as opposed to 6 hours in conventional chemical etching used today.

Introduction

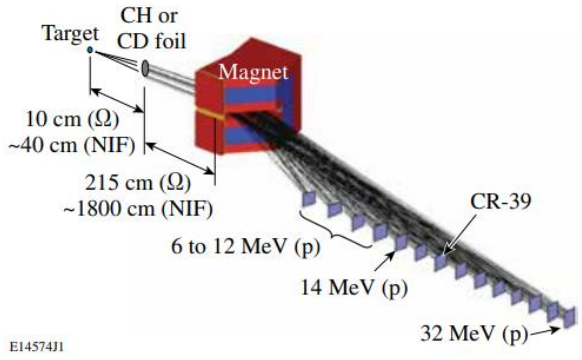

Figure 1: A diagram of the Magnetic Recoil Spectrometer. Energetic neutrons resulting from the fusion implosion collide with a CH or CD foil, producing energetic protons or deuterons. These charged particles pass through a magnet, causing them to be deflected by the Lorentz force onto a series of CR-39 pieces. The deflection angle is inversely proportional to the particle's velocity, allowing the particle's energy to be deduced by its position. Figure from Ref. 2.

Nuclear fusion is the process of fusing two lighter nuclei into a heavier nucleus, releasing energetic particles in the process. Targets can be manufactured with a variety of isotopes, but deuterium and tritium are the preferred pair at the Laboratory for Laser Energetics (LLE) for their energy efficiency. For relevant information to be gleaned from a fusion implosion, diagnostic instruments must be fielded to capture data from the target. The Magnetic Recoil Spectrometer (MRS)[1,2]—shown in Figure 1—is one of many such diagnostics fielded on the OMEGA laser at LLE. The MRS is used in conjunction with other charged-particle diagnostics to infer parameters such as areal density, which is calculated by the equation:

$$\rho R = \int_0^R \rho(r) dr,$$

where $\rho(r)$ is the density at radius r. The areal density quantifies the quality of the compression of a target during an implosion.

Energetic neutrons from the fusion implosion collide with a CD or CH foil on the front of the MRS diagnostic, releasing a charged particle known as a recoil deuteron or recoil proton, respectively. This charged particle then travels through a magnetic field, which deflects the

particle onto one of a series of CR-39 pieces. The piece absorbs the energetic particle, leaving nanoscale damage—referred to as latent tracks. These pieces are then recovered from the diagnostic and must undergo further development to enlarge the track pits to the microscale. The currently preferred method for this development is chemical etching.

Chemical etching works by introducing an etchant, usually a basic solution such as sodium hydroxide, to the CR-39 piece at a high temperature. This high temperature allows the etchant to attack the polymer bonds damaged by the charged particles. This mechanism has been explored in the literature and is the result of the etchant preferentially attacking regions with free radicals displaced by the charged particles[3]. This process, given sufficient time, results in the conical pits shown in Figure 2.

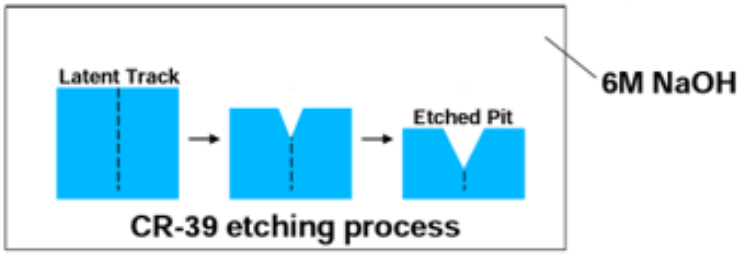

Figure 2: Etching of CR-39. Charged particles are slowed down inside of the CR-39, leaving behind a trail of broken polymer bonds—referred to as latent tracks. These tracks can then be developed using an etching process, revealing conical pits.

It has been shown in the literature that the presence of microwaves can speed up the etching process. This new method is called microwave-induced chemical etching (MICE)[3,4] and has been shown to substantially increase the rate of etching.[4] Though referenced literature has introduced MICE as a means of developing latent tracks on CR-39, further investigation is required to implement such a method at LLE.

Methods and Materials

The experimental setup is shown in Figure 3. The setup consists of a variable-power 1000-Watt microwave, four 400 mL Teflon beakers, and a thermometer.

Figure 3: The experimental setup. Teflon beakers and lids are used to ensure a microwave-safe vessel for the etchant. The thermometer is placed in a beaker of water after temperature measurements are taken to prevent a buildup of etchant on laboratory surfaces.

The etchant, 6 N sodium hydroxide, was decanted into four beakers, with each beaker containing 200 mL of etchant. The beakers were then covered with lids to minimize evaporation, though a small opening was kept, ensuring that there would be no build-up of pressure resulting from vapor. These beakers were then placed into a variable-power microwave and microwaved for two minutes. The beakers were then removed from the microwave and the etchant was stirred to ensure a uniform temperature distribution. The temperatures of all four solutions were measured, and the beakers were placed back into the microwave for another two minutes. This procedure was carried out until the solution reached 100°C. This process has been standardized in the literature[3]. The results of this procedure can be seen in Figure 4, which plots temperature against time for varying power settings. The plotted temperature readings were calculated by taking the average temperature of all four beakers.

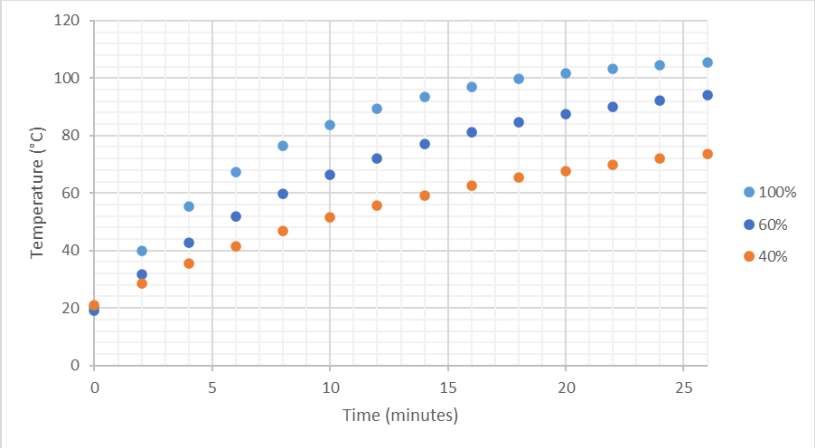

Figure 4: A summary of temperature over time for varying power settings. The beakers initially warm up quickly but temperatures eventually plateau due to the equilibrium between heating and cooling. The former occurs because the solutions are being microwaved, and the latter results primarily from the beakers being removed from the microwave for a temperature reading.

To use this data for etching, we must first account for the cooling during temperature measurements. This cooling would not occur if the beakers were simply left in the microwave. We fit a differential equation modeling constant heating and Newtonian cooling to resolve this issue:

$$\frac{dT}{dt} = s - k(T - a),$$

where s represents the constant rate of increase of temperature due to the microwave heating source, k represents the resulting cooling, T is the modeled temperature of the beakers that is being solved for, t is time, and a is the room's ambient temperature. This differential equation can be solved by separation of variables, giving the result:

$$T(t) = a + c_1 e^{-kt} + \frac{s}{k},$$

where c_1 is dependent on initial conditions. Substituting $t = 0$ yields

$$T(0) = a + c_1 + \frac{s}{k},$$

which we know is the ambient temperature of the room; thus,

$$c_1 = -\frac{s}{k}, \text{ giving,}$$

$$T(t) = a + \frac{s}{k}(1 - e^{-kt}),$$

which can then be used to fit our data. To do this, a Python program was written using the curve fit function in SciPy[5]. The resulting parameters are given in Table 1 and the fitted curve is shown in Figure 5.

Power Setting	$\boldsymbol{s}$ $(\frac{^\circ C}{s})$	$\boldsymbol{k}$ $(\frac{1}{s})$
40%	4.4	0.07
60%	6.7	0.08
100%	11	0.1

Table 1: Heating and cooling parameters, s and k respectively, for various power settings. As expected, the fitted values of s are proportional to the power setting of the microwave. It was expected that k would be approximately constant regardless of power setting, which is the case. The variation seen is due to measurements taking slightly longer by random chance.

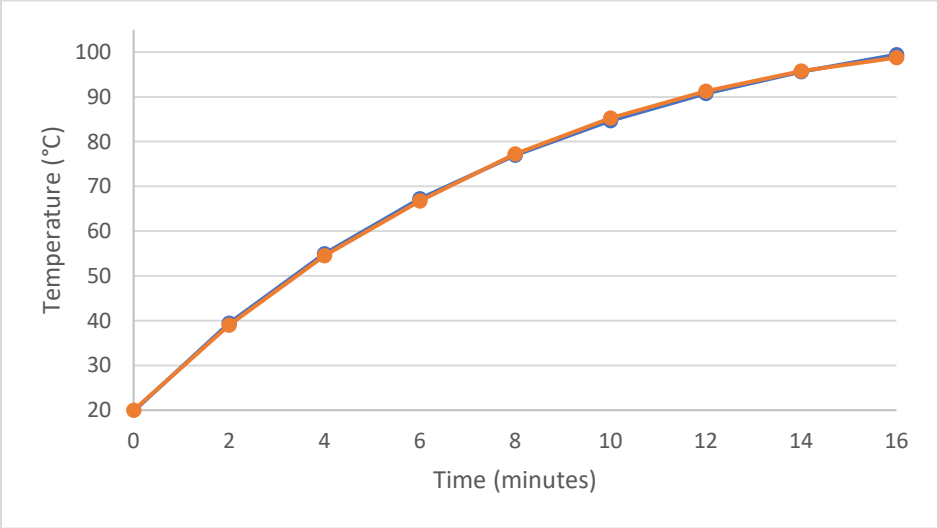

Figure 5: The recorded and modeled temperatures plotted over time for the 100% power setting. The orange data plots are the recorded data and the blue data points are the modeled temperatures calculated using the parameters in Table 1.

For optimal etching conditions, the etchant must be first heated to 70°C. Then, a step of etching can be carried out until the solution reaches 100°C. Etching must stop at this temperature to ensure data integrity[4]. The etchant is then allowed to cool back to 70°C. This was done by taking intermittent temperature measurements in conjunction with a Newtonian cooling model to

approximate how long cooling will take. This step etching process can be repeated until the etch duration has elapsed. This corresponds to step etching durations of 7 minutes, 4 minutes, and 3 minutes for 40%, 60%, and 100% power levels respectively, with a 4-minute preheating period at 100% power to reach the necessary 70°C for etching. These durations were calculated directly from the constant rate of increase of temperature from the microwave.

The center of a piece of CR-39 was irradiated with an Americium alpha particle source for five seconds at a distance of 0.5 cm. The alpha particles did not pass through a collimator. The beakers of etchant were then brought to 70°C per the previously outlined process. The piece of CR-39 was then placed into a beaker and microwaved for the prescribed 3-minute interval. After this time the piece was scanned, and the average particle pit diameter was measured.

Results

A region of the CR-39 was captured by an optical microscope at various times, showing the growth of alpha particle pits. Typical images are shown in Figure 6. Further inspection via the microscope revealed a uniform development of alpha tracks throughout the central region of the piece.

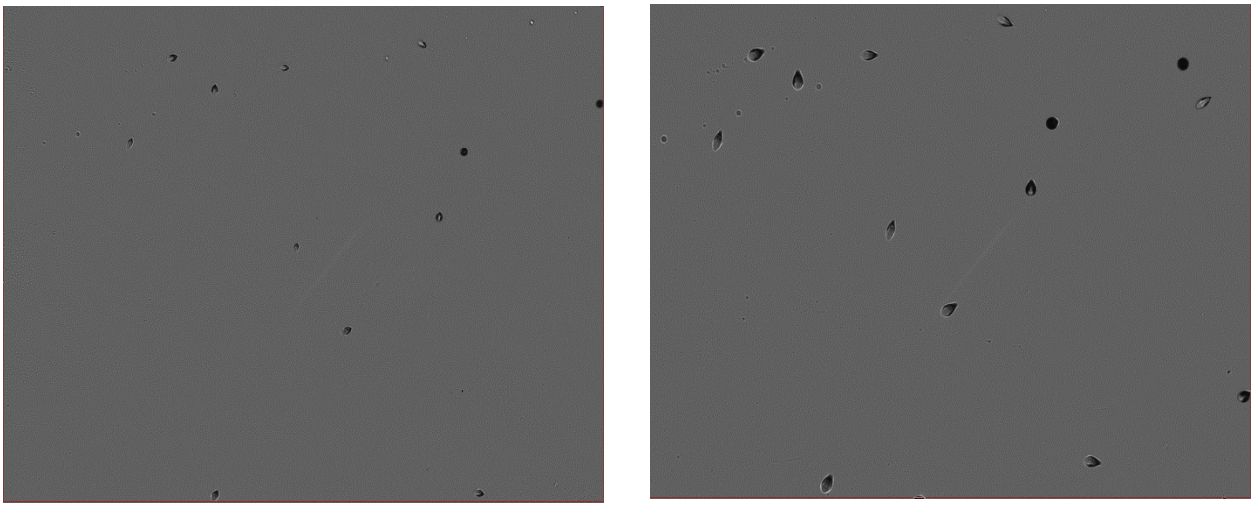

a. b.

Figure 6: Developing alpha particle tracks on CR-39. (a) A piece of CR-39 irradiated with alpha particles after 12 minutes of etching. (b) The same piece after 30 minutes of etching, where the pits are fully developed. The pieces were examined under the same optical microscope in the same region to ensure consistency.

Furthermore, the oblique incidence of the alpha particles is revealed upon inspection. This geometry corresponds to our expectation of tracks from an uncollimated alpha source. This is an important first step in ensuring the signal integrity of a piece prepared using MICE. Following the MICE procedure, we develop CR-39 pieces in 30 minutes, as opposed to the 6 hours required for chemical etching.[6]

Conclusion

This project investigated the merit of using microwave-induced chemical etching as an alternative to traditional chemical etching methods. The goals were to outline the process of microwave-induced chemical etching and supply a comparison between the duration necessary for the development of alpha particle pits. MICE was found to be a superior option, with traditional methods taking 6 hours to achieve fully developed alpha particle tracks whereas MICE develops latent particle tracks after 30 minutes.

The mechanism by which microwaves influence etching has been proposed in the literature[3]. Microwaves heat objects when dipoles within the object interact with microwave radiation, giving rise to dielectric heating. This mechanism favors polar regions, such as those with free radicals created by the alpha particles. This enables the etchant to more favorably attack latent particle tracks, giving rise to a shorter etch duration.

Further areas for exploration with MICE include testing for uniform development of pits throughout all regions of the CR-39 piece, and using recoil protons instead of alpha particles—which would entail an experiment involving a CH or CD foil along with a neutron source. Additionally, a comparison of the signals on pieces prepared using traditional methods and MICE would be integral. These experiments would serve to prove MICE as a reliable alternative in more than just duration.

Acknowledgments

I would like to thank my advisor Dr. Steven Ivancic for his invaluable guidance throughout this project. I thank Hannah McClow for always being in the lab to lend a hand and showing me how to use the scanning technology. Thank you to Dr. Peter Heuer for his willingness to explain various diagnostics to me and for always encouraging me to do my best work. Thank you to Alexa LaPierre for her help with getting things set up in the chemistry lab and her diligence in finding exactly what we needed. Lastly, I would like to thank Dr. Stephen Craxton for this amazing opportunity.

References

1. Frenje, J. A., et al. “First measurements of the absolute neutron spectrum using the magnetic recoil spectrometer at OMEGA (invited).” *The Review of Scientific Instruments* vol. 79, 2008: 10E502.
2. Casey, D. T., et al. "Measuring the absolute deuterium–tritium neutron yield using the magnetic recoil spectrometer at OMEGA and the NIF." *Review of Scientific Instruments* 83.10 (2012): 10D912.
3. Tripathy, S. P., et al. “Microwave-Induced Chemical Etching (MICE): A Fast Etching Technique for the Solid Polymeric Track Detectors (SPTD).” *Nuclear Instruments & Methods in Physics Research*. Section A, Accelerators, Spectrometers, Detectors and Associated Equipment, vol. 612, no. 2, 2010, pp. 421–426.
4. Sahoo, G. S., et al. “Optimization of Microwave-Induced Chemical Etching for Rapid Development of Neutron-Induced Recoil Tracks in CR-39 Detectors.” *Nuclear Instruments & Methods in Physics Research*. Section A, Accelerators, Spectrometers, Detectors and Associated Equipment, vol. 739, 2014, pp. 83–88.
5. Virtanen, P., et al. “SciPy 1.0: Fundamental algorithms for scientific computing in python.” *Nature Methods*, vol. 17, no. 3, 2020, pp. 261–272.
6. Hicks, D. G. “Charged-Particle Spectroscopy: a New Window on Inertial Confinement Fusion.” Diss. Massachusetts Institute of Technology, 1999, pp. 117-118.

CONTAINERIZED APPLICATION MANAGEMENT FOR CLOUD BASED SCIENTIFIC ANALYSIS

Cameron J. Ryan
Advisor: Richard Kidder
McQuaid Jesuit High School
cjryanwashere@gmail.com

Laboratory for Laser Energetics
University of Rochester
May 2023

ABSTRACT

Experimental data from diagnostic reports at the Laboratory for Laser Energetics (LLE) used for statistical analysis is accessed through the LLE web Application Programming Interface (API). The analysis software development pipeline is inhibited by the lack of any existing software for loading, formatting, and abstracting data from the web API. New software needs to be created redundantly to load data from the API every time new analysis software is made, or whenever external scientists make software that analyzes data observed from experiments at LLE. An application management system using software containers was researched and developed to allow new or external scientists to securely develop analysis software with LLE's physical computational resources, as well as a code-sharing repository for the distribution of diagnostic-reading software through GitLab. This can all be accessed through an easy-to-use web interface.

1 Introduction

Scientists at the Laboratory for Laser Energetics (LLE) and other nuclear fusion laboratories continually collaborate in the creation of software that analyzes data gathered from experiments conducted at LLE. Many of these software development projects are not open-source, and so their source code cannot be made publicly available through an online code repository service, such as GitHub. This is problematic, because scientists often need to use software that has already been created, yet have no clear method of discovering what they need. Additionally, scientists working at laboratories outside of LLE that have been granted permission to use data collected from experiments at the laboratory do not have a clear way to discover or access software that has been created to read and abstract data from diagnostics. This research aims to provide a method for internal and external scientists to collaborate in the development of software [1].

2 Challenges posed by distributed software collaboration

2.1 General software development

Most software development at LLE is version-controlled and shared using GitLab, a locally hosted Git repository service [2]. GitLab, as it has been previously used, is a competent tool for allowing scientists to collaborate together on a single project; however, scientists working on different projects have no way of sharing code that performs the same purpose. Because of this, scientists often redundantly create software for some particular task, such as reading data from LLE's shot diagnostic database. For example, if a scientist wants to create software that performs analysis on data gathered for a particular experiment, they will need to write code from scratch that will load data from the database Application Programming Interface (API) and abstract the data to provide the analysis that they need. Considering that what they create will likely have already been created, this is redundant and time wasteful.

2.2 External Users

An additional problem to be considered is scientists from external laboratories who are performing experiments in collaboration with scientists at LLE and have access to the LLE database API, through an LLE-specific API access token. External users cannot use GitLab, because it creates various potential security issues, and a potential challenge due to a need to manage the authentication of all their GitLab accounts. As external users are likely to find the most difficulty in figuring out how to write code for tasks such as reading data from the database API, code sharing platforms should be inclusive of them by not directly accessing the GitLab Representational State Transfer (REST) API [3].

3 Proposed solution

The purpose of this work is to demonstrate a web platform for scientists to discover software from Git repositories that performs a desired function, so that they do not have to do it themselves. Ideally, it should accomplish the following items:

- Both internal and external scientists should be able to use the web platform to browse Git projects that have already been created, and whose creators consent to having their code shared internally.
- The web platform should allow for scientists to edit code, and utilize the functionality of Git. With Git, scientists should be able to branch and merge code for various projects.

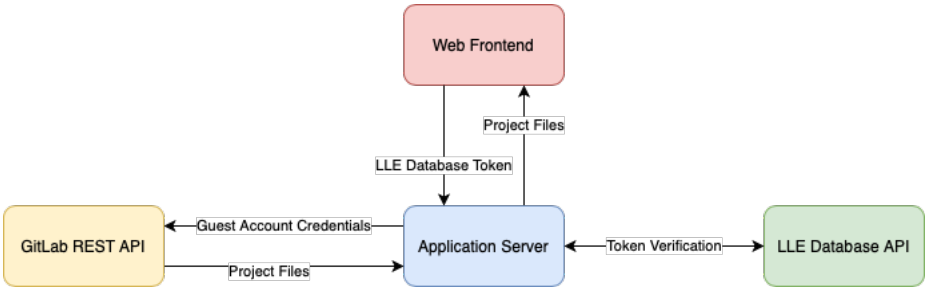

Figure 1: With indirect authentication, external users cannot directly access the GitLab REST API. However, they are able to authenticate through this project's server by sending a request with their database authentication token, which will be verified by the LLE database API, allowing them to access the GitLab projects as a guest user.

Figure 2: With direct authentication, users directly access GitLab on the web front end through the GitLab REST API. With this method, users are essentially using GitLab, except with additional features for exploring projects.

- Scientists should be able to run code that they have found or edited remotely on a server at LLE. When they run software, their computational resources should be regulated, and they should be able to save their work remotely. This can be accomplished through the use of a virtualization software.

4 Developing with GitLab

GitLab allows for developers to access many of the functions of Git through its REST API. This allows the main functionality of Git to be accessed from a web platform. Users can use their GitLab authentication credentials on the web platform, allowing them to open projects, browse files, and create new branches with their own accounts [3]. The two forms of authentication are described in the following subsections.

4.1 Indirect authentication

As mentioned, LLE is unable to provide GitLab accounts to all users from external laboratories. However, users can access data gathered from experiments through the database API. To allow them to access GitLab projects that contain code for reading data from diagnostics that they have access to, they can authenticate indirectly using their database access token.

When an external user is given access to data taken from certain shots, and certain diagnostics in the database, they can login to the web platform with their database access token. The server (for the web platform) will request which diagnostics the user has access to from the database API, find all GitLab projects that read data from that specific diagnostic, and return the source code for those projects to the user in the web front end. This is demonstrated in Figure 1.

Since the GitLab REST API must be accessed by a specific GitLab account, the creation of a guest user account allows for the server to access GitLab for the user who is authenticating with their database API token. Note that while this is designed for external users, it can also work for anyone with access to the database, thus internal users as well.

4.2 Direct authentication

If an internal user (LLE employee) wishes to browse GitLab projects with loading and analysis code for any particular diagnostic that they have access to, they may do so by directly accessing the GitLab REST API with their authentication credentials. If they provide their database API token, the web frontend will automatically filter what projects they have access to (based on what diagnostics they may access), and will return to them the source code for those projects. This is demonstrated in Figure 2.

Figure 3: Screenshot taken from the web front end. Users can search Git projects by diagnostic, browse the file tree of the Git project, and read files in the project

5 Web interface

To facilitate the discovery of Git projects, a web front end and server were created to indirectly browse Git projects. They could also be used to safely and securely access the computational resources of the server.

Additionally, since it would be unsafe to allow users to directly run their analysis code on the operating system of the server, containers were chosen to safely compartmentalize applications run by users. The reasoning behind this decision is further elaborated in 6.

5.1 Front end

The front end was created using JavaScript, HTML, and CSS. As mentioned, it was created with functionality to access GitLab through the GitLab API (or the server). The interface is organized on the basis of what diagnostic its code analyzes (each diagnostic corresponds to a set of projects that analyze data from that diagnostic). When the user has found the diagnostic, for which they need code to load data from or analyze, they are able to browse projects and their file trees. A screenshot of the front end's web interface can be seen in Figure 3.

Early versions of the front end allowed for the user to edit files directly using an embedded code editor. Once finished with editing files in the project, they could save their edits through the GitLab API if they have access to the project, and push their changes to a new branch if they do not have access to the project. New branches will be accessible by all

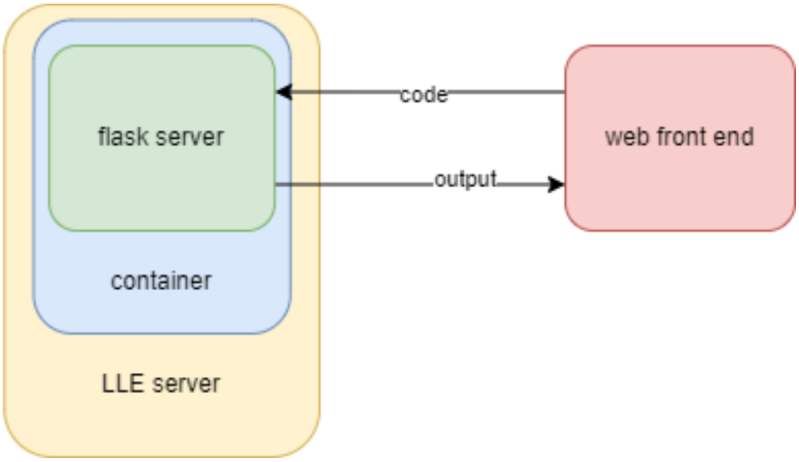

Figure 4: A demonstration of the web back end with a Flask server

users browsing a certain diagnostic, and will be owned by the user's GitLab account. If the user is an external user who is indirectly authenticating, then the branch will simply be owned by the guest user. Developing a better method for external users to save and have control over project branches they have created may be the subject of future work.

Furthermore, users would be able to directly run code on the server from the web interface as they edited it. This functionality is explained in 5.2.

5.2 Back end

The back end experienced various iterations over the course of this work. Initially the back end was a NodeJS server [4], and accessed the GitLab REST API by executing a series of python scripts that use the GitLab python library [5]. Furthermore, the back end authenticates users with their LLE database access token, so that they may access GitLab projects they have access to with the guest GitLab account.

When users would want to run code that they have found or edited, the back end would spawn a container, which runs a Python Flask server [6] in the container upon its boot process, as demonstrated in Figure 4. The python flask server would function in a way similar to a remote shell, allowing the remote user to run software in their container. The web server additionally had various built-in buttons that could run pre-made shell commands for running python [7] and Julia [8] scripts, allowing for the user to develop and run code with a minimal understanding of Linux [9] [10] shell commands.

5.3 Jupyter

While the custom, Flask-server-based back end for remote computation functioned properly, it was problematically prone to errors and insecurities due to the amount of new production-level software that needed to be created from scratch. This prompted research into a new solution for remotely editing code, and accessing computational resources in a container.

Jupyter provides a powerful text editor as well as built-in functionality for python notebooks (`.ipynb` files), which have fairly recently become an important tool for data science [11] [12]. With Jupyter, it is easy for users to remotely access containers by adding a command to start a Jupyter server in the container's `Dockerfile` [13]. Using this method, when a scientist wants to edit code, they can start a Jupyter container and then clone the GitLab repository of the project that they would like to edit.

6 Software compartmentalization

6.1 Remote scientific computation

The creation of the web-based diagnostic code sharing platform prompted an additional opportunity for streamlining the efficiency of internal software development at LLE. Given that scientists are able to find software for reading data from

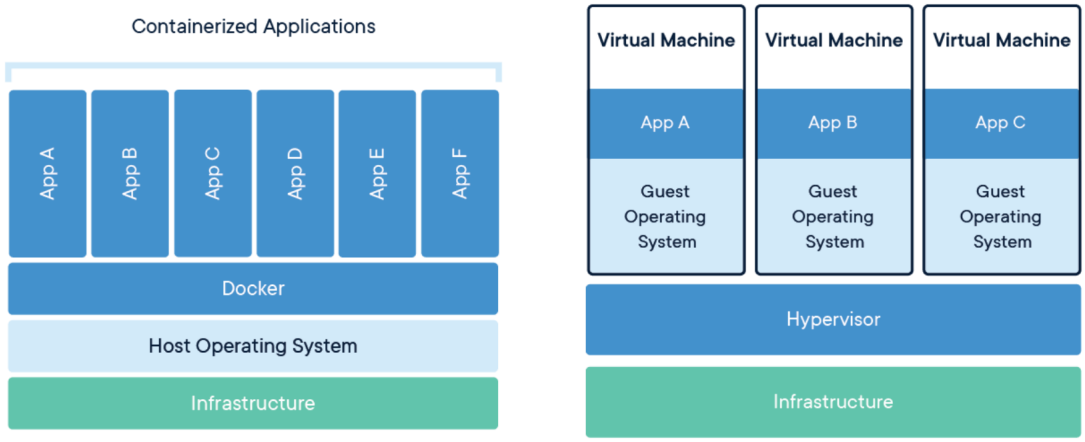

Figure 5: An intuitive visualization of containerization and virtual machines. Image sourced from [14].

diagnostics on the web platform, it is also possible that they may wish to use, modify, or further develop the software for their own personal needs, and share what they create with other scientists. This work aims to create an application management system that allows scientists to run or develop code securely and remotely.

If a scientist working on a particular project wants to use software created for another project that is stored on GitLab, such as loading diagnostic data and performing a particular analysis on it, they will need to clone the Git repository and run it locally (in this case, 'locally' means on their personal machine). They will need to install all of the dependencies of the project that they are using, and handle the issues created by conflicting software configurations on their local machine. Furthermore, if the project includes the usage of some intense scientific computation, their machine's hardware may be inadequate for its task. After all of this has been handled and the scientist has extracted the analysis data that they need, two more problems arise. Firstly, the installation of the project and its dependencies could potentially conflict with other software on the scientist's computer, and therefore have a detrimental effect on the software's ability to function properly in the future. Secondly, if the scientist wishes to return to their analysis project in the future, and use it the same way they had previously, dependencies from the project will likely have been updated, potentially causing compatibility issues, and preventing the analysis code from continuing to work properly. This is clearly a problematic system of using scientific analysis software, and this work aims to demonstrate how it can be improved through the usage of remote computing [1].

6.2 Compartmentalizing Software

Compartmentalization of software allows any given application to be run in a safe and controlled manner. One goal of this research was to find a compartmentalization tool that can be used to control the computational resources allotted to a particular application, and to easily manage the dependencies that a particular software needs so that it can be used to clone Git projects and run code from the projects.

6.3 Virtual machines

Virtual machines are operating systems that are run under the supervision of a hypervisor software. The operating systems each have an allocated portion of the physical computer's computational resources and are already commonly used for various applications [14]. This is visualized in Figure 5. While this is an attractive solution due to their powerful capabilities, virtualizing an entire operating system for the purpose of cloning a Git repository and writing code is inefficient and wasteful [1].

6.4 Containers

Containers are applications that virtualize the libraries, file system, and computational resources of an operating system, while running on a host operating system [14]. For this project, several software packages for containerization were researched.

6.4.1 Docker

Docker is an extremely popular container software for Linux. Docker utilizes a daemon, a server for developing and managing containers. Docker allows its user to create a Dockerfile, which contains set of commands that configure a container image, as well as allow for the container to run certain commands when it is spawned [14]. This was used in early versions of the back end, as the server's containers would run a python Flask server when they were spawned, allowing for the remote user to access its computational resources.

While Docker is a powerful tool, it is not supported by Red Hat Enterprise Linux (RHEL) [15], the operating system used for the server. Additionally, Docker requires root access in its operating system to develop and manage containers, which may pose a potential security risk. Because of these reasons, the decision was made to not use Docker, and look for another viable option for containerization [1].

6.4.2 Podman

Podman is a containerization software that has been created as a substitute for Docker, specifically for RHEL users. Podman does not use a central daemon server to manage and develop containers, and it does not require root privileges to be used. Furthermore, Podman's functionality is accessible by many of the same commands as Docker, and can use the same Dockerfiles that Docker uses to create container images [16].

6.5 Container and application management

While containers provide an important tool for software compartmentalization, allowing this project to function, a need was discovered for a way to manage containers, rather than simply spawning a container every time a scientist branches a Git [17] project from the web interface. It is desired that an application management system would solve the following items.

- Allow for a server administrator to manually control how many computational resources are allocated to each container. Different projects may take different levels of priority, or simply need more computational power than will be allocated to each container.
- Kill containers after they are no longer used, or when they have been left idle. There will likely arise situations when scientists accidentally leave containers on when they are no longer being used.

While Kubernetes [18] was examined to provide a solution to this, it was found that most of this functionality could be achieved through Docker and Podman alone. Additionally, for Jupyter notebooks, a software called DockerSpawner [19] was discovered and used for spawning Jupyter Notebook containers when scientists need to create a new container.

6.6 Saving containers

After a scientist has performed some sort of scientific analysis in their container, they may wish to save the file system of their container. By saving the file system of their container, they can return to their analysis code in the future, if they find themselves working on a project that requires more of the same analysis. Additionally, their container may be where they manage the Git branching and merging if their code is a contribution to a collaborative project.

A solution to this problem was not completely finished. Scientists can use Git to push their changes as a new Git repository that they own, and clone the repository when they want to use their work again. A solution for scientists to save container file systems will be explored in future work.

7 Conclusion

7.1 What has been accomplished

The purpose of this project is to demonstrate how a method of remote software collaboration can function for non open-source projects at LLE. This aims to solve many of the existing inefficiencies that exist, as well as allowing scientists from external research organizations to safely use software that has been created at LLE to analyze data that they have access to.

This project created a web interface, an indirect authentication server, and a containerized application management system to allow for users to access software they need, and run minor computational experiments in a safe and remote fashion. This proves to be advantageous, as the compartmentalized nature of containers allows for software dependencies to be easily managed remotely, thus improving the efficiency for the user.

7.2 Future Work

While this system has been demonstrated to work end-to-end, work on this project is not complete. The project has yet to be used for actual science in a practical application. The code for the server and application management must be refined to prevent insecurities that are inherently present in such a large untested project.

Future work on this project will attempt to deploy the server, and receive feedback on the server from scientists that use it. Optimistically, the web platform will become a useful tool for streamlining the efficiency of computational analysis experiments. This will allow for scientists to spend less time dealing with dependency and software compatibility issues on their local machine, so that they can focus on science.

Acknowledgments

Great thanks to the Laboratory for Laser Energetics High School Summer Research Program for allowing this research to take place. Furthermore, many thanks to Richard Kidder and Dr. R. S. Craxton for guidence during the course of this research.

References

[1] Richard Kidder. private communications.

[2] Gitlab. https://about.gitlab.com. Accessed on May 11, 2023.

[3] GitLab. Rest api. https://docs.gitlab.com/ee/api/rest/. Accessed on May 10, 2023.

[4] NodeJS. Documentation. https://nodejs.org/en/docs. Accessed on May 11, 2023.

[5] python-gitlab v3.14.0. https://python-gitlab.readthedocs.io/en/stable/. Accessed on May 11, 2023.

[6] Welcome to flask - flask documentation. https://flask.palletsprojects.com/en/2.3.x/. Accessed on May 11, 2023.

[7] Welcome to python.org. https://www.python.org. Accessed on May 11, 2023.

[8] The Julia Programming Language. https://julialang.org. Accessed on May 11, 2023.

[9] Wikipedia. Linux. https://en.wikipedia.org/wiki/Linux. Accessed on May 11, 2023.

[10] Linux. https://www.linux.org. Accessed on May 11, 2023.

[11] Jupyter. Project jupyter. https://jupyter.org. Accessed on May 11, 2023.

[12] Jupyter project documentation. https://docs.jupyter.org/en/latest/. Accessed on May 11, 2023.

[13] Docker. Minimal jupyter notebook. https://hub.docker.com/r/jupyter/minimal-notebook/. Accessed on May 11, 2023.

[14] Docker. Overview what is a container? https://docs.docker.com/get-started/. Accessd on May 10, 2023.

[15] Red Hat Enterprise Linux. https://www.redhat.com/en/technologies/linux-platforms/enterprise-linux. Accessed on May 11, 2023.

[16] What is podman? https://docs.podman.io/en/latest/. Accessed on May 11, 2023.

[17] Git. https://git-scm.com. Accessed on May 11, 2023.

[18] Kubernetes. https://kubernetes.io. Accessed on May 11, 2023.

[19] Dockerspawner. https://jupyterhub-dockerspawner.readthedocs.io/en/latest/. Accessed on May 11, 2023.

Development of a National Ignition Facility Laser Configuration with X-Ray Backlighting for Direct-Drive of a Foam Ball Target

Alisha Upal

Pittsford Sutherland High School

Pittsford, NY

Advisor: Dr. R. S. Craxton

Laboratory for Laser Energetics

University of Rochester

Rochester, New York

November 2022

Abstract

A laser configuration was developed for a National Ignition Facility (NIF) experiment that will compress an 1100 μm foam ball target. Foam ball targets are technology that may have applications in future fusion energy plants. Two quads, consisting of 4 beams each, are used for x-ray backlighting in order to obtain more extensive diagnostics on the foam ball, one quad in the upper hemisphere and one in the lower hemisphere. The backlighting quads are expected to produce an image of the target's shell which will be formed during the experiment. During compression, uniformity of a converging shock wave is necessary for a successful outcome. It was therefore essential to compensate for the backlighting beams and repoint the NIF beams in the θ (longitudinal) and φ (latitudinal) directions. The 2D hydrodynamics simulation code SAGE was used, maximizing the uniformity of the target's implosion. These simulations found velocity nonuniformity values for the shock wave as low as 1.40% RMS. The new laser pointing design is expected to be applicable to a variety of experiments that require beams to be used for backlighting.

1. Introduction

Nuclear fusion is a process that releases large amounts of energy through the combining of multiple atoms. Fusion provides a long-term, sustainable, safe energy source and is the primary objective of facilities like the National Ignition Facility (NIF). Inertial confinement fusion is one approach towards achieving nuclear fusion.[1] In inertial confinement fusion, laser beams or laser-produced x-rays irradiate a small target shell filled with fuel of two hydrogen isotopes, deuterium-tritium (DT), as illustrated in Figure 1(a). As the surface of the target reaches high temperatures, a plasma envelope is formed. This hot plasma wraps around the target. Next, in Figure 1(b) the hot shell is shown ablating outward and the internal fuel is consequently compressed from this force. The fuel reaches both extreme temperature and density, which leads to the hydrogen nuclei overcoming their repulsion forces and fusing as shown in Figure 1(c). A helium atom is formed and a neutron is released. The energy of the helium atom heats more of the compressed fuel, initiating a chain reaction and leading to "burn" where the kinetic energy of the neutron and helium atom produce a yield that is significantly larger than the input energy. This is labeled in Figure 1(d).

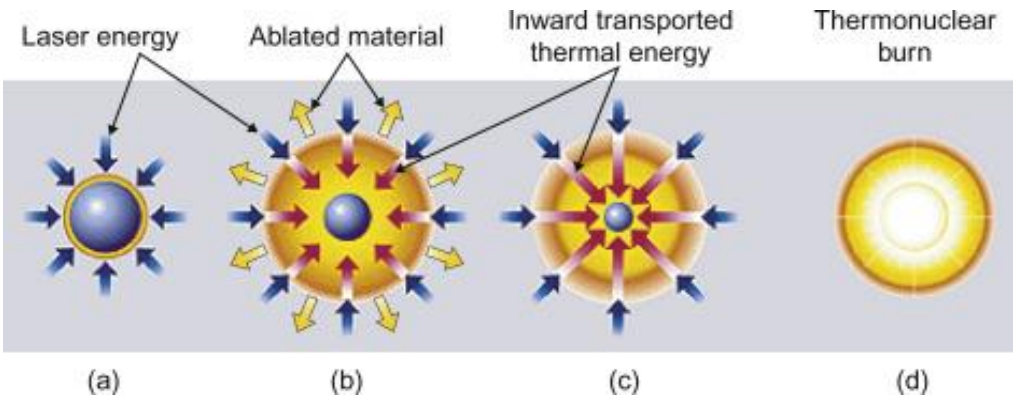

Figure 1: *Diagram of the steps in laser-driven nuclear fusion [From Ref. 1]*

The NIF and the OMEGA laser at the Laboratory of Laser Energetics (LLE) were constructed with a primary focus on two different methods for laser-driven nuclear fusion, which are indirect and direct drive respectively. For the direct drive method, shown in Figure 1, laser beams are aimed directly towards the target, also known as the capsule.[2] The laser beams irradiate the capsule at normal incidence. LLE employs the method of direct drive, which is considered more efficient than the indirect alternative. At LLE, the main laser system is called OMEGA which is an example of direct drive. OMEGA has 60 beams and provides up to 30 kJ of energy. In contrast, the NIF has 192 beams and gives up to 1.8 MJ of energy. LLE also has the OMEGA EP laser, which consists of 4 beams separate from OMEGA. It is capable of providing additional pulses to the OMEGA target chamber.

Indirect drive uses a hohlraum, typically made from gold due to its high atomic number, placed around the target.[3] This setup is shown in Figure 2. Laser beams must go through the holes at the ends of the hohlraum, and then upon impact with the walls of the hohlraum, the laser energy is converted to x-rays. It is the x-rays that then irradiate the capsule instead of the laser beams in direct drive. This method is less efficient because in the end the capsule absorbs roughly a fifth of the original energy from the laser beams. Most of the energy is absorbed by the hohlraum itself or is lost by escaping through the holes. However, the indirect drive method is prone to fewer perturbations and implosion nonuniformity issues. These issues arise from laser imperfections, thus direct drive is more sensitive to hydrodynamic instability.

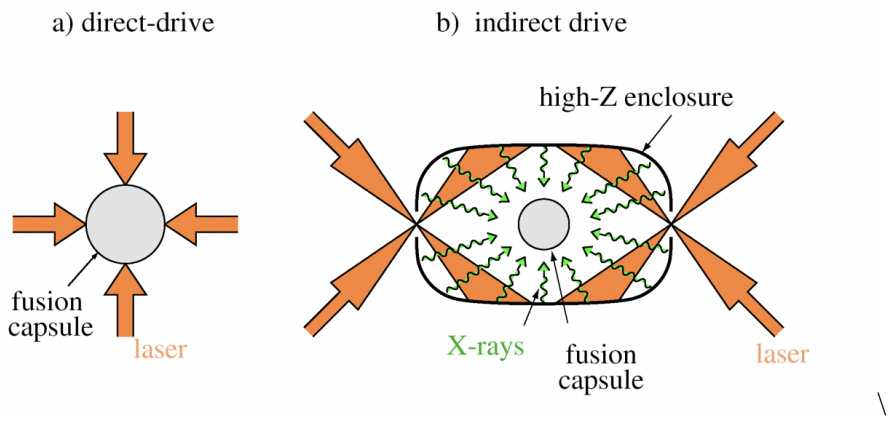

Figure 2: *A comparison between (a) direct drive and (b) indirect drive using a hohlraum, a high-Z enclosure that converts the laser energy to x-rays [From Ref. 4]*

The goal of these facilities and their projects is achieving nuclear fusion to support humanity's energy consumption. In a nuclear fusion reactor, targets would be expected to be fired at rates close to one target per second. Currently, conventional targets for direct drive are cryogenic plastic thin-shell spheres with DT ice layers inside. Producing one of these targets can take an entire day. The targets used in indirect drive have similar issues compared to the direct drive targets, regarding the inefficiency of their preparation time. The hohlraum used in the indirect drive method poses additional complications, which include requiring more preparation and depositing debris. The hohlraum material composes the majority of the mass of the target.

Alternative concepts such as the foam ball target are being explored to resolve these issues. Foam targets have an advantage of simplicity that would allow them to serve as better candidates for future fusion energy plants.[5] Instead of requiring the process to form DT ice layers, the foam ball targets only have to absorb liquid DT. Moreover, foam ball targets do not have a shell in their design. While conventional targets have pre-made plastic shells, for foam ball targets, the laser pulse forms the shell during the implosion.

This work supports a NIF experiment with the objective of investigating a foam ball target forming a shell. In the first stage of the experiment, a shock wave is launched that

converges towards the center of the foam ball. For this proposed experiment, a laser pointing configuration was developed to address the fact that the beams of the NIF are not symmetrically arranged for direct drive and that 8 beams are needed to produce diagnostics for the experiment. This means that those beams cannot contribute to pulses driving the target. The angles of the beams were adjusted and tested through the 2D hydrodynamics simulation code SAGE to optimize the configuration for uniformity. To assess the uniformity of the implosion, the shock wave radius distribution was determined based on the laser energy distribution, allowing the uniformity of the shock wave velocity to be calculated. The new design gave a low nonuniformity value of 1.40%.

2. X-Ray Backlighting in the NIF Geometry

X-ray backlighting is a technique to produce radiographic images, especially of high-density phenomena.[6] These images allow scientists to see properties of the target during compression, and can help provide insight into how to improve the target's compression. As illustrated in Figure 3, this technique has some laser beams irradiating the backlighter, which emits x-ray photons. Other laser beams are irradiating the target for implosion. The x-rays from the backlighter pass through the target and some are blocked by the high density areas.[7] The x-rays must cross through the pinhole to the detector, because the surrounding substrate is made from a high Z material and is opaque to x-rays. An absorption image of the target's shape is created.

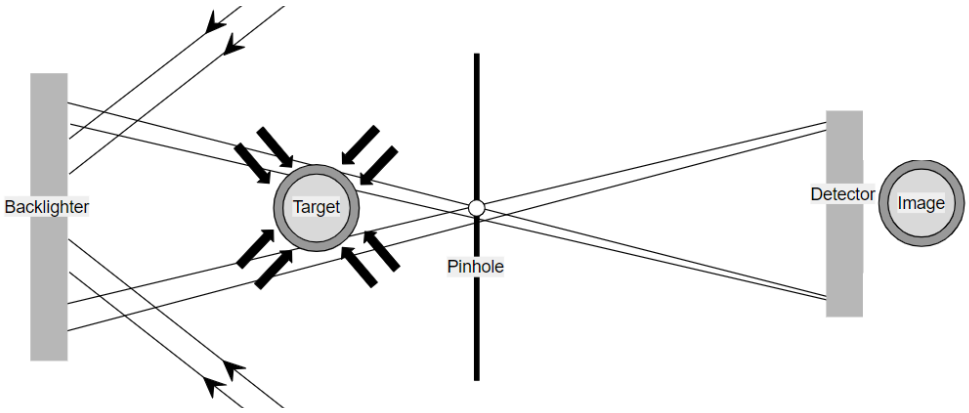

Figure 3: *Diagram of pinhole backlighting for a laser system.*

The NIF is structured with 48 quads and each quad contains 4 laser beams, summing to 192 beams overall. The structure of the NIF is shown in Figure 4 below, which is a two-dimensional projection of a spherical shell target with the laser beam configuration overlaid. The horizontal axis of Figure 2 is the vertical axis of Figure 4 since the hohlraum is oriented with its axis vertical on the NIF. In Figure 4, the beams are represented by green squares.The quads of the NIF are configured uniformly around the azimuth (φ) at angles of Θ = 23.5°, 30.0°, 44.5°, and 50.0° from the poles, with corresponding angles in the lower hemisphere. All the quads around the target chamber at one angle are considered one ring, and there are 8 rings total. The rings are numbered 1–8 from top to bottom.

Although the NIF is primarily designed for indirect drive, a direct drive method would be used in this proposed experiment for a foam ball target. However, when the NIF is used for direct drive with all the beams hitting the target at normal incidence, the equator of the target is significantly underdriven in comparison to the poles.[8] This leads to the target being imploded into an ovoid shape as opposed to a uniform sphere. To counter this, polar direct drive was developed.[9] The beams are redirected towards the equator in order to drive the equator at the same rate as the poles. This method requires a different beam configuration on the NIF from

typical direct drive. Figure 4 shows a configuration for polar direct drive on the NIF that was used for a previous backlighting experiment.[10]

In this NIF laser configuration, two quads which have eight beams total are used for backlighting. This means that these eight beams will not contribute to the target's implosion, and that the regions where the beams were aimed will have a lessened compression. This results in an implosion that is further away from the ideal uniformity. The currently used solution to this issue involves increasing the laser beam intensity for the 8 beams surrounding each backlighter quad by a factor of 50%. The aimpoint for each beam on the target is shown through a black dot. The black arrows show which beam is directed towards which aimpoint. The aimpoints of these 8 backlighting beams in each hemisphere are shifted to help compensate for the under-compressed regions.

Figure 4 shows contours of the center-of-mass radius of the imploded target after 6 ns. This is a representative time near the end of the laser pulse in the implosion experiment considered by Ref. 10, at which the center of mass radius was driven to 630 μm on average. The areas highlighted in red have a lower radius and have been compressed more while the areas highlighted in blue have a larger radius and have been compressed less. The root mean square (RMS) gives a value of the nonuniformity where the ideal would be 0%. This design has a 1.6% RMS for the center-of-mass radius, which is relatively low. The majority of the target is within 10 μm from the 630 μm mean, so the contour is $\frac{10}{630}$ or 1.6% from the mean. Over the whole sphere, the average deviation also ends up being 1.6%.

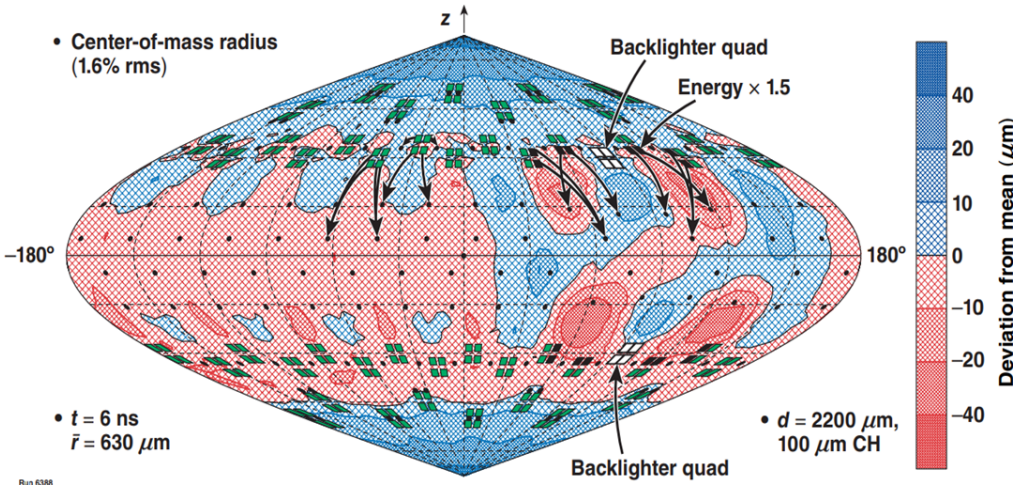

Figure 4: *Current NIF laser configuration with backlighters. The contours give deviations from the mean center of mass radius when the mean radius is 630 μm [From Ref. 10]*

However, there is a drawback to this current design. The energy of the 16 beams with increased intensity must stay below a certain limit to avoid the risk of laser system damage. As a result, the energy of the rest of the beams has to be lower than the limit by a factor of 1.5, leading to a lower overall energy compared to one without backlighting. In this work, a preferred laser configuration was developed with all the laser beams at the same intensity so this does not become an issue. To achieve this, simulations using different laser aimpoints were run and analyzed to identify a configuration that gives an optimally uniform result.

3. The Stages of a Foam Ball Implosion

For the proposed NIF experiment, a foam ball target would be used instead of the conventional target. The eventual goal is to use foam ball targets wetted with DT fuel. However, this proposed experiment is intended to first see how the concept of foam itself fares.[11] Liquid DT is absorbed into the foam, whereas conventional targets require forming a uniform solid layer of DT.[5] This also means that a shell in the foam ball must be formed after the start of laser irradiation, since it is not created in advance like conventional targets.

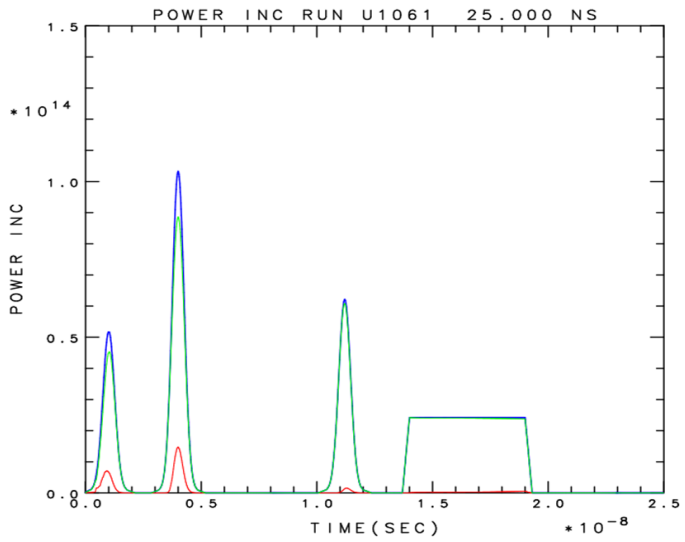

Figure 5: *Laser pulse design for proposed NIF experiment. Blue represents the amount of incident laser power; green represents the laser power absorbed by the target; red represents the laser power scattered.*

Figure 5 shows the power of the laser pulses in Watts on the y-axis with respect to time, throughout the 25 ns period. The short and intense laser pulses are known as pickets. In the figure, the blue line shows the amount of incident laser power. Of this power, most is absorbed by the target as shown by the green line and some is scattered as shown by the red line. In this experiment, only a small fraction of the laser energy is scattered and not absorbed by the target.

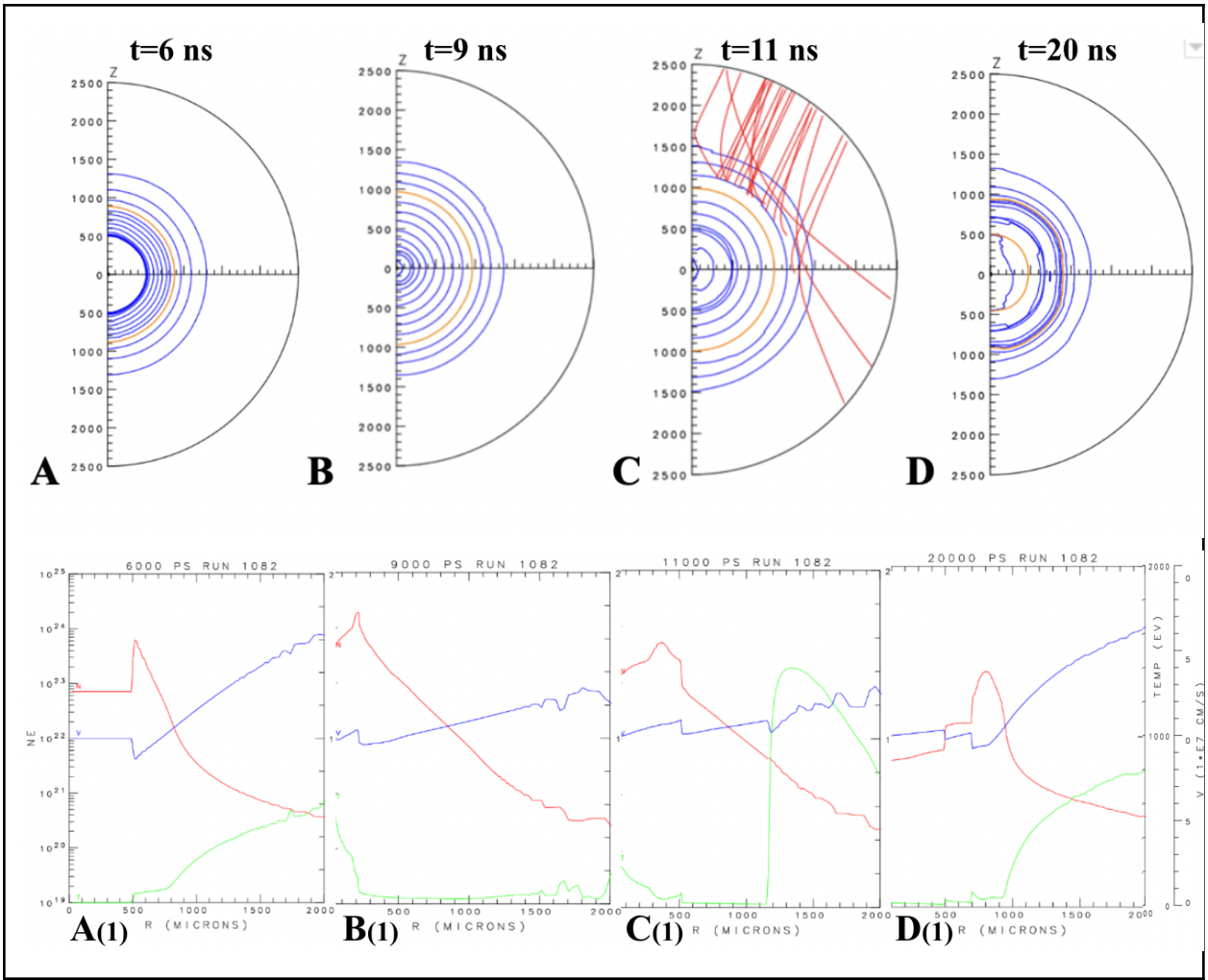

Figure 6: *A–D are density contours at selected times of the foam ball target during the proposed laser experiment; A(1)–D(1) are one-dimensional lineouts at 45° to the z-axis graphing the density in red, velocity in blue, and temperature in green throughout the depth of the foam ball target in μm at the same selected times. A: Initial compression; B: During expansion; C: Expansion stops; D: Final compression.*

The top row of Figure 6 shows density contours at different stages of the foam ball. The bottom row has lineouts of density (electrons/cc) in red, velocity (cm/s) in blue, and temperature (eV) in green. The target has a radius of 1100 μm to enable the pointing design of Ref. 10 to be used. (The pointing design depends on the target radius.) Stage A is at 6 ns, just after the first two pickets. The yellow contour line in Figure 6A–6D represents critical density, the greatest density that the laser rays can reach. Each contour line represents a factor of 2 in density. The foam deeper than the critical density line has an increased density, whereas the foam outside has

a lower density. Figure 6A shows how the shock from the laser pulses reaches about 500 μm, which is also where the jump in temperature from 0 eV to around 50 eV and spike in density are. At this point around 500 μm, Figure 6A(1) shows that the velocity is negative compared to its starting value, signifying that the target is being compressed. Inside this shock front, the foam is undisturbed.

After stage A, there is a period where the picket pulses are paused. Stage B is at 9 ns, right before the third picket. The shock has converged at the center. The velocity is positive up to 200 μm as graphed in Figure 6B(1), showing that the shock has now bounced from the center outward. The plasma in the outer part of the target continues to expand. Stage C is at 11 ns at the peak of the third picket. The target has continued to expand but its expansion is stopped by this third picket. The laser rays illustrated in Figure 6C are from a beam incident at 23.5° from the top. Rays refract along curved paths and after losing energy to 1%, the rays are no longer plotted. This occurs at half the critical density. The target absorbs close to 100% of the rays that it is hit with, as shown by the green line in Figure 5.

Stage D is at 20 ns at the end of the pulses. The foam has been compressed again by the final laser pulse and a shell is identifiable at around 750 μm. The density in the region of the shell is higher according to Figure 6D(1). This is the point at which it is most useful to take a backlighting image to determine whether a shell was successfully formed.[11] The goal of the proposed NIF experiment is to confirm and image the formation of a shell in the target. In the future, it would take additional pulses to compress that shell or attempt reaching ignition.

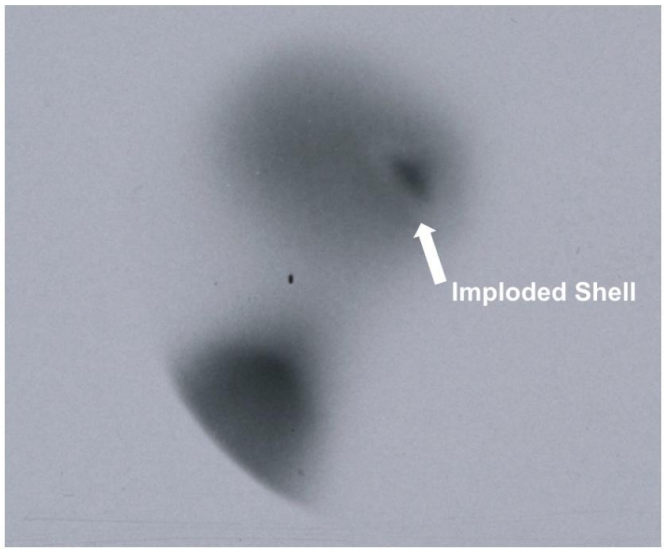

Figure 7: *Backlighting image of a foam ball implosion on OMEGA; Image credit to Dr. Christian Stoeckl and Dr. Igor Igumenshchev.*

Backlighting results for a foam ball implosion on a small scale were obtained on OMEGA in August 2022. In Figure 7, the imploded shell is visible as a slightly lighter ring around the darker part of the image. Obtaining similar results on a larger scale showing the formation of the shell is the goal of the proposed NIF experiment.

In the OMEGA experiment, the OMEGA EP laser was used as the backlighter. This meant that all the 60 beams from the OMEGA laser were able to be used for the implosion and the typical symmetrical configuration was used. However, the NIF does not have a separate laser that can be pointed to serve as a backlighter, and therefore two quads from the original NIF configuration have to be used as backlighters.

4. Beam pointing and focusing optimization

If no changes are made to the laser beam aimpoints of the NIF relative to the aimpoints with all quads present, there will be a significant decrease in laser energy deposited in the spots on the target that would have been irradiated by the backlighters. By adjusting the angular

positions of the laser aim points in the φ direction, this issue was resolved. Logically, the beams closest to the backlighters would have to be shifted more than the beams further away in order to compensate successfully.[12]

Only the laser beams in rings 4 and 5 had backlighting beams. Therefore, those were the only rings with laser beam pointings adjusted. There was natural vertical and horizontal linear symmetry present in the NIF laser beam configuration that could be used to make the optimization process more efficient. A φ angle value was assigned to a specific laser beam aimpoint in ring 4 that would then be reflected for the correlated aimpoint on the opposite side. This concept for ring 4 is illustrated in Figure 8 and matches the ring 4 quads shown in Figure 4. For example, the symmetry about quad A', the backlighting quad, was used so that the same φ6 and φ7 are used for both D and D' with their directions reversed. The φ angle values from ring 4 were also used for ring 5, but reflected going from the upper to the lower hemisphere. To find the optimal design, there are 7 parameters (φ angles 1–7) that must be adjusted. Due to the vast number of possible combinations, a systematic approach was taken, starting with evenly spaced aimpoints. Each laser pointing configuration was run through the hydrodynamics code SAGE to calculate the RMS value for the uniformity.

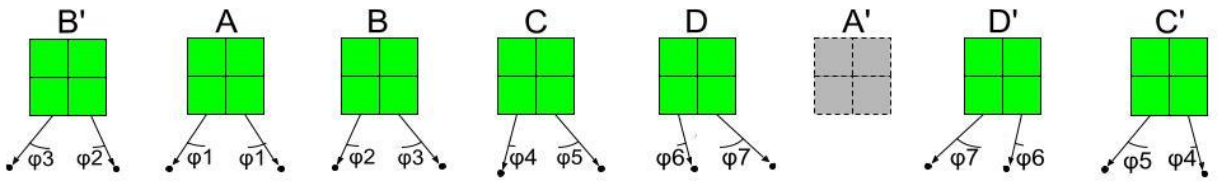

Figure 8: *Azimuthal pointing diagram of ring 4 quads, showing the symmetry of φ angles 1–7. Quad A' is used for backlighting.*

When all laser beams are in use, there are 32 beams in each of rings 4 and 5. In this design, only 28 beams from each ring are in use, and they are spread across the same 2π radians of the spherical target circumference. The new φ angles were first calculated so that each laser

aimpoint in rings 4 and 5 was equally spaced out in the φ direction, as was proposed for an earlier experiment using backlighting in Ref. 13. This meant that the aimpoints had a π/7 radian spacing between them.

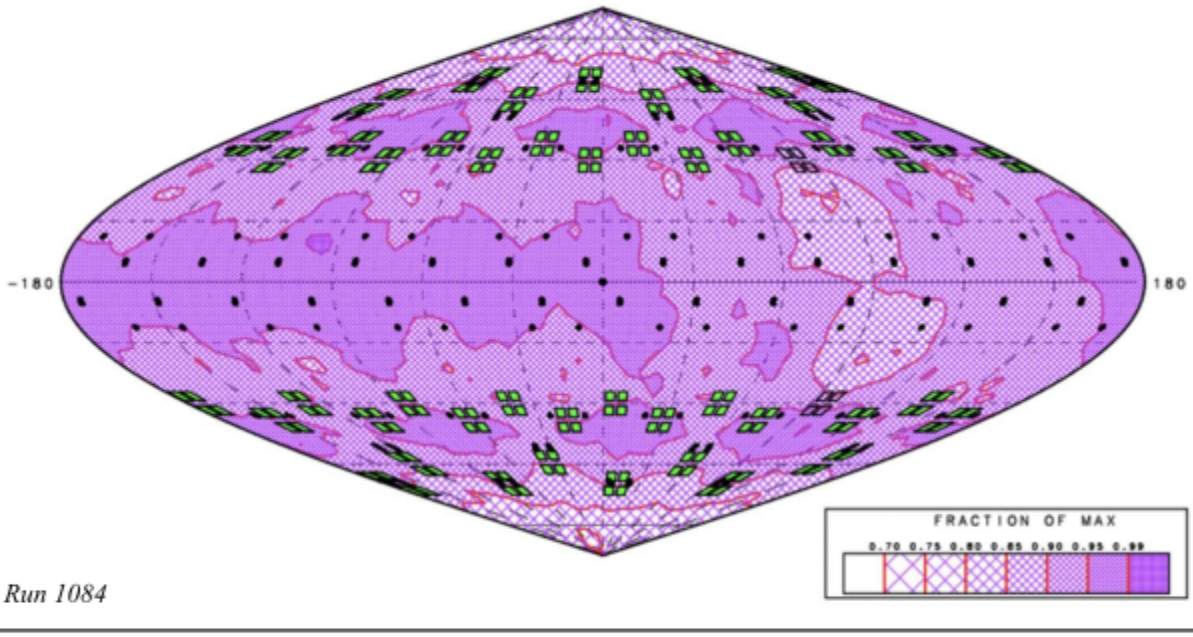

Figure 9: *Contours of deposited laser energy as a fraction of the maximum. The ring 4 aimpoints are uniform in φ with a π/7 radian spacing. The RMS is 3.93%.*

However, evenly spaced aimpoints in the φ direction did not cause an evenly distributed energy deposition in the φ direction. As shown in Figure 9, the beams that were aimed near the backlighters deposited approximately 85-90% of the energy the other beams in the same ring deposited elsewhere. The decrease in this region is because those laser beams had to shift further in the φ direction, which meant that the energy deposited from those beams was lower. These rays hit closer to the edges of the target rather than the center, leading to the target absorbing less energy. The RMS uniformity of the deposited energy for this simulation is 3.93%.

To produce a more uniform distribution of energy, combatting the weakened energy deposition in the backlighting region is necessary. Designs were investigated that had the

aimpoints in that region closer together, by increasing the other aimpoints' spacing. A range of aimpoint spacings were simulated starting from the previously tested π/7 radians up to π/6.6 radians apart. This increase in spacing kept all the aimpoints of the quads the same distance apart except for quads D and D' whose aimpoints became increasingly closer together.

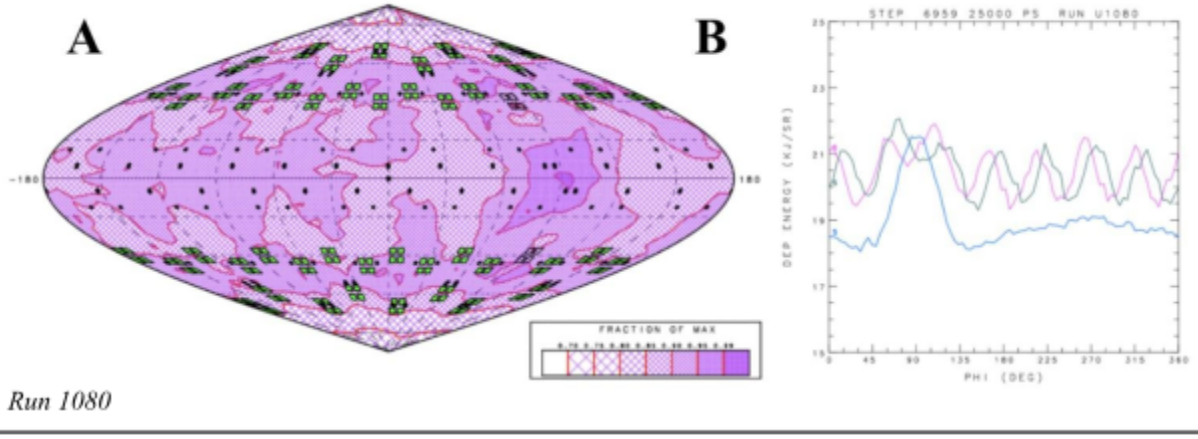

Figure 10: (A) *Target uniformity of deposited laser energy with a π/6.6 radian spacing. The horizontal dashed line above the equator is at 70° and the line below is at 110°.*
(B) *The energy deposition variance over the φ direction at specific θ angles. The green represents 110°, blue represents 90°, and pink represents 70°.*

Figure 10A shows that the backlighting region has been overcompensated at around φ = 90° in the π/6.6 radian spacing design. (In Figure 10A, φ = 0 occurs at the central meridian while in Figure 10B, φ = 0 is marked on the left side.) The two aimpoints close to the backlighting quad are close together as illustrated in Figure 10A. The uniformity variance for this pointing configuration is 3.53% RMS. Figure 10B shows the energy deposition variance for scans over φ at specific θ angles. The green represents 110°, blue represents 90°, and pink represents 70°. It is apparent that there is a spike in energy deposition around 90° in the φ direction, especially in the 90° θ lineout as shown highlighted in blue. This is approximately the location of the backlighting quads.

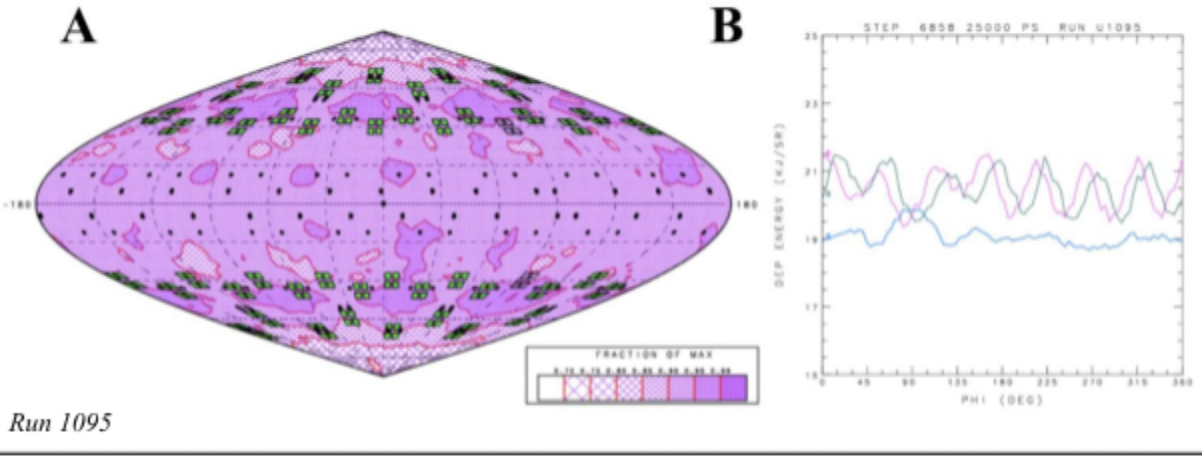

Figure 11: (A) *Target uniformity of deposited laser energy with a π/6.8 radian spacing* (B) *The energy deposition variance over the φ direction at specific θ angles. The green represents 110°, blue represents 90°, and pink represents 70°.*

Figure 11A shows a simulation run with a π/6.8 radian spacing. The energy deposition is slightly more uniform, with an RMS of 3.38%. Figure 11B shows that each θ lineout vs φ is more uniform compared to the other simulations, because there are no major dips or spikes. However, the azimuthal angle adjustments only made a small difference to improving the RMS, because the nonuniformity in the θ direction is also a contributor. As in Figure 10B, the lineout at θ = 90° has a lower average energy deposition than the lineouts at the other values of θ. This is expected as ring 4 is aimed towards the equator and there are 7 quads available rather than the 8 assumed by the previous pointing design.

Additionally, minor adjustments in the φ direction on top of the π/6.8 radian spacing were experimented with to increase the optimization. The values of φ1 – φ7 used are shown in Table 1. This adjustment produced the optimized design.

Table 1: *Aimpoint φ angles for beams in rings 4 and 5, including minor adjustments*

φ1	φ2	φ3	φ4	φ5	φ6	φ7
14.74°	3.79°	22.68°	4.35°	31.12°	8.59°	40.06°

5. Assessment of Overall Uniformity

Figure 4 used the center of mass radius to assess the overall uniformity of an imploding shell of a conventional target. However, this same concept cannot be applied to a solid such as the foam ball target. Foam ball targets do not have a clear change in density to identify the center of mass radius. Instead, the shock radius is used, as shown in Figure 6A. Identifying the shock radius can be done by finding the radius at which the temperature increases to 10 eV. This can also provide a more accurate representation of the uniformity of the target as time passes.

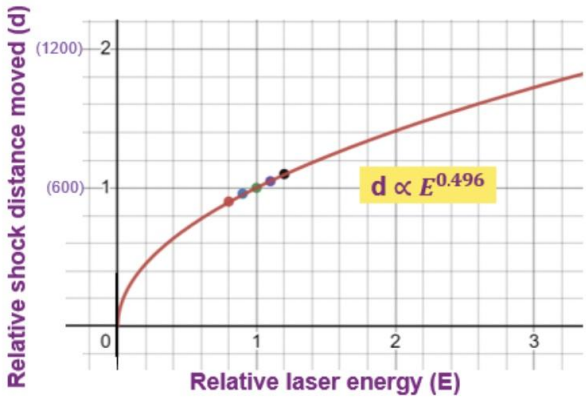

Figure 13: *The proportional relationship between shock distance moved and laser energy is graphed*

SAGE is a two-dimensional hydrodynamic code that calculates the radius and θ dependence of the implosion. However, it needs to be able to relate the deposited energy to the shock wave distance moved in order to calculate the φ dependence of the implosion. Thus, the relationship between laser energy and shock distance moved was investigated. To estimate this relationship, multiple simulations were run from 80% to 120% of the original total laser energy,

with a 10% incrementation each run. It was found that there was a scale factor of 0.496 connecting the two proportionally as shown in Figure 13. Previous work used a similar method to relate the distance moved by the imploding shell to the amount of laser energy.[14] The two were determined proportional by a scale factor of 0.72. This factor for the distance moved by the imploding shell is greater than the factor for the distance moved by the shock.

The scale factor of 0.496 was then used to create a shock wave radius plot (Figure 14) from the energy deposition distribution plot. The shock wave radius deviated 8.4 μm on average from the average 600 μm distance moved. The RMS velocity nonuniformity, the mean difference from the average velocity across the shockwave, for this plot is therefore 1.40%.

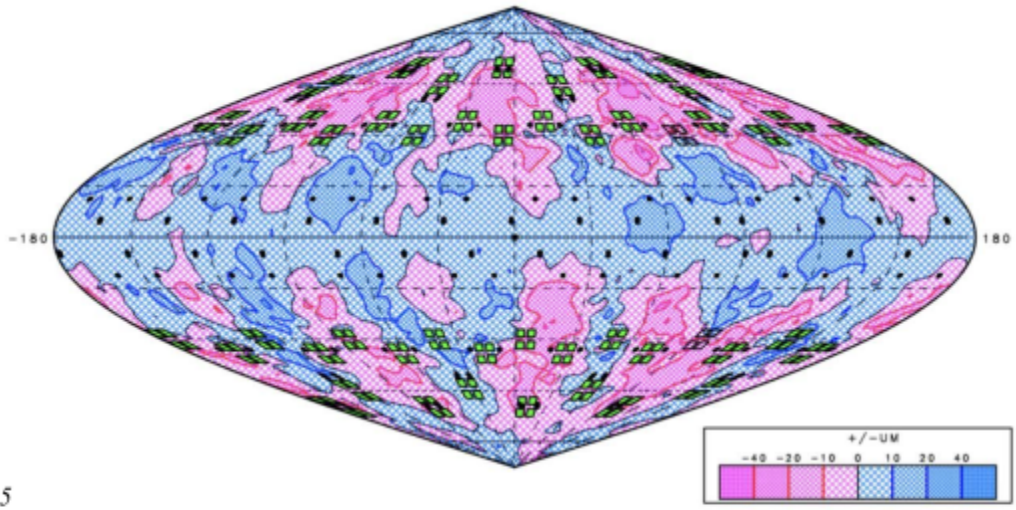

Figure 14: *Contours of deviation from the average of the shock wave radius of the optimized design at 6 ns, when the shock has moved 600 μm to an average radius of 500.5 μm. The RMS is 1.40%.*

Conclusion

This work developed an improved configuration for a proposed experiment on the NIF to irradiate a foam ball target and produce a highly uniform implosion while using two quads for backlighting. Foam ball targets have potential applications in future fusion energy plants. They

are desirable when a mass supply of targets is necessary, because the formation of the shell can occur right before implosion, rather than during the preparation of the target. Backlighting is necessary to determine the success of the shell formation during the proposed experiment on the NIF. This will allow the practicality of foam ball targets to be assessed for future experiments.

The current design for backlighting on the NIF increases the intensity and shifts the beams surrounding the backlighting quads in order to compensate. The rest of the beams are not adjusted. In the improved design developed here, all the beams are at the same intensity and the entirety of beams in rings 4 and 5 are shifted around the azimuth. The improved design has the advantage that the target can be irradiated with a 50% higher energy. Beyond foam ball target experiments, other experiments that use the current pointing design to produce backlighting images on the NIF can benefit from using this new design.

Acknowledgments

I would like to give my appreciation to my advisor and the program director, Dr. R. Stephen Craxton for helping me immensely throughout my project. I would also like to thank Dr. Igor Igumenshchev for showing me his simulations of foam ball targets. I appreciate Ms. Kim Truebger for helping the program run smoothly. Lastly, I would like to acknowledge my parents for their support.

References

1. I. Hoffman. “Review of Accelerator Driven Heavy Ion Nuclear Fusion.” Matter and Radiation at Extremes. *3*, 1 (2018).
2. J. Nuckolls, L. Wood, A. Thiessen, and G. Zimmerman. “Laser Compression of Matter to Super-High Densities: Thermonuclear (CTR) Applications.” Nature, *239,* 139 (1972).
3. J. D. Lindl. “Development of the Indirect-Drive Approach to Inertial Confinement Fusion and the Target Physics Basis for Ignition and Gain.” Phys. Plasmas, *2,* 3933 (1995).
4. *International School of Quantum Electronics 54th Course: “Atoms and Plasmas in Super-Intense Laser Fields”* http://www.emfcsc.infn.it/ef/emfcsc2013/posters2013.html (2013).
5. V.N. Goncharov, I. V. Igumenshchev, D. R. Harding, S. F. B. Morse, S. X. Hu, P. B. Radha, D. H. Froula, S. P Regan, T. C. Sangster, and E. M. Campbell. “Novel Hot-Spot Ignition Designs for Inertial Confinement Fusion with Liquid-Deuterium-Tritium Spheres.” Physical Review Letters, *125*, 065001 (2020).
6. O. L. Landen, D. R. Fraley, S. G. Glendinning, L. M. Logory, P. M. Bell, J. A. Koch, F. D. Lee, D. K. Bradley, D. H. Kalantar, C. A. Back, R. E. Turner. “X-Ray Backlighting for the National Ignition Facility.” Review of Scientific Instruments. *72,* 627 (2001).
7. R. VanDervort, M. Trantham, S. Klein, C. Sorce, P. Keiter, and R. Drake. “Development of a Backlit-Multi-Pinhole Radiography Source.” Review of Scientific Instruments. *89,* 10G110 (2018).
8. A.M Cok, R. S. Craxton, and P. W. McKenty. “Polar-drive designs for optimizing neutron yields on the NIF.” Phys. Plasmas. *15*, 083705 (2008).
9. S. Skupsky, J. A. Marozas, R. S. Craxton, R. Betti, T. J. B. Collins, J. A. Delettrez, V. N. Goncharov, P. W. McKenty, P. B. Radha, T. R. Boehly, J. P. Knauer, F. J. Marshall, D. R. Harding, J. D. Kilkenny, D. D. Meyerhofer, T. C. Sangster, and R. L. McCrory. “Polar Direct Drive on the National Ignition Facility.” Phys. Plasmas. *11,* 2763 (2004).

10. R. S. Craxton, M. Hohenberger, W. E. Kehoe, F. J. Marshall, D. T. Michel, P. B. Radha, M. J. Rosenberg. “Design of Platforms for Backlighting Spherical Implosions on OMEGA and the NIF.” 58th Annual Meeting of the American Physical Society (2016).
11. V. Goncharov, L. Ceurvorst, S. Craxton, I. V. Igumenshchev, M. Rosenberg, W. Theobald, W. Trickey. “Demonstration of High-Density Shell Formation Dynamically Starting from a Homogenous Density Ball in Support of the Dynamic Shell Ignition Concept.” Unpublished proposal (2022).
12. W. Kehoe. “Beam Pointing Optimizations for Omega Implosions.” Laboratory of Laser Energetics High School Program (2016).
13. N. S. Krasheninnikova, S. M. Finnegan, and M. J. Schmitt. “An Initial Assessment for Three-Dimensional Polar Direct Drive Capsule Asymmetries for Implosions at the National Ignition Facility.” Phys. Plasmas. *19,* 012702 (2012).
14. L. Tucker. “A Design for a Shock Ignition Experiment on the NIF Including 3-D Effects.” Laboratory of Laser Energetics High School Program (2011).

Energy Prediction on the Omega EP Laser System Using Neural Networks

David Villani

The Harley School

Advisor: Mark Guardalben

June 2023

Laboratory for Laser Energetics

University of Rochester

1. Abstract

OMEGA EP is a kilojoule-class laser system with four independently configured beams. The amplification and wavelength conversion processes are highly nonlinear, and laser performance is currently predicted using a physics-based model, *PSOPS*. An alternative neural network model was created and trained using simulated data from *PSOPS* to predict the required laser input energies for a wide range of output energies and pulse shapes. The network model predictions were within 0.05% of *PSOPS* predictions with 1000x faster processing speed. Although initial training time was 3 hours on a Graphics Processing Unit node, by implementing transfer learning the network was retrained in only 24 minutes to accurately predict a new category of pulse shapes. The network model provides a proof-of-concept for laser performance prediction using neural networks and can be implemented as an efficient, accurate replacement for certain *PSOPS* functions within OMEGA EP shot operations.

2. Introduction

2.1. The OMEGA EP System

The OMEGA EP laser at the University of Rochester Laboratory for Laser Energetics is a four-beam, kilojoule-class, frequency-tripled laser system with independent beam configuration and the ability to produce either nanosecond-scale ultraviolet (UV) pulses or picosecond-scale infrared (IR) pulses via optical parametric chirped-pulse amplification [1]. For the purposes of this paper, we are considering only the former functionality and ignoring the latter. Each beam on OMEGA EP starts with a temporally shaped pulse created by an integrated front-end system from a continuous laser with a waveform generator. This pulse is injected into front-end amplifiers before injection into the main beamline, where it is amplified by flashlamp-pumped Nd:glass in several passes through the primary beamline amplifiers, which can be configured to use a different number of amplifier discs [2]. Finally, the infrared pulse is converted via frequency tripling into an ultraviolet wavelength pulse before reaching the target. This structure is depicted in Fig. 1. Each amplification step and frequency conversion are highly nonlinear processes.

Fig. 1. A simplified diagram of the OMEGA EP laser configuration. *An integrated front-end system (IFES) provides shaped 1053-nm seed pulses from a continuous-wave fiber laser, before amplification and frequency conversion.*

2.2. PSOPS and Prediction for OMEGA EP

The ability to produce complex laser pulses is necessary for various fields of high-energy research, such as laser-driven inertial confinement fusion [3]. In such laser facilities, the ability to model, in real time, the energy of a pulse as it travels through a laser system is critical to provide flexibility and optimize operational effectiveness. OMEGA EP uses the *MATLAB*-based PSOPS model for this purpose [4,5]. This model provides accurate, flexible, real-time predictions for pulse shapes, stage energies, and beam profiles in both the forward and backward directions, and allows for real-time optimization of the model between shots using measurements of laser energy, pulse shape, and beam profile at different locations within the laser system. Figure 2 shows the process by which PSOPS predicts required IR laser energy, including the backward prediction step that is discussed in this paper. The machine-learning model discussed herein could replace the physics-based model in this step for faster backward predictions.

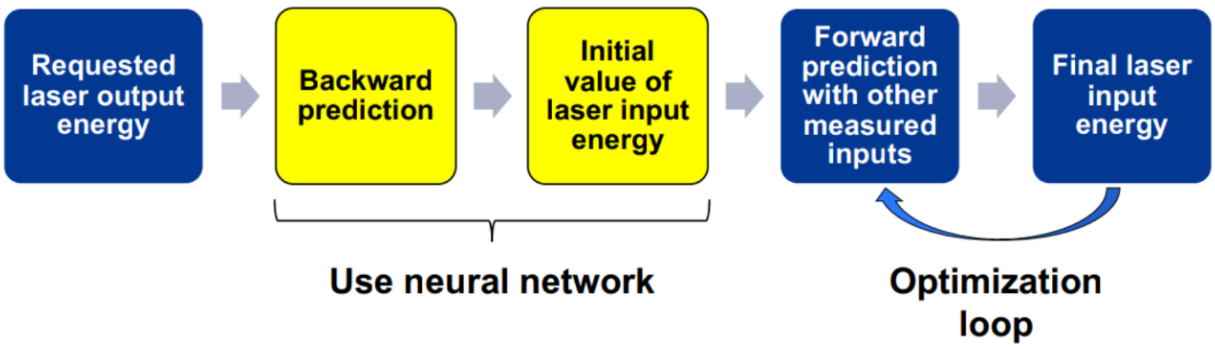

Fig. 2. A diagram of the PSOPS pulse prediction process
To configure the laser for a shot, backward prediction is used to provide an initial value of injected beamline energy for subsequent forward prediction optimization. The neural network discussed in this paper focuses on the backward prediction step, highlighted in yellow.

2.3 Artificial Neural Networks

Artificial Neural Networks, or ANNs, are connectionist optimization models capable of performing a variety of tasks efficiently. An ANN processes input data and passes the processing data through connected neurons.

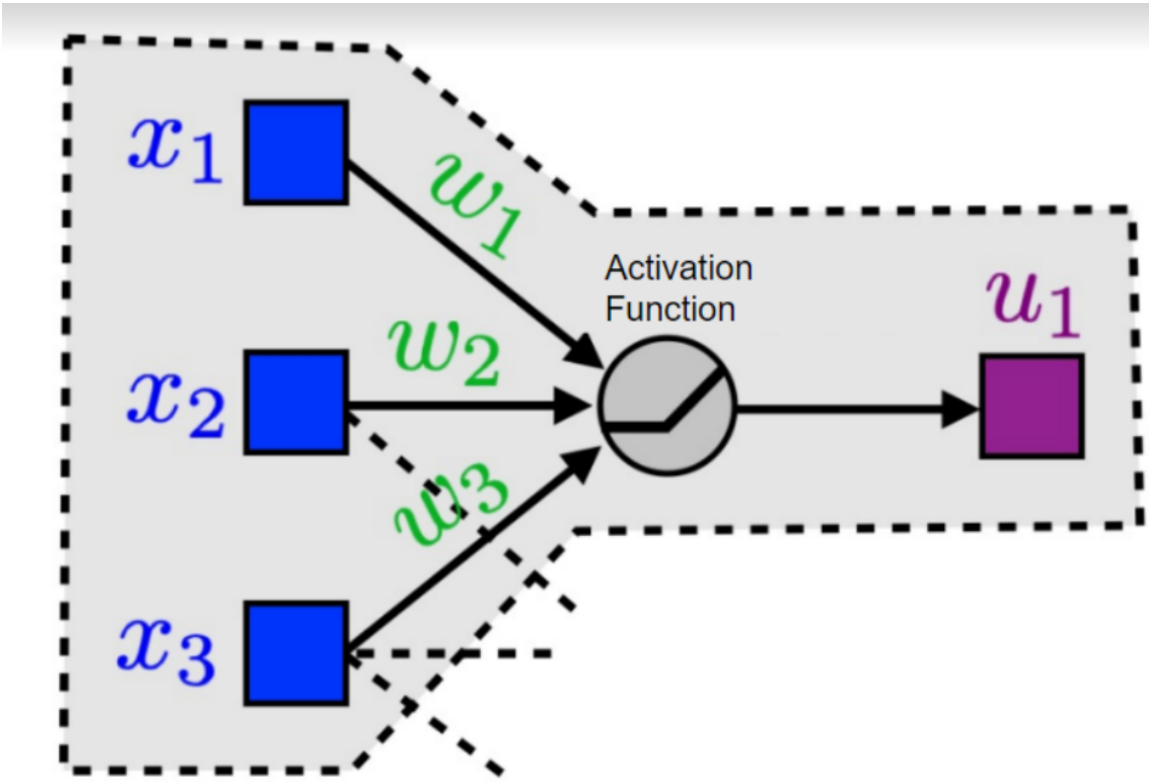

Fig. 3. An example of a neuron in an artificial neural network (based on Ref [6]).
This neuron has three inputs, x_1, x_2, and x_3, which are transformed by the linear functions w_1, w_2, and w_3, respectively. The sum of those transformed values is input into an activation function, in this case a Rectified Linear Unit (ReLU). The output, U1, is then input into the next layer of the neural network. The dotted lines represent how the same data points can also be input into other neurons, with different weights and biases, before ReLU activation.

As shown in Figure 3, each neuron applies a linear transformation (the slope of which is known as the weight and the y-intercept as the bias) followed by a nonlinear

activation function to each of its inputs.

Therefore, each neuron of a neural network is a system of equations

$$T_n = \sum_1^k (W_k x_k + B_k) \qquad (1)$$

$$u_n = f(T_n) \qquad (2)$$

where W_k is the weight, x_k is one input, B_k is a bias, T_n is the temporary sum of inputs to the activation function, and u_n is the output of a neuron.

As Fig. 4 shows, the output of each neuron in a layer can then either be collated into output data or input into another layer of neurons, creating a deep neural network. ANNs essentially manipulate and sum nonlinear components to approximate continuous functions. They have a strong ability to learn and apply nonlinear mapping and function modeling, allowing for the modeling of complex behaviors while maintaining low operational complexity due to only summing simple linear or nearly linear functions. The activation function (such as ReLU) provides the nonlinearity required to model complex functions, as otherwise the sum of a series of linear functions will always be linear.

An ANN is initialized with random weights and biases, and then optimized via backpropagation during a training process. Backpropagation is the recursive process by which a neural network is gradually optimized to ‘learn’ a data set, by calculating the error compared to a training data set, finding how to change each weight and bias to best reduce the error, and then iteratively repeating this process.

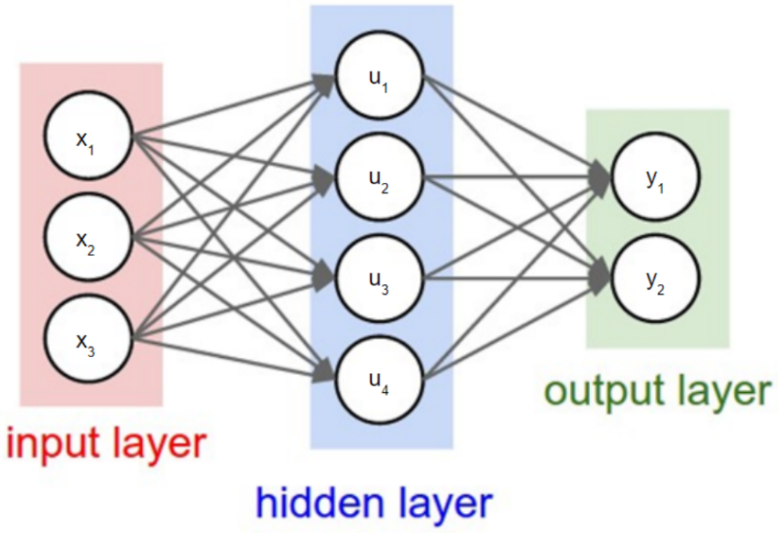

Fig. 4. A diagram of a neural network with three inputs, four hidden nodes, and two outputs.

This is a feed-forward, fully connected neural network, as each neuron in one layer is connected to every neuron in the next. More fully connected hidden layers can be added to increase computational complexity and ability.

Neural networks almost exclusively use backpropagation for optimization. During backpropagation, the Jacobian matrix (a matrix of the first-order partial derivatives of a multivariable neural network) of the ANN is calculated that contains the first derivatives of the errors in the network with respect to each weight and bias. Traditionally, for a feed-forward neural network, error is calculated as the mean squared error (MSE) of each output across the entire training data set. Algorithms such as the Levenberg-Marquardt algorithm [7] (a modified version of Newton's method) are then used to generate approximations of the Hessian matrix H (the square matrix of second-order derivatives) and gradient g of each variable of the neural network,

$$H = J^T J \qquad (3)$$

$$g = J^T e \qquad (4)$$

where J is the Jacobian matrix of the network and e is the set of vectors of network output errors relative to each weight and bias [8]. Following this, the weights and biases of the neural network, w_i, are then incremented with Newton-like updates

$$w_{k+1} = w_k - [J^T J + \mu I]^{-1} J^T e \qquad (5)$$

where μ is the learning rate (a scalar that is decreased after each successive step of the function by a ratio determined by the gradient descent function) and I is the identity matrix. The number of vectors in e equals the total amount of training data used. This process is repeated until the performance of the neural network ceases to significantly improve, as measured by the mean squared difference between the network output and the known training (or 'ground truth') data, or until another termination limit, such as a certain number of epochs of training or a minimum gradient, is reached. Other methods, such as Newton's Method gradient descent, are possible but typically approach local minima less efficiently, so Levenberg-Marquardt training was used for the model described in this paper.

3. Predictions on Simple Pulse Shapes

MATLAB was selected as the programming language and workspace for the creation of neural networks. The software already has a suite of premade machine learning algorithms and the ability to handle large-scale matrices. Initially, an ANN was developed and trained using PSOPS 'ground truth' data to predict simple ESG (EP Super Gaussian) pulse shapes. Fig. 5 shows an example of an ESG output pulse and the input pulse needed to produce it. This system used a number of inputs

describing the laser configuration and the requested UV energy and pulse shape, and the injected IR energy as the output. For the model described in this section, unlike that used in the rest of the paper, the Full Width at Half Maximum (FWHM) was used to describe the shape of the UV pulse. Prior models have used a similar system, representing shaped pulses with the FWHM [9].

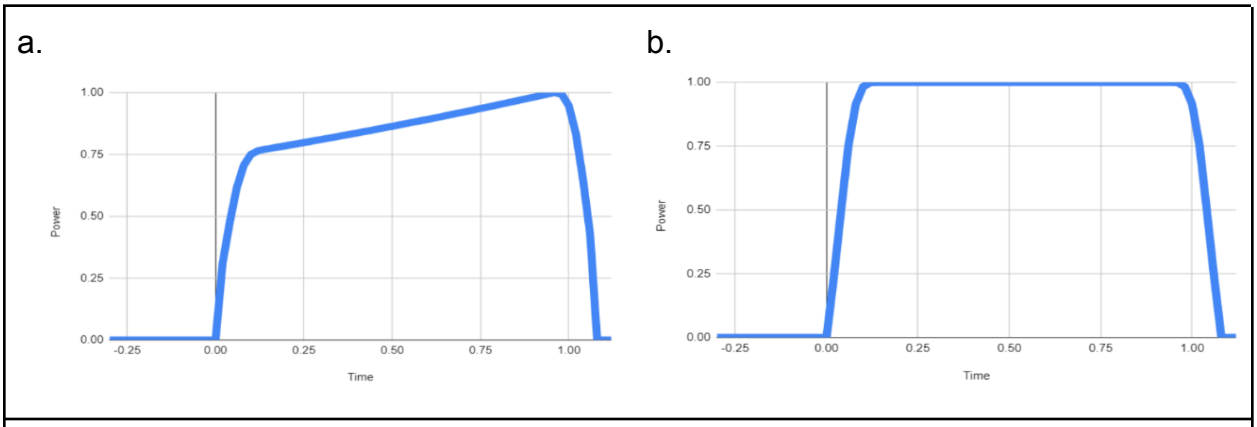

Fig. 5. *Pulse shapes as power (W) versus time (ns), with maximum normalized to 1. (a) The required IR injected pulse prior to beamline amplification to produce the ESG UV pulse shown in (b). (b) The corresponding UV pulse after beamline amplification and frequency conversion.*

This model used a structure with 4 inputs, 2 hidden fully connected layers with 10 neurons each, and a single output node. A Leaky ReLU function, which, unlike a traditional Rectified Linear Unit (ReLU), is capable of negative output, was used as an activation function, and is applied to each layer

$$f(x) = \max(x, x/10) \qquad (6)$$

which provides nonlinearity and combines computational simplicity with the ability to output negative values. The *MATLAB fitnet* function was used to create and train the function-fitting neural network.

The model performed accurately to within ±1% of PSOPS-generated ground

truth values across a broad range of ESG pulse lengths and energies. Validation and test data were randomly selected from the initial training data, with 70% of the pulses as training values, 15% as validation, and 15% as test. Validation data are used between model updates during training to prevent an ANN from overfitting by terminating training when error values for the validation data begin to increase rather than decrease. As the neural network is using training data to map to the validation data, test data that are separate from the training process are used after training to determine the quality and accuracy of the neural network. Overfitting occurs when a network adapts too precisely to noise in the training data and its ability to generalize to data it was not trained on decreases.

4. Predictions for Complex Pulse Shapes

For more complicated pulse shapes, such as the ESS (EP Stepped Square) and ERM (EP Ramp) pulses shown in Fig. 6, the FWHM was found to insufficiently sample the pulses. Thus, a new feature set to describe the input pulse shape was developed that consisted of piecewise integrals of the pulse in time. Each pulse was divided into a given number of sections, or bins, and the integral of the pulse section over its width was taken as a pulse shape feature.

Excess zeros were removed from the beginning and end of each pulse, after which the pulse was normalized to a maximum of 1 and divided into 20 concatenated pulse sections.

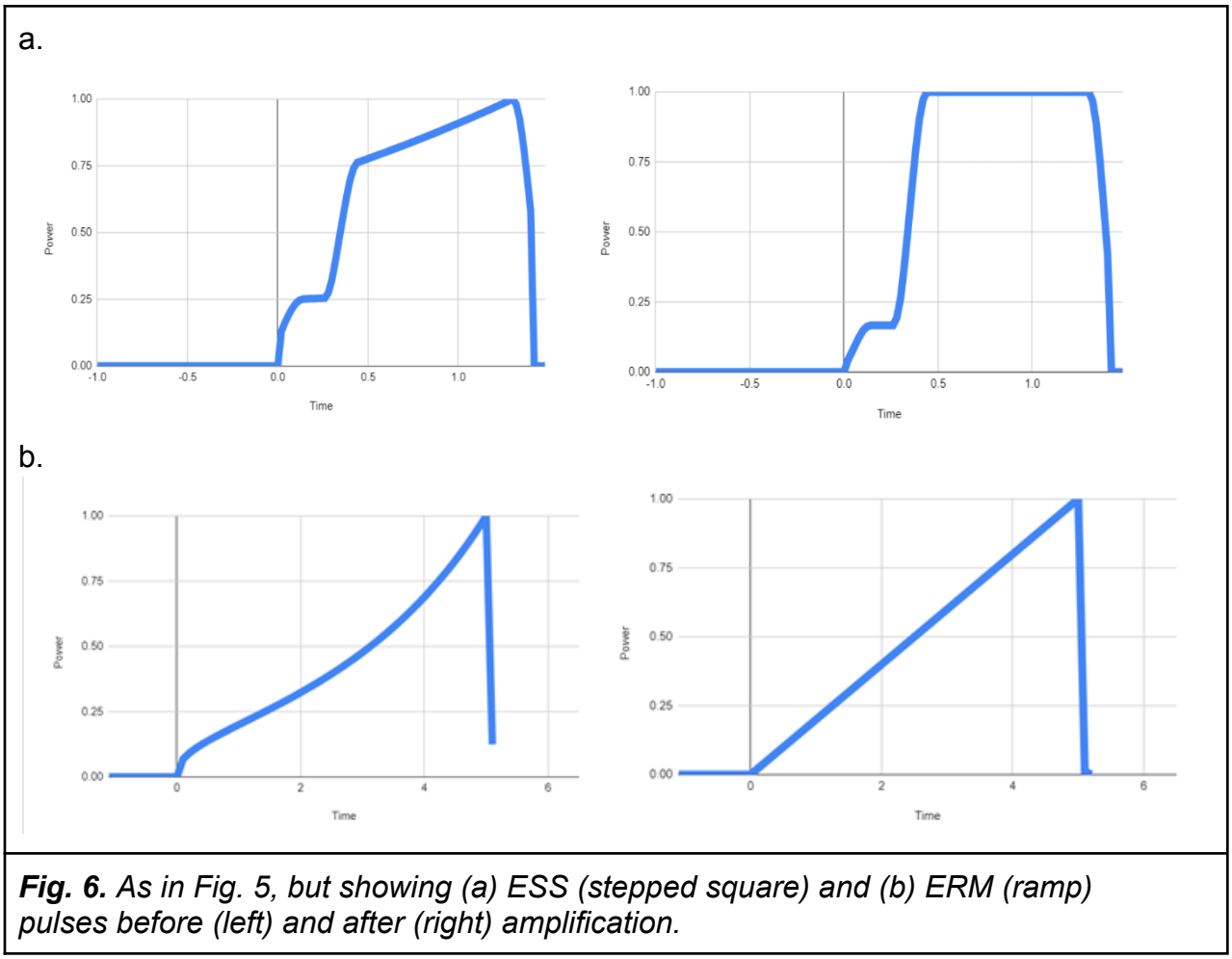

Fig. 6. *As in Fig. 5, but showing (a) ESS (stepped square) and (b) ERM (ramp) pulses before (left) and after (right) amplification.*

This number of pulse shape features was determined by balancing the model's accuracy against training time. Each section was then summed separately, resulting in 20 numerical values to be used as input features to the neural network. Additional input features included a manually input integer modifier (a discussion of which is beyond the scope of this paper), beamline number, number of active amplifier discs, and total UV energy. The output of the network is a single node, the total predicted input energy, which is returned as a scalar value. To account for the increased input complexity, the size of the neural network was increased to two hidden leaky ReLU layers with 30 neurons each. Fig. 7 shows the structure of this model.

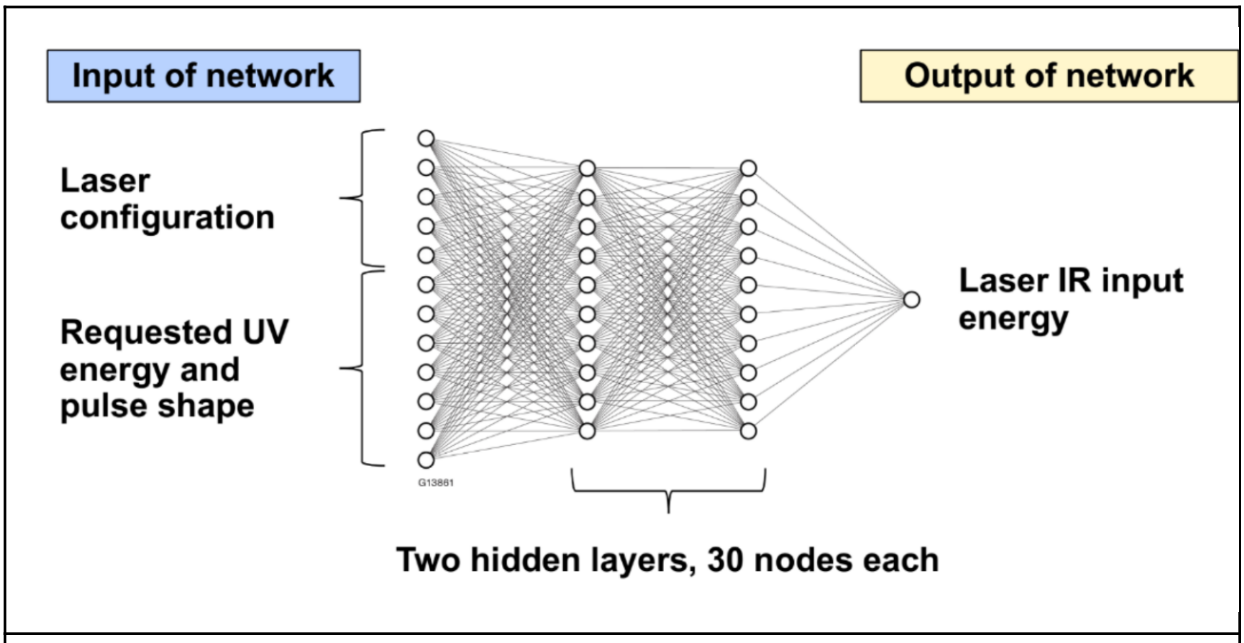

Fig. 7. A graphical depiction of the neural network used for backward prediction
Compared to the earlier, FWHM-based neural network, this model was significantly more complex, with 24 inputs and 2 hidden Leaky ReLU layers with 30 neurons.

This ANN was found to be extremely accurate when tested on ESS, ERM, and ESG pulses similar to those it had trained on, using the same randomly selected 70% training, 15% validation, and 15% test data from 16,000 PSOPS simulations. Fig. 8 shows the error distribution across the test data set, with a mean error of μ = -2.77*10^{-5}% (defined as the average of the difference between true and predicted data, and used here as a measure of skew), and a standard deviation σ=1.2*10^{-3}%.

There is an increased percentage error for low injected energy values. This is due to the ANN training to minimize mean squared error (MSE), which incentivizes reducing percent error in higher energy pulses. This could be avoided by backpropagating in a manner that minimizes the mean squared percentage error rather than MSE.

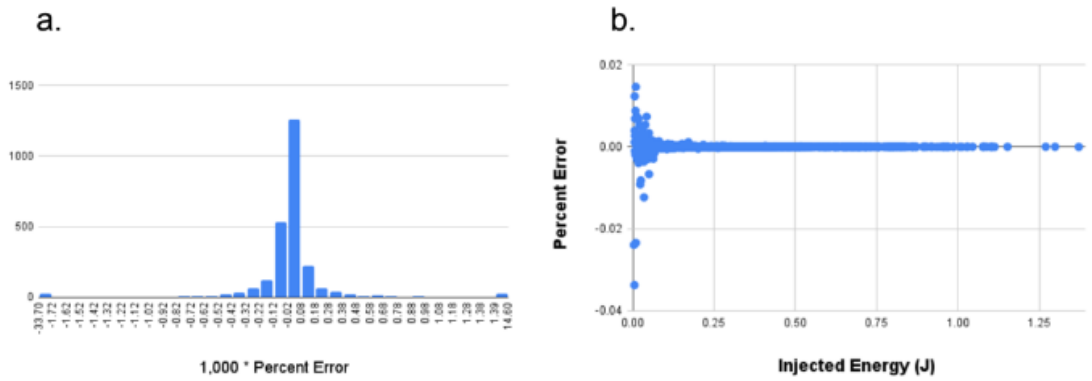

Fig. 8. Visual representations of errors in ANN predictions.
(a) A histogram of prediction percent error for the test data set. There is no significant skew in either the positive or negative direction. (b) A graph showing percent error versus injected energy (in Joules). Notably, low-energy pulses have a significantly greater percent error, as described in the text.

5. Processing Speed and Transfer Learning

Training and predictions were run on a GPU node at the University of Rochester's Laboratory for Laser Energetics Computing Facility with the Storm High Performance Computing system. The average training time across several models was approximately 3 hours, and prediction time on test data was an average of 5.4 ms. The current PSOPS system has an average prediction time of 4-6 seconds, marking a nearly thousandfold increase in prediction speed for the ANN.

Transfer learning is the process by which a pre-trained neural network is retrained with new data in order to decrease the amount of computation required to predict new types of data. The ANN can be retrained easily to incorporate new data with a high degree of accuracy, providing high agility.

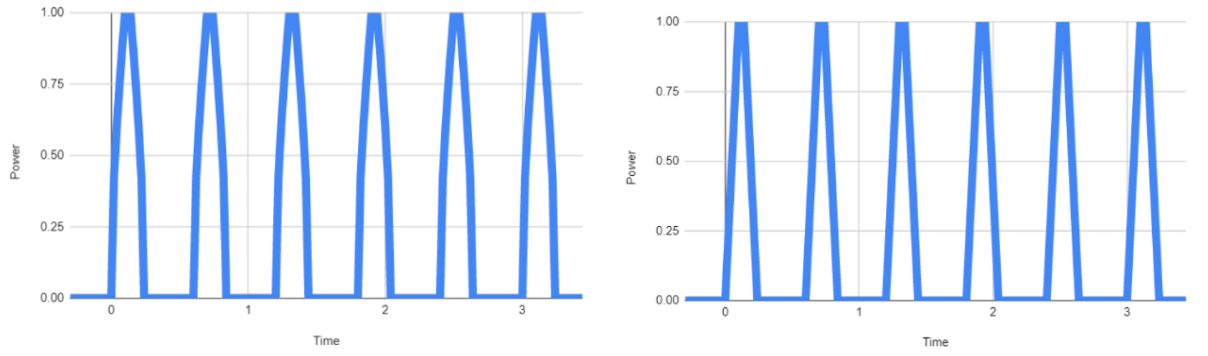

Fig. 9. *As in Fig. 5 but showing the normalized shapes of picket (EPM) pulses before and after amplification and frequency conversion.*

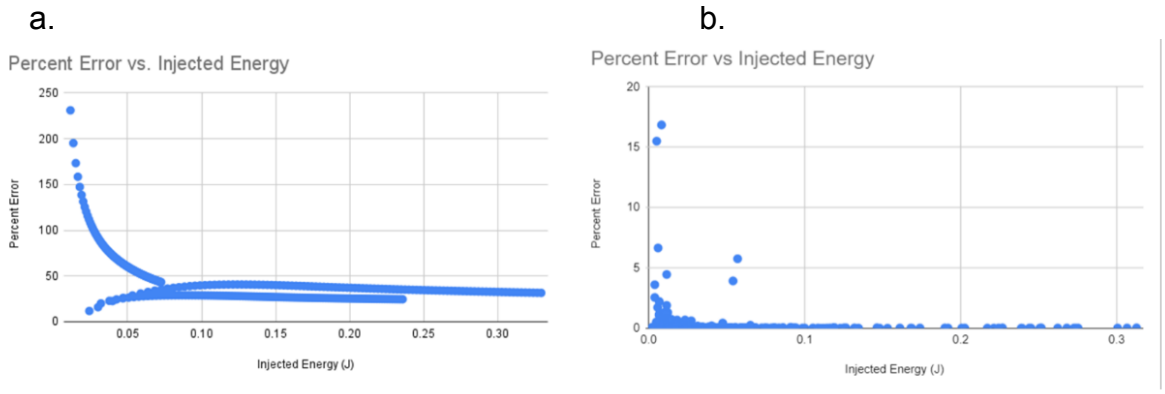

Fig. 10. Percent error versus injected energy for picket pulses before and after retraining.
(a) All provided picket pulses were input into the ANN without retraining, leading to substantial errors. (b) After retraining with 70% of the picket pulses, the randomly selected test data set has significantly less error across the range of injected energies.

A new and dramatically different type of pulse, picket pulses (EPM), as shown in fig. 9, were input into the ANN without retraining. Fig. 10 shows the error before and after retraining the neural network for picket pulses. A comparatively small number of new pulses (300 as opposed to 16,000) were used for retraining, leading to decreased accuracy compared to previous training.

The retraining of the neural network started with the already-trained network, on both the picket pulses and the previous pulse shapes. The ANN took an average of 00:24:13 to retrain for picket pulses, and maintained high accuracy predictions on ESS, ESG, and ERM pulse profiles. No significant change was observed in single pulse prediction time. This transfer learning would likely improve retraining time compared to the initial 3-hour training even with more picket pulse values, as the majority of the computational intensity is due to maintaining accuracy on the larger amount of previous (non-picket) data.

6. Conclusion

A fully connected, feed-forward neural network model was created and used to predict the required OMEGA EP IR input energy for a given UV output energy, laser pulse shape, and laser configuration. The difference between predicted energies using the ANN and the physics-based PSOPS model was less than 0.05%, and energy prediction using the neural network was approximately 1000 times faster than the physics-based model. Accurate prediction was achieved across a broad range of laser pulse shapes and output energies. Furthermore, transfer learning was found to reduce training time for new pulse shapes by 88%. The prediction accuracy and speed of the ANN model demonstrates the viability and potential advantage of using neural networks for laser performance prediction.

ANNs have several other advantages. The ANN discussed here was trained with noiseless, predicted data, but a neural network can be trained on actual pulses

and can account for several variables, such as humidity, that are difficult to predict with high-energy physics models. On the other hand, it is challenging to maintain the calibration of the model, and retraining might be required to account for changes in the laser system over time. Further research is needed to determine the viability of ANNs with greater predictive capability, for example forward energy calculations and pulse shape predictions, as well as neural networks trained on raw data as opposed to simulated noiseless data. With more diagnostic information and further development, such models could replace the current physics-based predictive models with neural networks that could considerably increase the operational efficiency of the laser system.

7. Acknowledgements

I would like to thank those who assisted with the completion of my project. First, I thank Dr. Craxton for giving me and the other interns in the LLE summer internship program the opportunity to work in a research environment. I would also like to thank my fellow student interns in the Annex Conference Room. Their dedication and hard work created an environment that supported each of us in our various projects, as well as making the summer much more enjoyable. Finally, I give special thanks to my advisor, Mark Guardalben, for the amount of time and effort he has devoted to my project, none of which would have been possible without his guidance. I am extremely grateful for his efforts and advice.

References

1. L. Waxer, J. Kelly et al. "The OMEGA EP High-Energy, Short-Pulse Laser System," in Frontiers in Optics 2008/Laser Science XXIV/Plasmonics and Metamaterials/Optical Fabrication and Testing, OSA Technical Digest (CD) (Optica Publishing Group, 2008), paper FWQ2.
2. J. Kelly, R. Jungquist et al., "Optical Engineering of the OMEGA EP Laser System," in Frontiers in Optics 2008/Laser Science XXIV/Plasmonics and Metamaterials/Optical Fabrication and Testing, OSA Technical Digest (CD) (Optica Publishing Group, 2008), paper OFB2.
3. D. Cao, T. R. Boehly, M. C. Gregor, D. N. Polsin, A. K. Davis, P. B. Radha, S. P. Regan, and V. N. Goncharov, “Theoretical quantification of shock-timing sensitivities for direct-drive inertial confinement fusion implosions on OMEGA,” *Physics of Plasmas*, vol 25, 052705 (2018)
4. MATLAB®R2013b, The MathWorks Inc., Natick, MA 01760-2098 (http://www.mathworks.com)
5. M. Guardalben, M. Barczys, B. Kruschwitz, M. Spilatro, L. Waxer, & E. Hill, “Laser-system model for enhanced operational performance and flexibility on OMEGA EP,” *High Power Laser Science and Engineering, 8*, E8. doi:10.1017/hpl.2020.6 (2020)
6. G. Peyré (2020) “Mathematics of Neural Networks,” unpublished manuscript. Retrieved from https://mathematical-tours.github.io/book-basics-sources/neural-networks-en/NeuralNetworksEN.pdf
7. J.J. Moré (1978). “The Levenberg-Marquardt algorithm: Implementation and theory.” In: Watson, G.A. (eds) Numerical Analysis. Lecture Notes in Mathematics, vol 630. Springer, Berlin, Heidelberg. https://doi.org/10.1007/BFb0067700
8. M.T. Hagan, and M. Menhaj, “Training feed-forward networks with the Marquardt algorithm,” *IEEE Transactions on Neural Networks*, Vol. 5, No. 6, 1999, pp. 989–993, 1994.
9. L. Zou, Y. Geng, G. Liu, L. Liu, F. Chen, B. Liu, D. Hu, W. Zhou, and Z. Peng, "Laser energy prediction with ensemble neural networks for high-power laser facility," Opt. Express 30, 4046-4057 (2022).

Measurement of the refractive indices of KDP and ADP at low temperatures

Grace Wu

Pittsford Mendon High School

Pittsford, NY

Advisor: Ildar Begishev

Laboratory for Laser Energetics

University of Rochester

Rochester, NY

April 2023

1 Abstract

Potassium dihydrogen phosphate (KDP) and ammonium dihydrogen phosphate (ADP) are nonlinear optical crystals used to convert radiation of high-power, large-aperture infrared lasers into the deep-ultraviolet range. The current temperature-dependent Sellmeier equations for both KDP and ADP don't correspond to experimental data at low temperatures. In this work the refractive indices of KDP and ADP were measured at different temperatures to allow the equations to be modified. Initially, the refractive indices of both crystals were measured at room temperature and checked by comparison with existing values. Prisms from KDP and ADP crystals were then placed inside a two-chamber cryostat, and two laser beams of different wavelengths (633 nm and 533 nm) were aligned to the prisms. Liquid nitrogen was pumped into the cryostat, cooling the crystals down from approximately 300 K to 200 K. The refractive indices were measured for ordinary and extraordinary beams based on the positions of the refracted beams as the temperature changed. The experimental data were fitted to new equations, which were then compared with the original equations.

2 Introduction

Nonlinear crystals are often used in lasers and electro-optical applications, including the OMEGA [1] and OMEGA EP [2] lasers at the Laboratory for Laser Energetics of the University of Rochester. Currently, the most powerful lasers emit light in the infrared range. However, many applications, such as high-density plasma diagnostics [3], require high-energy deep ultraviolet (UV) sources. Unfortunately, only a few lasers can generate UV light directly. They either cannot provide sufficiently energetic beams in the UV region, or they are too complicated (excimer laser) [4]. Methods of nonlinear optics can be utilized to convert infrared light into UV. Particularly, the

fifth-harmonic generation (FHG) of large-aperture neodymium lasers in ADP and KDP can provide beams with high UV energies due to the availability of large ADP and KDP crystals. Harmonics are laser beams with a frequency that is n-times higher than the fundamental (initial) laser frequency of ω, where n is an integer and ω is the circular frequency of the light. The simplest example is second harmonic generation (SHG), where two photons at the fundamental ω generate one photon of second harmonic with frequency 2ω: $\omega + \omega = 2\omega$.

Another type of nonlinear process is frequency mixing. For example, the third harmonic generation (THG) process $\omega + 2\omega = 3\omega$ provides photons of the third harmonic from photons of the second harmonic, 2ω, and residual photons of fundamental frequency ω left after SHG. THG is used on all 60 beams of the OMEGA laser to convert radiation with a wavelength of 1054 nm into UV light with a wavelength of 351 nm. The fourth harmonic generation can be generated in a cascade of two SHG processes. Finally, the FHG can be realized in a cascade of three processes:

$$\omega + \omega = 2\omega \;>\; 2\omega + 2\omega = 4\omega \;>\; \omega + 4\omega = 5\omega$$

To convert light of one wavelength into another, it is necessary to match their phase velocity in a crystal. Nonlinear crystals can achieve this because of the birefringence effect, which can split light into two different beams inside the crystals, the ordinary and extraordinary. At orthogonal polarizations, these beams can have the same refractive index and therefore the same phase velocity for different wavelengths. This process is called phase matching and can only be achieved in a certain beam direction inside a crystal. Since the angular acceptance range for the direction is very small, it could be called critical angular phase matching. Thus, we can generate the second harmonic $\omega + \omega = 2\omega$, where ω is the ordinary beam and 2ω is the extraordinary beam. Both beams have the same refractive index, but in orthogonal polarizations. As a result, we can

efficiently convert 1054 nm light into 527 nm light. Second, in a similar process in a cascade, we can generate the fourth harmonic: $2\omega + 2\omega = 4\omega$, with the resulting wavelength at 264 nm. To generate light at 211 nm, we must realize the $\omega + 4\omega = 5\omega$ process. This can be written in vector form as

$$k_1{}^o + k_4{}^o = k_5{}^e$$

where $k_i{}^{o,e} = \frac{2\pi}{\lambda_i} n^{o,e}$ are the wave vectors for different harmonics i and ordinary (o) or extraordinary (e) beams with λ_i the vacuum wavelength of harmonic i.

Interaction beams can be non-collinear. In our case of FHG, all beams are collinear. The phase matching for FHG can be realized when

$$\Delta k = k_5{}^e - k_1{}^o - k_4{}^o = 0 \quad (1)$$

This can't be achieved at room temperature in ADP and KDP, but we can tune the refractive indices of these crystals by changing the temperature and reaching the phase matching condition (1). Moreover, when the angle between the direction of beam propagation in a crystal and the z-axis of a crystal is close to 90°, the angle tolerance is less tight. In this case, the phase matching (1) is said to be noncritical.

Noncritical phase matching for ($\omega + 4\omega$) was achieved by cooling an ADP or KDP large-aperture crystal in a two-chamber cryostat [5] below 200 K. While the total conversion efficiency from the fundamental to the fifth harmonic at 211 nm was 26% using ADP [5], there was a significant discrepancy between the calculated (230 K) and experimentally measured (200 K) temperatures of noncritical phase matching. This likely comes from incorrect refractive indices *n*

of crystals at low temperatures. Currently, there are not many available *n* measurements at low temperatures, so it is necessary to accurately measure *n* of ADP and KDP crystals at low temperatures.

As a result of the birefringence of KDP and ADP, double refraction occurs when a beam is put through the crystal a certain way. If there are two polarizations coming into a nonlinear crystal, the horizontal and vertical, the beam is split into the ordinary and extraordinary beams. These beams propagate with different angles because they have different velocities in the material, as shown in Figure 1.

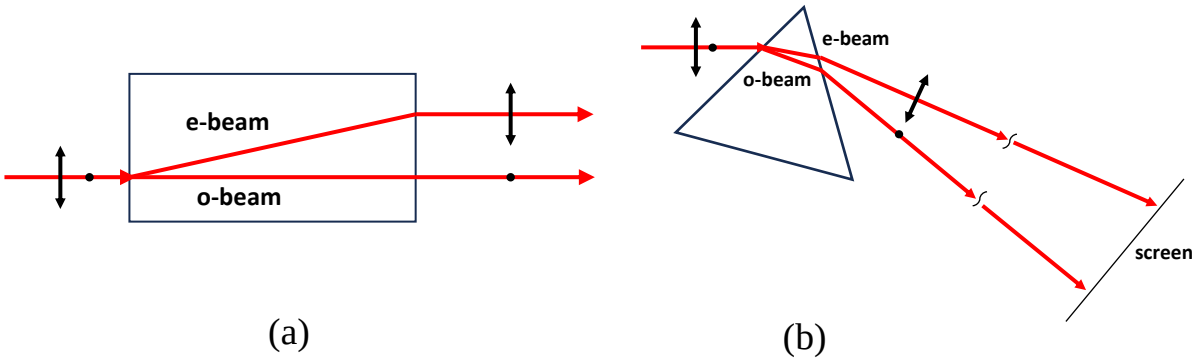

Figure 1: Ordinary (o) and extraordinary (e) beams for rectangular and triangular prisms. Figure 1a shows a rectangular prism, and the two beams come out parallel to each other, but with the e-beam displaced sideways. Figure 1b shows a triangular prism, and the two beams diverge at an angle. The screen allows the position of the refracted beams to be tracked and measured.

Temperature-dependent Sellmeier equations (2) relate refractive index to temperature and wavelength for KDP and ADP [6]. Based on the original temperature-dependent Sellmeier equations, we calculated the temperature when non-critical phase matching of the $\omega + 4\omega = 5\omega$ process should occur. However, it was different from the experimentally measured

temperature. Since Equations (2) don't match experimental data at low temperatures, they need to be modified.

KDP:

$$n_o{}^2 = (1.44896 + 3.185 * 10^{-5}T) + \frac{(0.84181 - 1.4114 * 10^{-4}T) * \lambda^2}{\lambda^2 - (0.0128 - 2.13 * 10^{-7}T)} + \frac{(0.90793 + 5.75 * 10^{-8}T) * \lambda^2}{\lambda^2 - 30}$$

$$n_e{}^2 = (1.42691 - 1.152 * 10^{-5}T) + \frac{(0.72722 - 6.139 * 10^{-5}T) * \lambda^2}{\lambda^2 - (0.01213 + 3.104 * 10^{-7}T)} + \frac{(0.22543 - 1.98 * 10^{-7}T) * \lambda^2}{\lambda^2 - 30}$$

(2)

ADP:

$$\mathrm{n_o}{}^2 = (1.6996 - 8.7835 * 10^{-4}\mathrm{T}) + \frac{(0.64955 + 7.2007 * 10^{-4}\mathrm{T}) * \lambda^2}{\lambda^2 - (0.01723 - 1.40526 * 10^{-5}\mathrm{T})} + \frac{(1.10624 - 1.179 * 10^{-4}\mathrm{T}) * \lambda^2}{\lambda^2 - 30}$$

$$n_e{}^2 = (1.6996 - 8.7835 * 10^{-4}T) + \frac{(0.64955 + 7.2007 * 10^{-4}T) * \lambda^2}{\lambda^2 - (0.01723 - 1.40526 * 10^{-5}T)} + \frac{(1.10624 - 1.179 * 10^{-4}T) * \lambda^2}{\lambda^2 - 30}$$

where T is the temperature in K and λ is wavelength in μm.

In this work, two prisms of ADP and KDP were fabricated. An automated system for continuous filling of the existing two-chamber cryostat [5] by liquid nitrogen was designed and built. The refractive indices were checked at room temperature first. Then, the crystalline prisms were moved into a cryostat where the temperature could be lowered using a liquid nitrogen system. The refractive indices of KDP and ADP were measured using the deviation of the ordinary and extraordinary beams.

3 Experimental Setup

3.1 Room Temperature Testbed

In a rectangular crystal, the ordinary and extraordinary beams come out of the crystal parallel and close to each other, as shown in Figure 1a. To better differentiate between the two refracted beams, the crystals were cut into triangular prisms, as shown in Figure 1b. Using a rotating stage, the tip angles of both prisms were measured. This is the angle p between the input and output surfaces of the prisms (see Fig. 2). The KDP prism has an angle of 46.33° and the ADP prism has an angle of 43.98°.

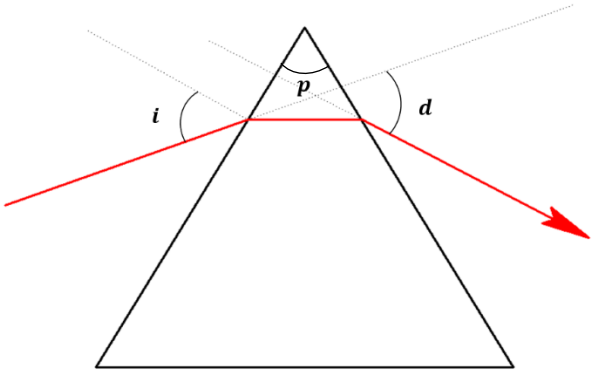

Figure 2: Diagram showing a beam refracting through a prism. The angle of deviation d can be determined from the incidence angle i, the prism angle p, and the refractive index of the crystal.

To begin, measurements were made at room temperature to ensure that the measurements matched with the existing values for the refractive indices of KDP and ADP. For this experiment, a testbed was assembled at room temperature. A red helium-neon (He-Ne) laser and a green semiconductor laser were used to measure the refractive indices at these two different wavelengths of light. Using a spectrophotometer, the red laser was determined to have a wavelength of 633 nm and the green laser to have a wavelength of 533 nm. The beams were put through the prisms at an incidence angle of 8° for ADP and 12° for KDP. The angle of deviation (see Fig. 2), which is how

much a beam changes as it goes through the prism, was measured for KDP and ADP at room temperature. The angles for ADP were measured to be 31.21°, 36.27°, 31.46°, and 36.94° for the extraordinary red beam, ordinary red beam, extraordinary green beam, and ordinary green beam, respectively. Similarly, the angles for KDP were measured to be 35.40°, 43.45°, 35.30°, and 43.22° for the extraordinary red beam, ordinary red beam, extraordinary green beam, and ordinary green beam, respectively. The theoretical values were determined by

$$d = sin^{-1}\left[n\, sin(p - \sin^{-1}(\frac{\sin i}{n}))\right] + i - p \quad (3)$$

where d is the angle of deviation, i is the angle of incidence, n is the refractive index, and p is the angle of the prism.

Using the diagram in Figure 2, Equation (3) was derived using Snell's law and geometry. Snell's Law states that $n_1 \sin\theta_1 = n_2 \sin\theta_2$, where n_1 and θ_1 are the refractive index and incident angle of the first material, respectively, and n_2 and θ_2 are the refractive index and refracted angle of the second material, respectively. Experimental values for ADP were compared to the theoretical angles of deviation at room temperature, which are 31.12°, 36.26°, 31.55°, and 37.00°, respectively. The theoretical values for KDP are 35.45°, 43.42°, 35.99°, and 45.02°. Since the theoretical and experimental values for the angle of deviation closely matched for both prisms, the next step was making the measurements at low temperatures.

3.2 Two-Chamber Cryostat

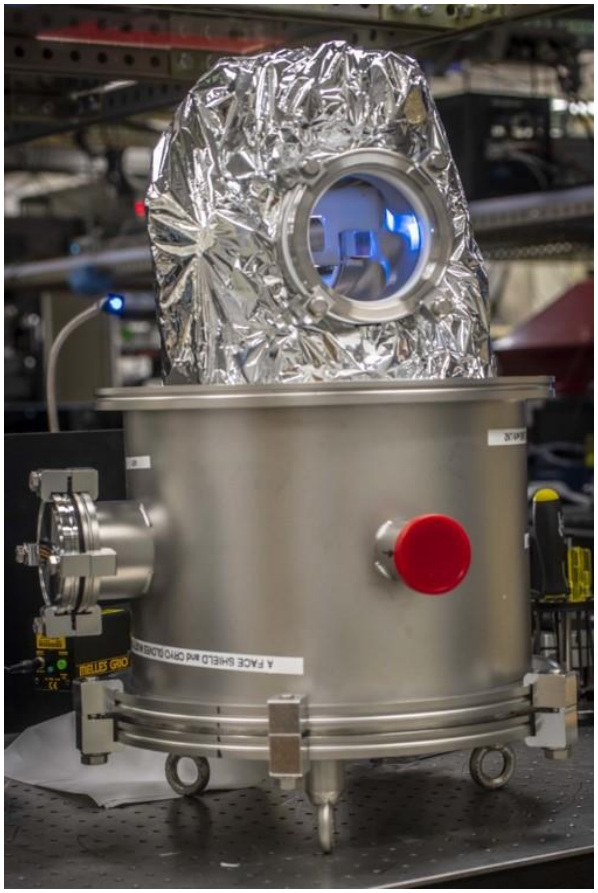

Figure 3: Unassembled two-chamber cryostat with prisms inside. The crystals are placed inside the internal chamber, which is insulated by mylar-aluminum foil. The cryostat is inverted in this figure because it was in the process of being assembled.

The two-chamber cryostat, shown in Figure 3, is made up of external and internal chambers. The internal chamber contains a crystal mount, which was 3-D printed to fit the KDP and ADP crystals. Temperature and pressure sensors were placed on the mount to record the temperatures of the crystals and ensure that the pressure inside the chamber is stable. The mount with ADP and KDP prisms and temperature and pressure sensors is shown in Figure 4.

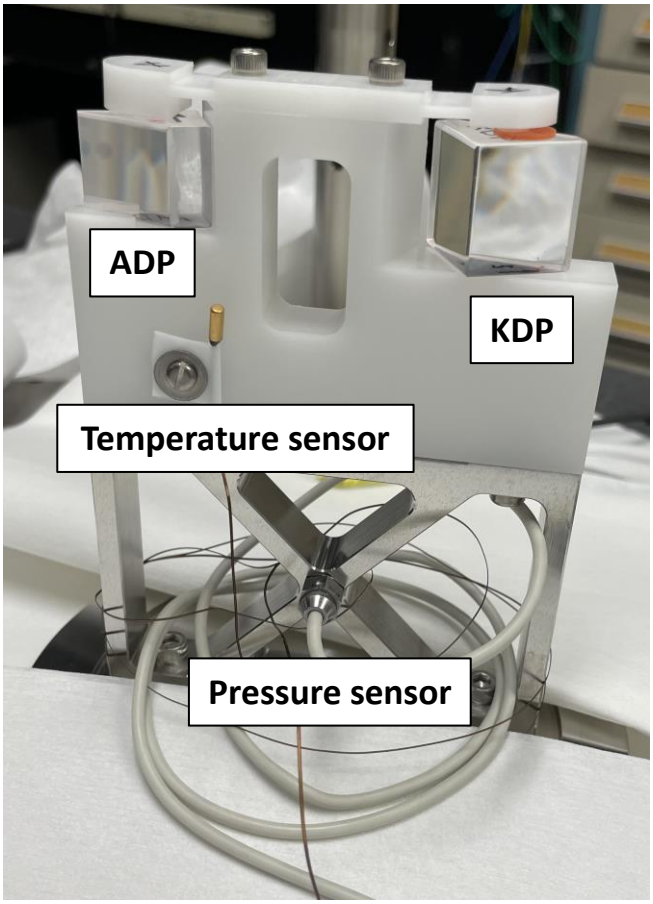

Figure 4: ADP and KDP crystals inside the 3D-printed mount. There are temperature and pressure sensors on the mount to track the temperature and ensure that the pressure inside the internal chamber is stable.

The internal chamber is filled with 1 atm of helium, which was chosen due to its high thermal conductivity. A liquid nitrogen tank is located inside the external chamber and connected to the internal chamber. “Cold flow” goes from the liquid nitrogen tank into the internal chamber. Since the contact area between the prisms and mount is minimized, the prisms are cooled down through surrounding He. This provides smooth (better than 0.1° C) temperature distribution across the prisms. Layers of multilayer insulation made of mylar-aluminum foil were wrapped around the internal chamber. A vacuum pump creates a vacuum in the external chamber, further ensuring that the internal chamber remains isolated from the outside environment. Both the internal and external chambers have two fused-silica windows on opposite sides of the chambers, which have sol-gel antireflection coatings.

3.3 Automated Liquid Nitrogen System

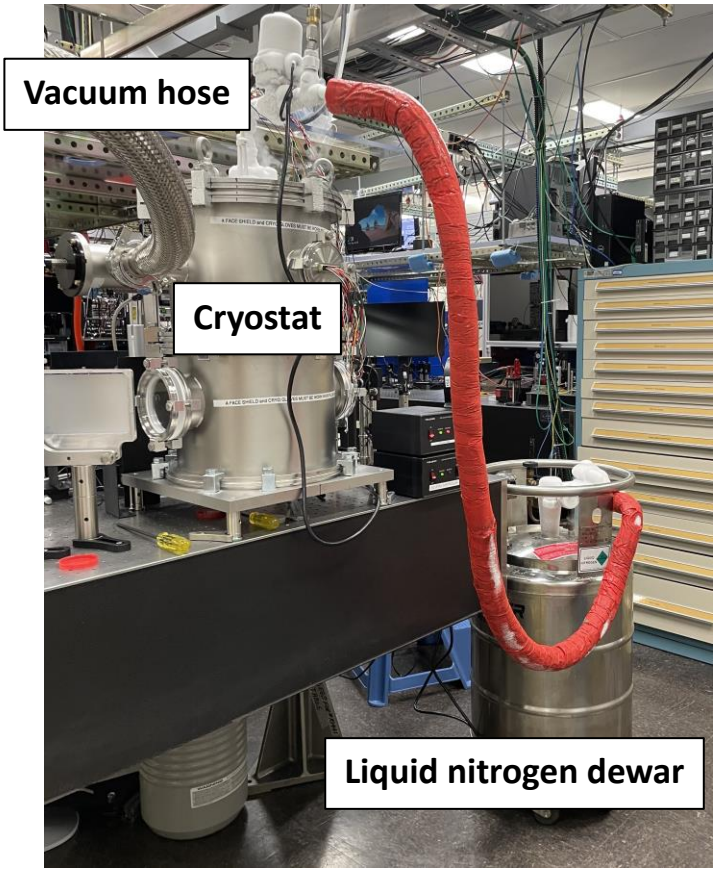

Figure 5: Automated liquid nitrogen filling system. This system was specially designed and fabricated for continuous cooling of the two-chamber cryostat. Liquid nitrogen is pumped from the dewar into the cryostat through a hose, cooling the crystals down from 300 K to 200 K.

An automated liquid nitrogen filling system, shown in Figure 5, was assembled to maintain low temperatures over the full aperture of the KDP and ADP crystals. Vaporized nitrogen creates pressure in the dewar, pushing liquid nitrogen through a hose into the cryostat. A solenoid valve regulates the flow of liquid nitrogen into the cryostat. The system is self-regulating and stops filling when the liquid nitrogen level reaches a set point in the cryostat. A safety valve prevents the pressure inside the dewar from exceeding 35 psi, and an oxygen deficiency detector monitors the oxygen level in the laboratory.

The system was tested to determine how long a dewar of liquid nitrogen will continue pumping before running out. The temperature decreases for about 12 hours when the liquid

nitrogen is filling the cryostat, and then the temperature slowly increases when the liquid nitrogen runs out. A full cycle (room temperature – 200 K – room temperature) lasts around 50 hours.

4 Experiment

Measurements for ADP were done first, and then the cryostat was rotated 180° to make measurements for KDP. The laser beams were precisely directed to hit the ADP crystal at an incidence angle of 8° and the KDP crystal at 12°. Diaphragms, which are opaque structures with an opening in the center, were utilized in the setup in order to keep the beams aligned to the crystals.

As the crystals cooled down from room temperature, around 295 K, to 200 K, the distance the refracted ray moved on a screen was measured for both the ordinary and extraordinary rays of red and green light at different temperatures. From this measurement and Equation (3), the refractive index can be determined at varying temperatures. The screen was located around 8 meters from the prism, making measurements more accurate since the beams are farther apart. The experimental setup was modeled using Graphite software, as shown in Figure 6.

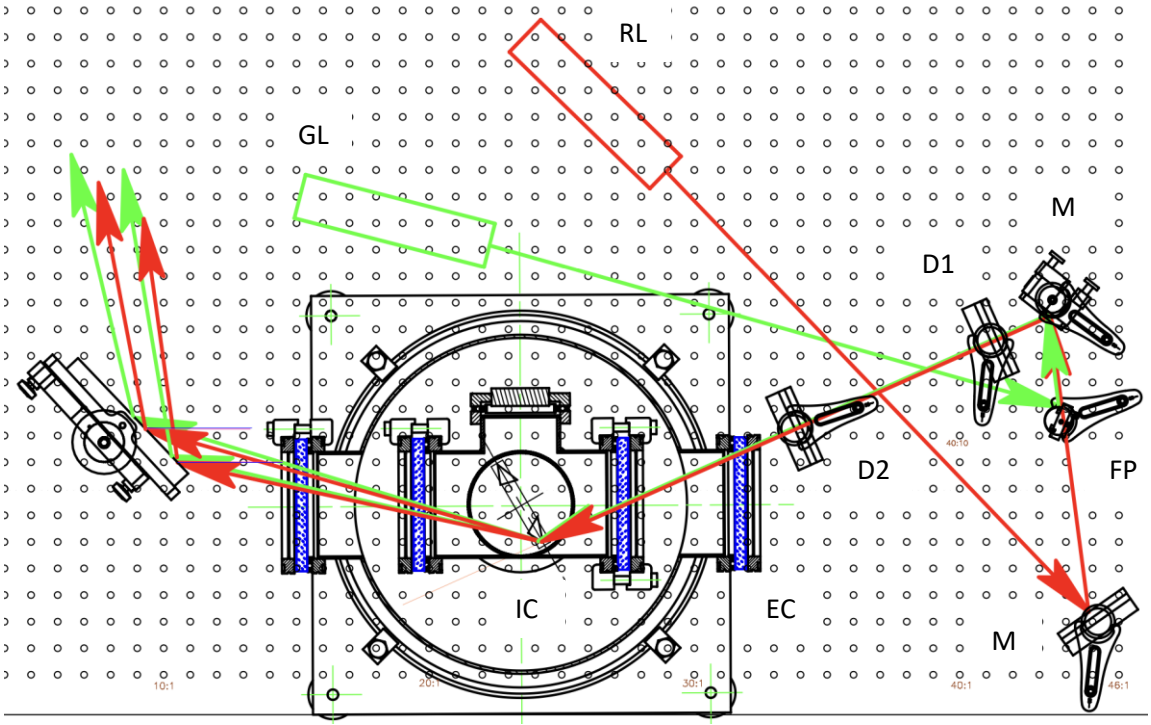

Figure 6: Experimental setup modeled on Graphite software. D1, D2 – input beam alignment diaphragms, M – mirrors, FP – flipping mirror, GL – green laser, RL – red laser, IC – internal chamber, EC – external vacuum chamber

A combination of lenses makes a laser beam collimated. Mirrors align both the red and green beams through the two-chamber cryostat on the same path. A beam enters through a window on the cryostat, passes through the prisms, and exits as two beams through the window on the other side of the cryostat. The two refracted beams then reflect off a mirror and hit a wall where their movements can be tracked. Using this, dimensions of the setup can be measured, and the angle of deviation can be determined.

5 Results

The refractive indices for KDP and ADP were graphed with temperature on the x-axis and refractive index on the y-axis, shown in Figure 7.

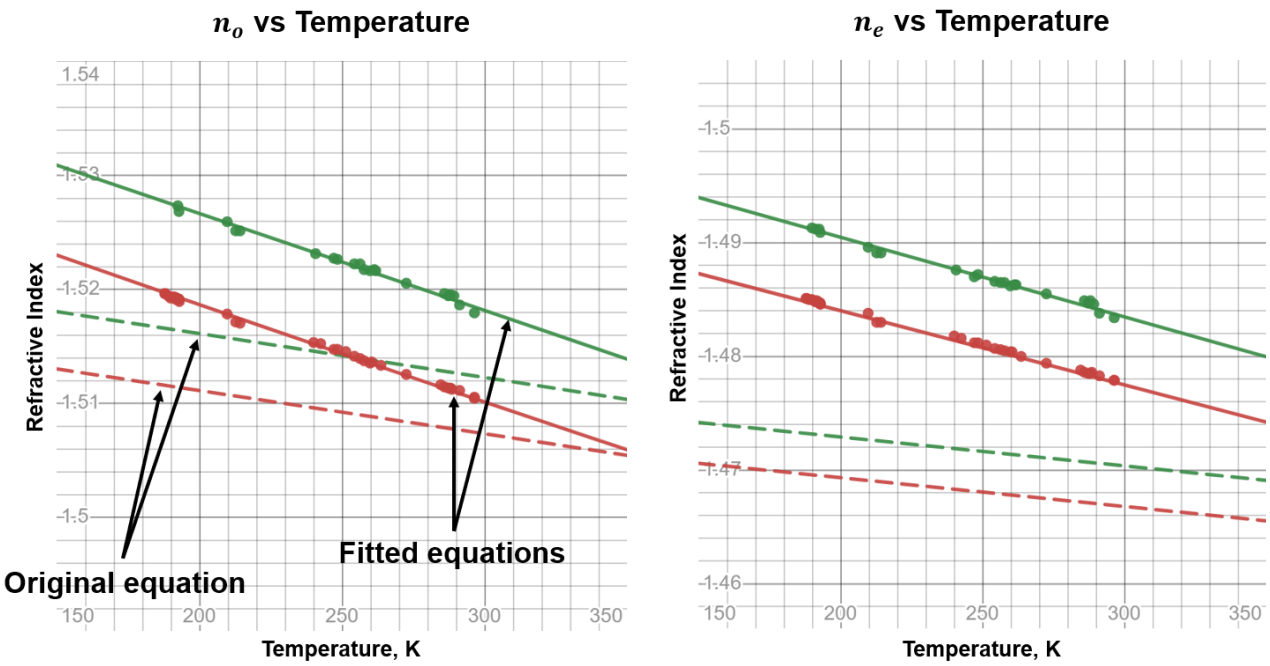

Figure 7: Original and fitted temperature-dependent Sellmeier equations for ordinary and extraordinary beams of KDP. n_o is the ordinary refractive index and n_e is the extraordinary refractive index. The green lines represent the measurements with the green laser and the red lines represent the measurements with the red laser.

The original KDP temperature-dependent Sellmeier equations were modified to fit the new data, with the updated equations shown below.

$$n_o^2 = (1.51 + 3.185 * 10^{-7}T) + \frac{(0.84181 - 1.4114 * 10^{-4}T) * \lambda^2}{\lambda^2 - (0.0139 - 1.83 * 10^{-5}T)} + \frac{(1 + 7.75 * 10^{-3}T) * \lambda^2}{\lambda^2 - 30} \quad (4)$$

$$n_e^2 = (1.495 - 8.2 * 10^{-5}T) + \frac{(0.727 - 1 * 10^{-4}T) * \lambda^2}{\lambda^2 - (0.01513 + 3.104 * 10^{-7}T)} + \frac{(1 - 9.8 * 10^{-4}T) * \lambda^2}{\lambda^2 - 30}$$

Keeping the original form of the equations, the numbers were incrementally adjusted to align the equations with the data points. The modified equations are steeper than the original equations, and there is a clear difference between the original and new graphs.

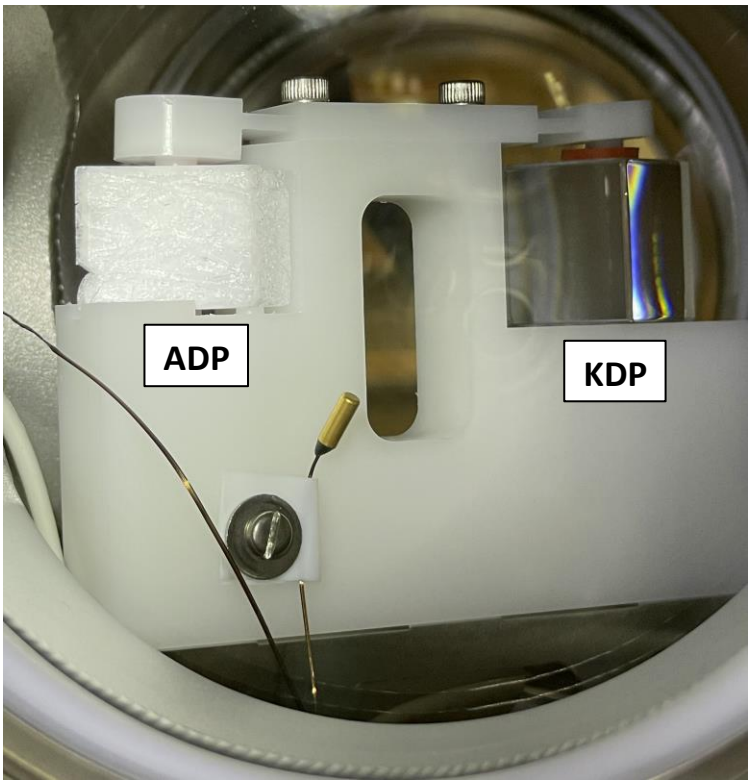

Figure 8: ADP prism cracked and crumbled during cooling stage, blocking any laser light from getting through, while the KDP prism survived.

Unfortunately, the ADP crystal crumbled at around 240 K, as shown in Figure 8. As a result, the data for ADP only ranged from 300 K to 240 K, instead of down to 200 K. One possible reason for this could be an excess amount of moisture inside the crystal, caused by repeated exposure to the air. The moisture in the crystal may have expanded due to the low temperatures, cracking the crystal. Since the ADP crystal cracked and the temperature range is limited, further measurements are needed to get accurate results through a wider range of temperatures.

6 Conclusion

Accurate measurements of the refractive indices of KDP and ADP at varying temperatures are essential to calculate phase matching of a wide range of nonlinear processes. There is a need

to modify the temperature-dependent Sellmeier Equations, which have proved unreliable for many decades.

The refractive indices of KDP and ADP were measured using the deviation of the ordinary and extraordinary beams when passing through triangular prisms at room temperature and at low temperatures. Using a two-chamber cryostat, the temperature could be lowered to 200 K.

A significant discrepancy between the measured refractive indices of KDP and ADP and the refractive indices calculated from the original Sellmeier equations has been demonstrated. The experimentally measured refractive indices at room temperature for KDP and ADP using a room-temperature testbed are in good agreement with the refractive indices calculated from the original Sellmeier equations. However, the same measurements done at room temperature for ADP and KDP inside the cryostat don't line up with the theoretical values from the original Sellmeier equations, showing a systematic error. As a result, additional series of measurements are needed.

7 Acknowledgements

I would like to thank Dr. Ildar Begishev for guiding me through the project. This could not have been done without his dedication and patience. I would also like to thank Alexander Maltsev for cutting and polishing the ADP and KDP prisms, Sean Carey for helping with the sensors and electronics, Mark Romanofsky for designing the prism holder, and Roger Janezic and Salvatore Scarantino for creating the automatic liquid nitrogen filling system. Lastly, I would like to thank Dr. Stephen Craxton for giving me the opportunity to work and do research in this laboratory.

8 References

1. T.R. Boehly, et al., “Initial performance results of the OMEGA laser system,” Opt. Commun. 133, p. 495-506 (1997).

2. J. H. Kelly, et al., “ OMEGA EP: High-Energy Petawatt Capability for the OMEGA Laser Facility,” J. Phys. IV France, **133**, p. 75-80 (2006).

3. J. S. Ross, S. H. Glenzer, J. P. Palastro, B. B. Pollock, D. Price, G. R. Tynan, and D. H. Froula, “Thomson-scattering measurements in the collective and noncollective regimes in laser produced plasmas,” Rev. Sci. Instrum. **81**(10), 10D523 (2010).

4. D. Basting and G. Marowsky, eds., Excimer Laser Technology (Springer, 2005).

5. I.A. Begishev, G. Brent, S. Carey, R. Chapman, I. A Kulagin, M. Romanofsky, M. J. Shoup III, J. D. Zuegel, and J. Bromage, “High-efficiency, fifth-harmonic generation of a joule-level neodymium laser in a large-aperture ammonium dihydrogen phosphate crystal,” Opt. Express, **29**, No. 2, p. 1879-1889 (2021).

6. V.G. Dmitriev, G.G. Gurzaydyan, D.N Nikogosyan, “Handbook of nonlinear optical crystals,” Springer Series in Optical Sciences, vol. 64, Third Edition (1999).

Chiroptical Properties and Mesophase Stability of Saturated Chiral Dopants for High Peak Power Liquid Crystal Device Applications

Jenny Zhao

Pittsford Mendon High School

Pittsford, NY

Advisors: Kenneth L. Marshall and Dr. Nathaniel D. Urban

Laboratory for Laser Energetics

University of Rochester

Rochester, NY

Summer High School Research Program 2022

April 2023

Abstract

Liquid crystal polarizer (LCP) devices are critical optics on the OMEGA laser used to transmit circularly polarized light while also functioning to protect the system from retro reflections. The chiral dopant used in the nematic LC host mixture in the majority of OMEGA LCP's is CB-15, a compound containing delocalized π-bonded structural elements that negatively impact the laser-induced damage threshold (LIDT) of the host LC, depending on the dopant concentration. The optical absorption of the material also increases as the incident wavelength approaches the ultraviolet (UV) region of the spectrum. These two factors serve to reduce the operational lifetime of LC optics employing CB-15 and prevent them from being deployed in the UV portion of the laser system for applications such as polarization control. The LIDT's of liquid crystals (LC's) are consistently higher in *saturated* materials (molecules in which π-bonds are either completely absent or widely isolated) than in their unsaturated counterparts, such as CB-15. In this work, several different saturated chiral dopants were evaluated over a wide range of concentrations in two different nematic LC hosts with the goal of finding a replacement material for CB-15 that possesses a higher LIDT. The factors considered included helical twisting power (HTP), UV absorbance, solubility, and LC phase orientation. Evaluation of these series of properties using polarizing optical microscopy and UV-VIS-NIR spectrophotometry showed that cholesterol oleate (CO), S-811, and MLC-6247 are promising saturated chiral dopant candidates. Although CO has a low HTP when calculated in terms of weight concentration, CO shows the best results to date due to CO's low UV absorbance, good solubility, and ability to produce the desired planar LC orientation. Future research is needed to determine the laser damage resistance of these promising chiral dopants.

1. Introduction

In the OMEGA laser system at the Laboratory for Laser Energetics (LLE), liquid crystal (LC) devices are used to transmit circularly polarized laser light, while simultaneously preventing back-reflected light from causing damage to the laser system. Circular polarization is desired as it allows the laser amplifiers to operate at nearly 100% efficiency by mitigating birefringence effects [1].

Unpolarized light contains two different circularly polarized components: right-handed (RH) and left-handed (LH). LC circular polarizers (LCP's) isolate one handedness of light from the other by allowing one handedness to pass through the device, while the other handedness is reflected or scattered. This effect is called "selective reflection" [1]. An illustrative example of the selective reflection effect is shown in Fig. 1. For a right-handed LCP, the right-handed circular light passes through the LC device towards the target, while the left-handed light is reflected. When back-reflected left-handed circular light encounters the LC device, the light is reflected diffusely since it is unable to pass through the LC device.

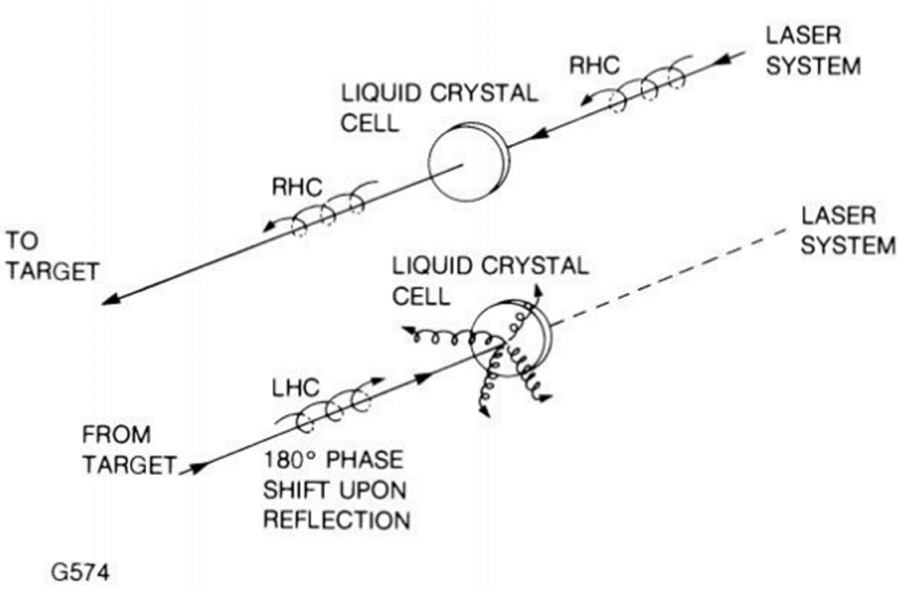

***Fig. 1*:** Illustration of the use of LCP's to protect the laser system from back-reflected light. RHC and LHC denote the two polarizations of light [2].

LCP devices consist of a mixture of a nematic LC host and a chiral dopant. Nematic LC's are rod-shaped molecules that exhibit anisotropy, meaning the physical properties of the material are directionally dependent [3]. In the nematic phase, there is long-range orientation of the LC molecules aligned in a particular direction, along a common axis, referred to as the director. However, they are not ordered in the same way as in a solid [3]. Instead, they maintain their fluidity and mobility, similar to a liquid. LCP's employ mixtures that orient in the chiral nematic LC phase. The chiral nematic LC phase is a phase that is characterized by the presence of chirality, or handedness, in the alignment of the LC molecules (Fig. 2). In this phase, the LC molecules are aligned in a particular direction, similar to the nematic phase, but they also exhibit a helically twisted structure in which the orientation of the molecules rotates along the axis perpendicular to the director (Fig. 2) [3]. This twisting structure is referred to as the cholesteric helix and possesses a pitch length, which is the distance for one full revolution of the director, the average alignment direction of the LC molecules [3]. The operational selective reflection wavelength of an LCP is governed by the pitch length and the average refractive index of the mixture.

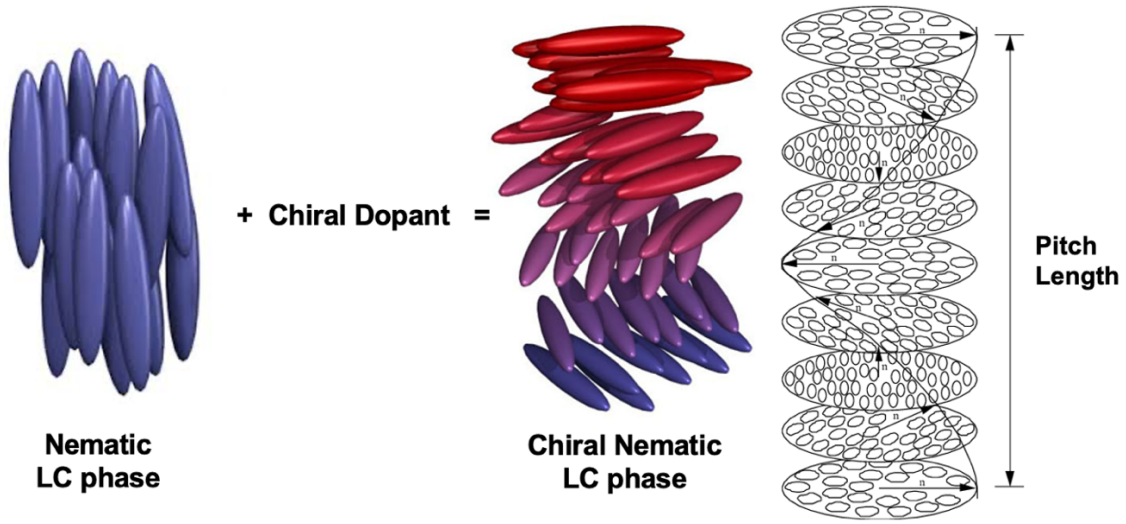

***Fig. 2*:** Visual representation of the components in a chiral nematic LC mixture, which includes a nematic LC and a chiral dopant. The chiral nematic LC mixture has a pitch length that comprises one full rotation of the director axis.

This "selective reflection" effect occurs for specific wavelengths that satisfy the equation $\lambda_{max}=\boldsymbol{n}p$, where λ_{max} is the selective reflection peak wavelength, $\boldsymbol{n}$ is the average refractive index of the mixture, and p is the pitch length. The pitch length is dependent on the chiral dopant concentration, its helical twisting power (HTP) (Fig. 3), and the mixture temperature [1].

$$\frac{1}{P} = B_M * c$$

$P = pitch\ length$

$B_M = HTP$

$c = wt\%\ concentration$

***Fig. 3*:** Equation used for the calculation of helical twisting power (HTP) of a chiral dopant. Because the value of HTP depends on the host LC composition, it must be determined separately for each host.

Molecular structures referred to as "saturated" contain almost no double bonds or π-bonded systems. In contrast, unsaturated structures contain delocalized π-bonds, typically in the form of benzene rings (Fig. 4).

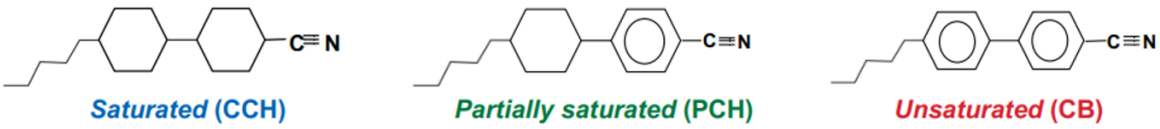

***Fig. 4*:** Illustration of saturated, partially saturated, and unsaturated molecular structures [4].

According to previous research conducted at LLE, laser-induced damage thresholds of LC's are much higher in saturated materials than in unsaturated materials (Fig. 5), which makes saturated structures more favorable for use in a high-peak-power laser system [5].

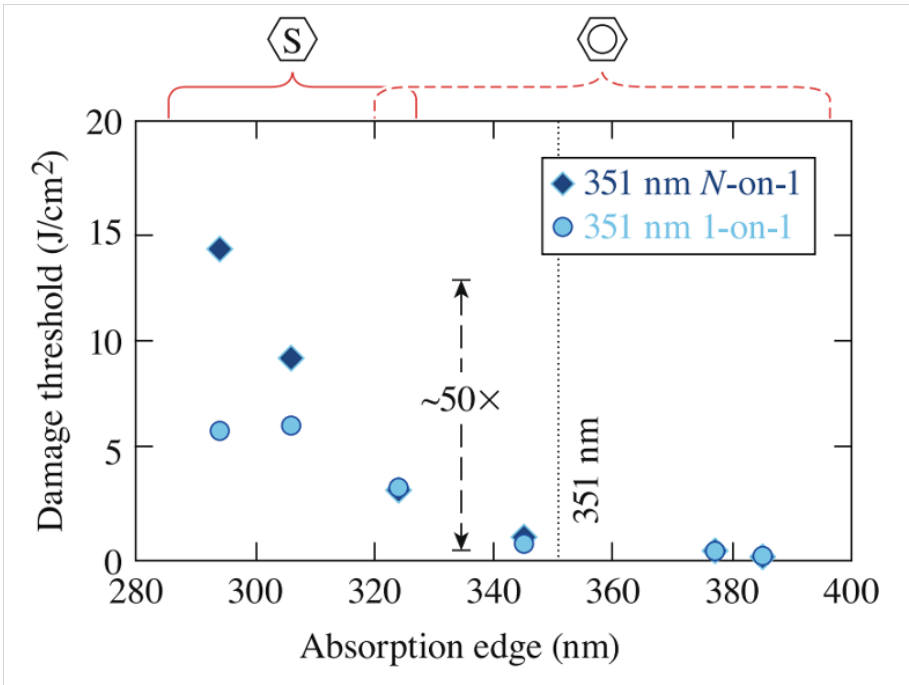

***Fig. 5*:** Graph of damage threshold (J/cm^2) vs absorption edge (nm) of saturated (left part of graph) and unsaturated (right part of graph) LC compounds [5].

The current chiral dopant, CB-15, used in the LCP devices in the OMEGA laser system has a highly unsaturated structure. It has many double bonds, in the form of two conjugated benzene rings and a triple bond between carbon and nitrogen in the cyano group.

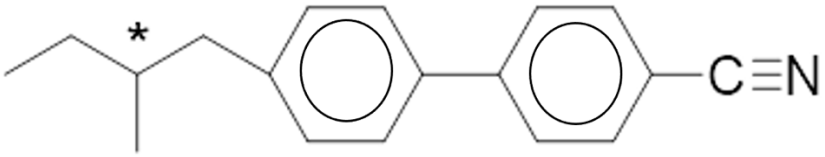

***Fig. 6*:** The molecular structure of CB-15, the current chiral dopant used in the OMEGA LCP devices.

For this study, the goal was to find a more laser-damage-resistant, saturated chiral dopant to replace CB-15. Ten commercially available saturated chiral compounds were evaluated as dopants in the nematic host LC's ZLI-1167 and MLC-2037 (Table 1). ZLI-1167 showed better compatibility and stability with the dopants, so this study is focused mainly on this host.

Saturated Chiral Compounds	Nematic Host LC's
Cholesterol oleate (CO)	ZLI-1167
S-(-)-Perillyl alcohol	MLC-2037
L-Proline t-butyl ester	
Uridine	
2-Ethyl fenchol	
S-(-)-Limonene	
S-811	
MLC-6247	
Stigmasterol	
Androsterone C9 ester	

***Table 1*:** Table displaying a list of 10 different saturated chiral compounds and 2 nematic host LC's studied in this work.

The saturated chiral dopants tested contain little-to-no double bonds in the structures, and they possess either mesogenic or isotropic phases in their pure state (three examples are shown in Fig. 7). Mesogenic materials are those that exhibit mesophase behavior, meaning they exhibit both liquid-like and solid-like properties, and display orientation-dependent optical properties. Isotropic materials have no preferred orientation, and their physical properties are the same regardless of the measurement direction (e.g., water) [3]. The distinction between mesogenic and isotropic is a fundamental aspect of the behavior of LC materials and has important implications for the design and functionality of LC materials and devices.

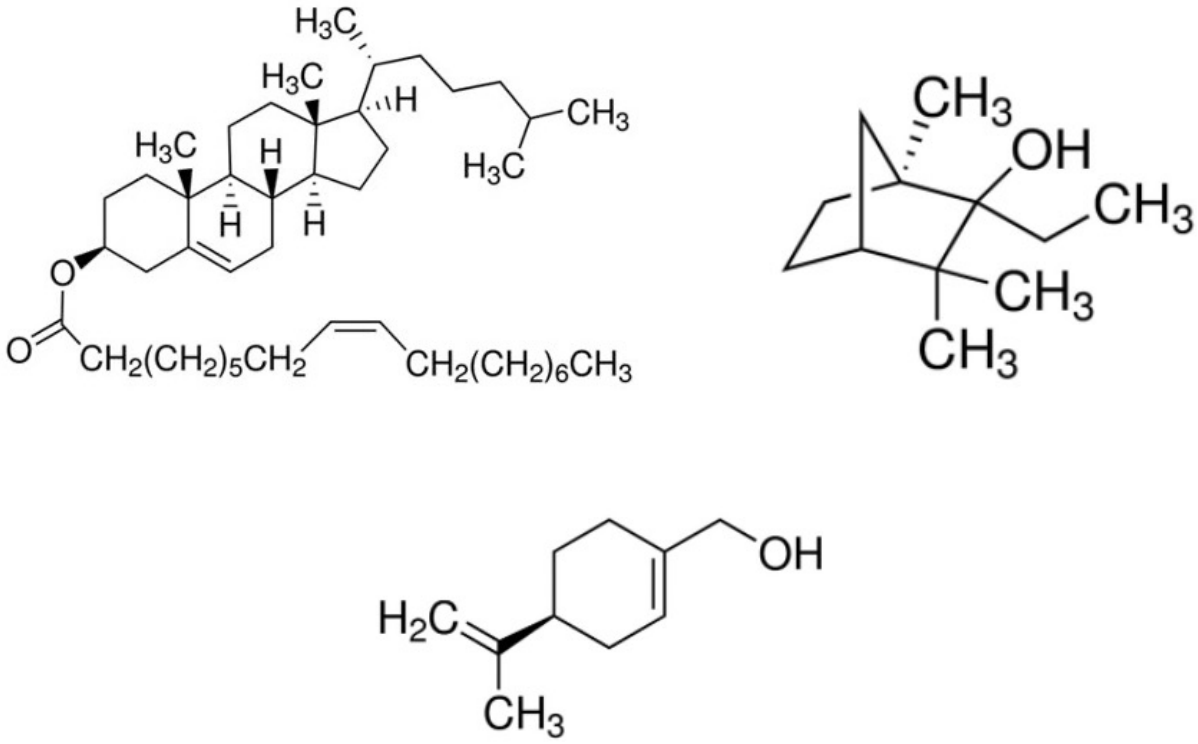

***Fig. 7*:** The molecular structures of some of the chiral dopants studied in this work: CO (mesogenic) (top-left), 2-ethyl fenchol (isotropic) (top-right), and S-(-)-perillyl alcohol (isotropic) (bottom).

2. Experimental Procedures

2.1 UV Transmittance of chiral dopants

Evaluating the UV absorbance of the chiral dopant candidates was the preliminary screening method. To do so, the dopants were dissolved in cyclohexane at 0.235 molal concentration (molal = moles of solute per kilogram of solvent). The transmittance of the chiral dopants in cyclohexane was measured using UV-VIS-NIR spectrophotometry on a Lambda 900 (Perkin Elmer) spectrophotometer using quartz cuvettes (Starna) with 1 cm path lengths. Cyclohexane is a UV-transparent solvent that does not interfere with this analysis. This method was used since some of the chiral dopants are in the solid phase at room temperature, and they

must be in a liquid form for the UV-VIS-NIR analysis. High UV transparency is typical of saturated structures and an indicator that the compounds may possess high laser damage thresholds.

2.2 Preparation of LC Mixtures

LC mixtures were prepared by combining a saturated chiral dopant and a nematic host in a glass vial that had been cleaned with isopropyl alcohol and spectral grade methanol. Depending on the phase the chiral dopants and nematic hosts are in at room temperature, a metal spatula or a syringe was used accordingly to help measure and transfer the materials from their original containers to the cleaned glass vial. The quantities of dopants and nematic hosts were measured in milligrams using a top-loading balance, which measured to the hundredths place. The mixtures were then heated on a hot plate for 30 minutes with stirring until the mixture became homogenous. The mixtures were typically heated to 100°C unless a chiral dopant was evaluated with a boiling point below this value. In that case the mixture was heated to 50°C.

2.3 LC Phase Analysis: Polarizing Optical Microscopy

Test samples for polarizing optical microscopy were prepared by placing a small amount of the LC mixture between a microscope slide and coverslip. The slides were then placed under the polarizing optical microscope (POM) in a hot stage. The different phases of the samples were observed under the microscope at 100X magnification. Two heating cycles were run on the sample: 7°C/min followed by 2°C/min. The 7°C/min heating cycle was used to even out the mixture and make it more homogenous. The 2°C/min heating cycle was used to determine the phase behavior of the mixture. The temperatures at which the sample went through a phase transition and the orientation of the sample (planar, fingerprint, focal conic, or homeotropic, diagrammed in Fig. 8) were recorded. The heat cycle would be stopped once the mixture became completely isotropic,

which is when the LC material becomes completely transparent, and the LC molecules are randomly oriented with no long-range orientation or ordered structure. The temperatures at which the LC mixture changed phases and the orientation of the mixture were recorded again as the LC mixture cooled from its clearing point back down to room temperature. If the LC mixture had a fingerprint orientation (cholesteric helix axes parallel to the substrates), its pitch length in micrometers was determined using the POM (without the hot stage) to focus on the fingerprint pattern using a 50X objective (500X total magnification). The distance between two successive light-dark sequences in the texture in micrometers was measured in several areas of the sample, and the distances were averaged to determine the pitch length.

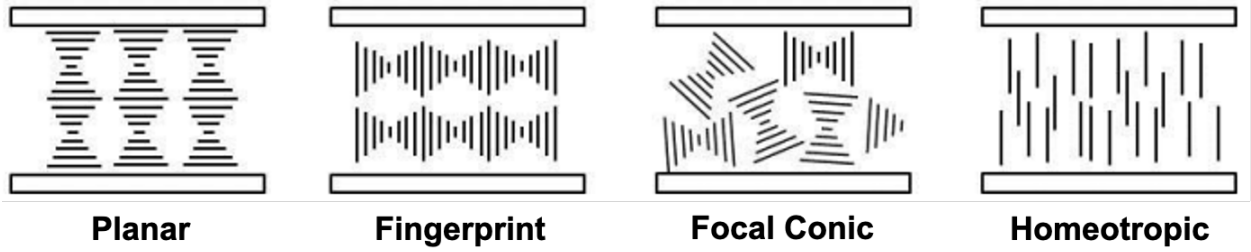

***Fig. 8*:** Illustrations of the different types of possible chiral nematic LC orientations between two substrates.

2.4 LC Mixture Pitch Length and HTP Analysis: UV-VIS-NIR Spectrophotometry

The UV-VIS-NIR spectrophotometer (UV-VIS-NIR) was used to determine the test mixtures' selective reflection peak wavelengths (λ_{max}). This instrument determines the transmittance of the mixture by scanning different wavelengths of light through the mixture. Initial scans of new mixtures were conducted over a wide range of wavelengths from 3000 nm to 300 nm. The selective reflection peak wavelength was determined by a 50% loss in transmission of the sample. The 50% loss in transmission is due to half of the light from the UV-VIS-NIR being reflected or scattered by the chiral nematic fluid. The minima of the percent transmission are used to determine pitch lengths, which are then used to calculate the HTP's. Pitch length vs.

concentration dilution curves were created to calculate the weight percent of chiral dopant that was needed in the nematic host to hit the 1054 nm pitch length.

2.5 LC Mixture Device Fabrication

The LC test devices were constructed in a Class 10000 clean room environment. They were created by buffing nylon alignment layers on glass substrates and depositing spacers consisting of 22-micron microspheres mixed in epoxy between the substrates applied in four places near the edges. The empty devices were placed on a hot plate and heated to 70°C, then filled with the LC mixture using a syringe and allowing the LC fluid to flow into the cell gap. In the device, the orientation of the mixture is determined using the POM and the λ_{max} is determined using the UV-VIS-NIR.

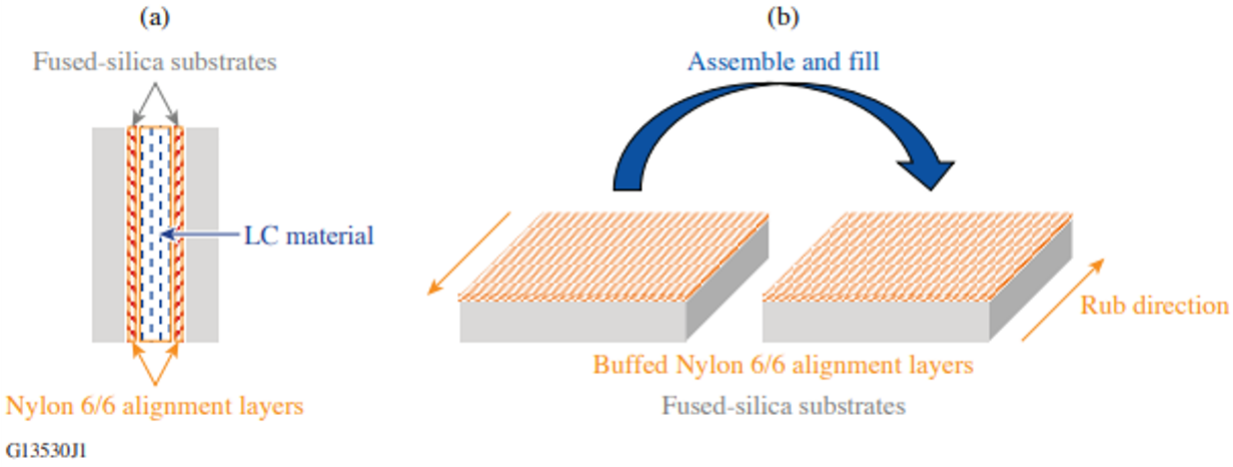

***Fig. 9*:** Illustration showing a side view of the process of fabricating an LC device; (a) LC material is sandwiched between two fused silica substrates; (b) two fused silica substrates are coated with nylon and buffed to create alignment layers, assembled and filled.

3. Results and Discussion

The POM analysis conducted on the chiral nematic mixtures revealed that many of the chiral dopants demonstrated good phase behavior with the LC hosts. Figure 10 shows

photomicrographs of the fingerprint (left) and focal conic (right) textures observed for two chiral nematic mixtures under polarized light. The focal conic orientation is more desirable as it indicates the mixture is likely to form a planar orientation in a device. A planar orientation is necessary for a circular polarizer to function. For mixtures that displayed the fingerprint texture, the pitch length was determined by measuring the distance across the length of two successive light-dark bands. The pitch length of focal conic mixtures was obtained from their selective reflection peak wavelength determined by UV-VIS-NIR spectrophotometry.

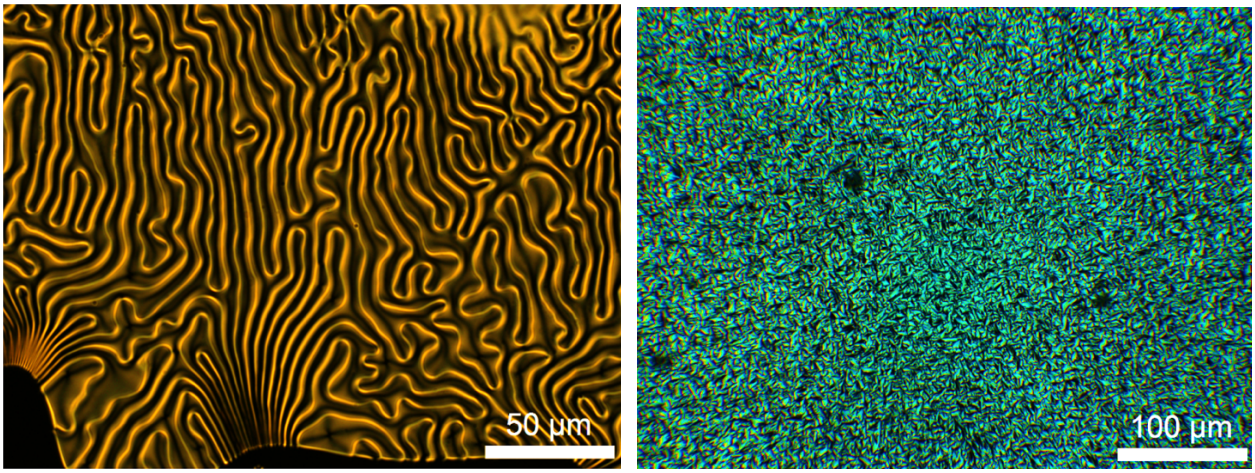

(a) (b)

***Fig. 10*:** Photographs taken using POM of (a) 15 wt% S-(-)-perillyl alcohol in ZLI-1167 "fingerprint texture" and (b) 39.17 wt% CO in ZLI-1167 "focal conic" texture; these photographs differ from the side-view diagrams in Fig. 8 in that they are captured from the direction of incident light propagation.

Pitch length and helical twisting power (HTP) are inversely related in the equation shown in Fig. 3. The HTP for a single dopant may also be different depending on which nematic host it is dissolved in. The chemistry of both the host and dopant are important to the HTP.

The UV absorbance values of the pure chiral dopants in cyclohexane were determined by UV-VIS-NIR spectrophotometry. With the exception of S-(-)-perillyl alcohol, all of the dopants tested demonstrated a lower UV absorbance than CB-15 (Fig. 11), which indicates that these

compounds may be more resistant to laser-induced damage. The CB-15 solution absorbs a significant amount of UV light and is completely absorbing by 325 nm.

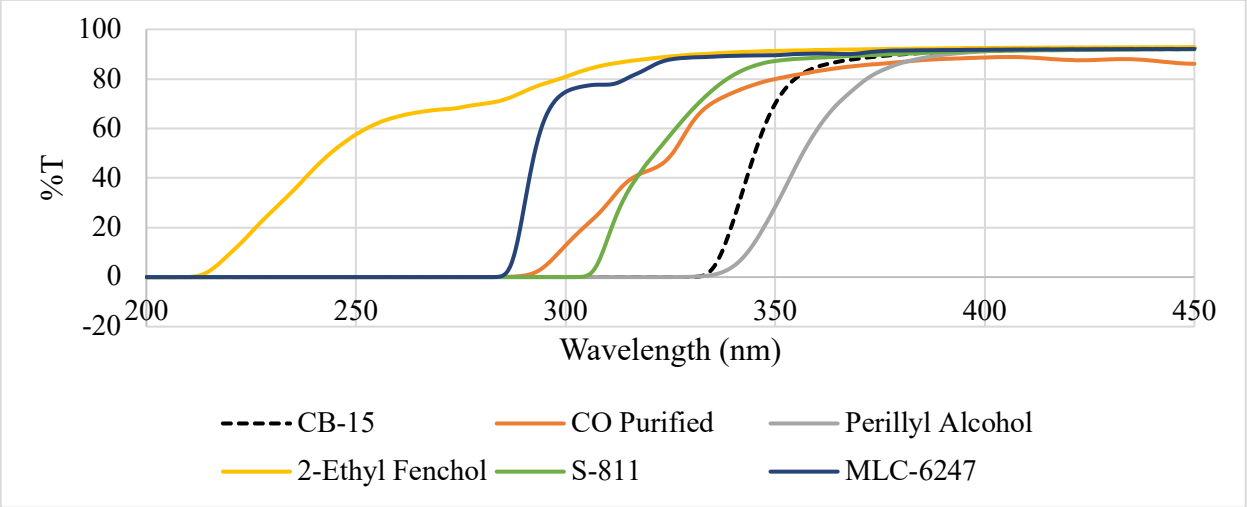

***Fig. 11*:** Graph of the UV-Vis absorption spectrum of pure chiral dopants dissolved in cyclohexane. The spectrum of CB-15 in cyclohexane is shown in the dashed line and exhibits a sharp UV absorption cutoff below 350 nm.

S-811 and MLC-6247 both had favorable UV transmission, but no further research was done pursuing these chiral dopants due to time constraints. A more detailed study of these promising chiral dopants will be performed in future studies. Due to a combination of promising properties such as good solubility, low UV absorbance, and promising LC orientation, the λ_{max} for the CO mixture in ZLI-1167 was fine-tuned to the operating wavelength of the OMEGA circular polarizers (1054 nm). This process involved preparing a series of concentrations ranging from 30% to 50% CO in 5% increments and measuring the selective reflection band on the UV-VIS-NIR. A plot of the λ_{max} vs wt% CO was constructed (Fig. 12) from this data. Based on this plot, 41.5% CO in ZLI-1167 was determined to be the concentration necessary for generating a λ_{max} at 1054 nm. Using the UV-VIS-NIR, the 41.5% CO in ZLI-1167 mixture was determined to have a λ_{max} of 1049 nm, which is within the specification tolerances for OMEGA (1054 +/- 13 nm).

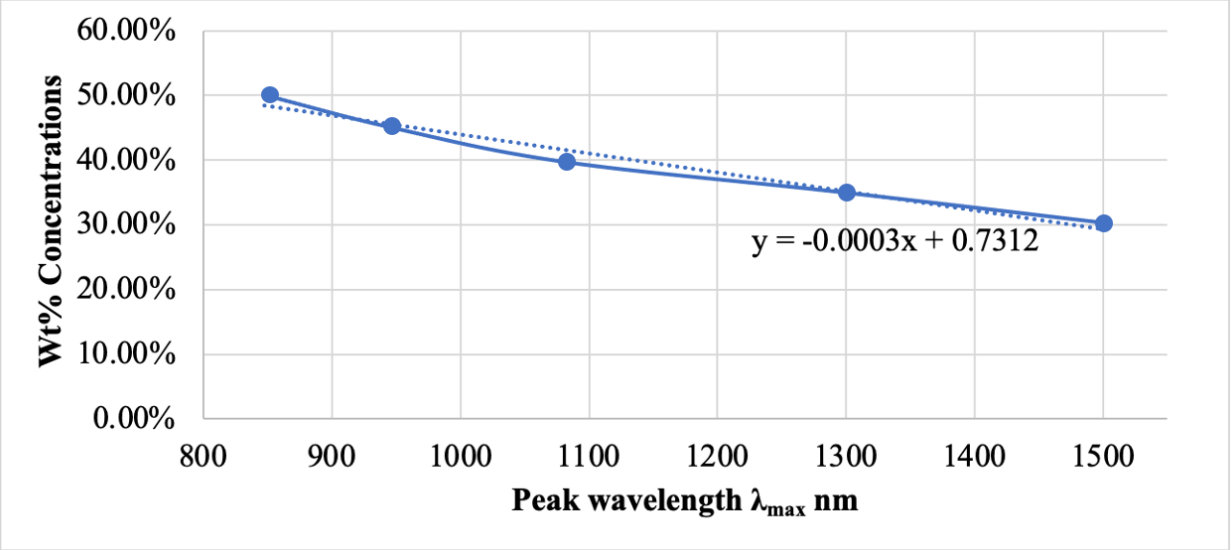

***Fig. 12*:** A dotted best-fit linear graph of the wt% concentration vs. λ_{max} was created using data from the % transmittance of 5 dilutions of CO in ZLI-1167 mixture at different wavelengths represented by the points on the solid line.

The mixtures 19.43 wt% CB-15 in ZLI-1167 and 41.13 wt% CO in ZLI-1167 both represent a wt% concentration of chiral dopant that generates λ_{max} near 1054 nm. The enantiomeric purity of both dopants is assumed to be 100%. The equation shown in Fig. 3 was used to determine the HTP of both mixtures. The 19.43 wt% CB-15 in ZLI-1167 mixture had an HTP of 4.83 μm^{-1}, and the 41.13 wt% CO in ZLI-1167 mixture had an HTP of 2.28 μm^{-1}. Although CO has a smaller HTP than CB-15, its improved UV transparency makes it promising.

Using the 41.13% CO in ZLI-1167 mixture as the reference, an LC device was then fabricated using 41.5% CO in ZLI-1167 following the procedures described in Section 2.2 and Fig. 9. The purpose of the device was to see if the focal conic chiral nematic mixture was able to align in the desired planar orientation when placed between two fused silica substrates with alignment layers. This phase alignment is critical for an LCP to function properly, so any new LC candidate mixture must demonstrate the ability to align in this orientation. Analysis by POM showed that the

CO-in-ZLI-1167 LC device displayed a planar orientation (Figure 13), demonstrating that CO is a viable candidate to replace CB-15.

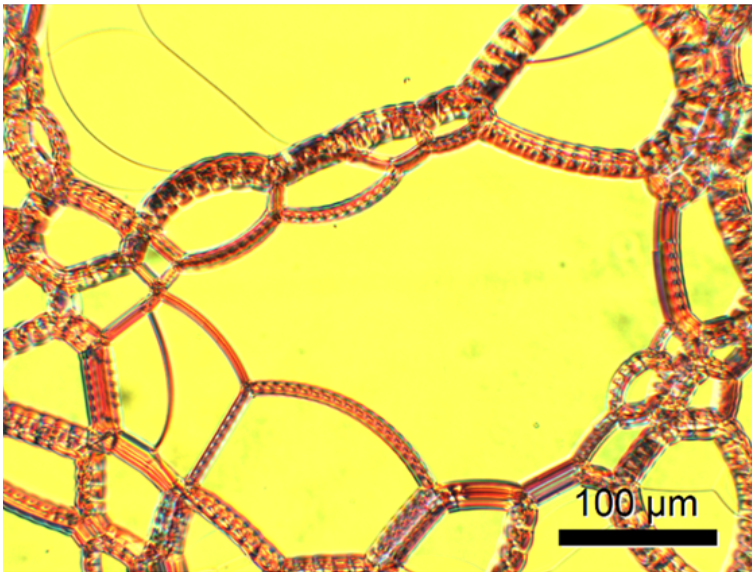

***Fig. 13*:** POM micrograph of a mixture of 41.5% CO in ZLI-1167 in an LC device. The homogenous yellow background with sporadic disclination lines (brown), often termed as the "oily streaks" texture, indicates that a planar orientation has been achieved.

Overall, CO was found to be the most promising chiral dopant since it has a balance of important properties such as high HTP, low UV absorbance, good solubility, and a planar chiral nematic orientation in the ZLI-1167 nematic host. While S-811 and MLC-6247 showed promising UV absorbance, further research needs to be done to evaluate these dopants. The other chiral dopants were not evaluated further due to them displaying a fingerprint texture or insolubility in the nematic host ZLI-1167. A summary of these properties and behavior including physical state, solubility, wt.% concentration, pitch length, texture, twist sense, and HTP in ZLI-1167 is shown in Table 2.

Dopant	Physical state (25°C)	Soluble in ZLI-1167	Dopant concentration Wt.%	Pitch length (µm)	Texture	Twist sense	HTP in ZLI-1167 (μm^{-1})
CB-15	Isotropic liquid	Y	19.43%	1.066	Planar	RH	4.83
Cholesteryl oleate	Solid	Y	41.13%	1.067	"Oily streaks"	LH	2.28
S-811 (R-811)	Solid	Y	13.35%	1.064	Planar	LH (RH)	7.04
MLC-6247	Solid	Y	14.06%	1.055	Planar	LH	6.74
S-(-)-Perillyl alcohol	Isotropic liquid	Y	15%	2.15	Fingerprint	LH (RH)	3.10
2-Ethyl fenchol	Isotropic liquid	Y	15%	5.02	Fingerprint	LH (RH)	1.33
S-(-)-Limonene	Isotropic liquid	Y	10%	2.62	Fingerprint	LH (RH)	3.54
L-Proline, t-butyl ester	Isotropic liquid	Y	15%	11.07	Fingerprint	LH (RH)	0.602
Uridine	Solid	N	--	--	--	LH	--
Stigmasterol	Solid	N	--	--	--	LH	--
Androsterone C9 ester	Solid	N	--	--	--	--	--

***Table 2*:** Table displaying a list of 11 different saturated chiral compounds and their properties studied in ZLI-1167.

4. Conclusions

Ten different saturated chiral dopants were tested in two different nematic hosts (Table 1) as alternatives to CB-15. Using POM and UV-VIS-NIR, the solubility, UV absorbance, HTP, and orientation of the mixtures and pure dopants were determined. Most of the chiral dopants were not evaluated in further detail, due to either their fingerprint texture observed by the POM or their insolubility in the ZLI-1167 nematic host (Table 2). A few of the mixtures that showed good results were then filled into devices. The devices were tested for planar orientation using the POM, which

is essential for circular polarizers to work, and for the selective reflectance peak using the UV-VIS-NIR to determine that the λ_{max} was maintained. After testing a range of different saturated chiral dopants, CO was determined to be a very promising dopant candidate for LCP's. However, CO cannot be used as a direct replacement for CB-15, as it transmits left-handed circularly polarized light while CB-15 passes right-handed circularly polarized light. Some dopants under consideration are available in both left-handed and right-handed forms, such as S-811, which is left-handed and R-811, the right-handed form of S-811. As a result, they can be considered as replacements for CB-15 in right-handed LCP's. Future research will be focused on determining the laser damage threshold of chiral nematic mixtures employing CO and other promising dopants such as S-811 and MLC-6247.

5. Acknowledgments

I thank Dr. Stephen Craxton for providing this wonderful opportunity to conduct this research and meet other like-minded hardworking peers; Ms. Kimberly Truebger for organizing this program; my project advisors Mr. Kenneth Marshall and Dr. Nathaniel Urban for their endless help, support, and guidance throughout; Mr. Leonid Solodov and Ms. Ji-Mi Jang, the undergraduate mentors, who helped me gain familiarity and answer questions regarding my project; Mr. Eugene Kowaluk for his photography. Finally, I acknowledge the U.S. Department of Energy, the National Nuclear Security Administration, the National Science Foundation, New York State, and the University of Rochester for providing the funding for this research.

6. References

[1] J. Bonadonna, (2016, March), "Next Generation Liquid Crystal Mixtures for OMEGA Circular Polarizer/Isolator Devices", retrieved July 2022, from http://www.lle.rochester.edu/media/publications/high_school_reports/documents/hs_reports/2015/Bonadonna_James.pdf

[2] S. D. Jacobs, K. A. Cerqua, K. L. Marshall, A. Schmid, M. J. Guardalben, and K. J. Skerrett, "Liquid-Crystal Laser Optics: Design, Fabrication, and Performance," in *Journal of the Optical Society of America B*, Vol. 5, Issue 9, pp. 1962-1979, https://doi.org/10.1364/JOSAB.5.001962, 1988.

[3] P. J. Collings and J. S. Patel, *Handbook of Liquid Crystal Research,* Oxford University Press, 1997.

[4] K. L. Marshall, K. R. P. Kafka, N. D. Urban, J. U. Wallace, and S. G. Demos, "The Effect of Incident Polarization Handedness and Ellipticity on the Laser-Damage Resistance of Oriented Liquid Crystals in the Nanosecond Regime," Vol. 11910, *SPIE Laser Damage Conference*, 2021.

[5] T. Z. Kosc, A. A. Kozlov, S. Papernov, K. R. P. Kafka, K. L. Marshall, and S. G. Demos, "Investigation of Parameters Governing Damage Resistance of Nematic Liquid Crystals for High-Power or Peak-Intensity Laser Applications," *Scientific Reports* 9, 16435, 2019.